Comprehensive Approaches and Results in the Indirect Dark Matter Search

by

Alex Geringer-Sameth

A.B., Washington University; St. Louis, MO, 2007

A dissertation submitted in partial fulfillment of the
requirements for the degree of Doctor of Philosophy
in the Department of Physics at Brown University

PROVIDENCE, RHODE ISLAND

May 2013

This dissertation by Alex Geringer-Sameth is accepted in its present form
by the Department of Physics as satisfying the
dissertation requirement for the degree of Doctor of Philosophy.

Date_____ _____

Savvas M. Koushiappas, Ph.D., Advisor

Recommended to the Graduate Council

Date_____ _____

Ian Dell'Antonio, Ph.D., Reader

Date_____ _____

Richard Gaitskell, Ph.D., Reader

Approved by the Graduate Council

Date_____ _____

Peter Weber, Dean of the Graduate School

Vitae

Alex Geringer-Sameth was born on July 2nd, 1985 in New York, NY. He graduated from Croton-Harmon High School in 2003 and received his A.B. in Physics with Honors from Washington University in St. Louis in May 2007. That fall he joined the Physics Department at Brown University as a graduate student and in the summer of 2009 began working with Savvas Koushiappas. Alex completed his preliminary exam in April 2011.

Refereed publications

"Dark Matter line search using a joint analysis of dwarf galaxies with the Fermi Gamma-ray Space Telescope", Alex Geringer-Sameth & Savvas M. Koushiappas, *Physical Review D*, **86**(2), 021302(R) (2012).

"Detecting unresolved moving sources in a diffuse background", Alex Geringer-Sameth & Savvas M. Koushiappas, *Monthly Notices of the Royal Astronomical Society*, **425**, 862 (2012).

"Extracting the unresolved pulsar contribution to the gamma-ray background", Alex Geringer-Sameth & Savvas M. Koushiappas, *Monthly Notices of the Royal Astronomical Society*, **421**, 1813 (2012).

"Exclusion of canonical WIMPs by the joint analysis of Milky Way dwarfs with Fermi", Alex Geringer-Sameth & Savvas M. Koushiappas, *Physical Review Letters*, **107**(24), 241303 (2011).

Presentations

Invited Seminars:

Center for Cosmology and AstroParticle Physics at Ohio State University, Columbus OH, Nov 13, 2012

Kavli Institue for Cosmological Physics at the University of Chicago, Chicago IL, Oct 19, 2012

Yale Center for Astronomy and Astrophysics at Yale University, New Haven CT, Sep 21, 2012

Fermilab, Batavia IL, Sep 17, 2012

Michigan Center for Theoretical Physics at the University of Michigan, Ann Arbor MI, Sep 12, 2012

University of Pittsburgh, Pittsburgh PA, Dec 7, 2011

Conferences:

The Fourth Fermi Symposium, Monterey CA, Oct 30, 2012

Identification of Dark Matter 2012, Kavli Institue for Cosmological Physics at the University of Chicago, Chicago IL, July 26, 2012

Workshops:

SnowDOG - Dark Matter Observations with Gamma-rays, University of Utah, Salt Lake City UT, Mar 25, 2012

Posters:

SLAC Summer Institute, Menlo Park CA, July 26-28, 2011

Awards

2012-2013 Brown University Department of Physics Galkin Foundation Fellow

Schools attended

XXXIX SLAC Summer Institute: History of the Universe, Menlo Park CA, July 25-Aug 5, 2011

Teaching

Grader for PHYS 1250, Stellar Structure, Fall 2010, Spring 2012

Teaching assistant for PHYS 0400, Electricity & Magnetism, Spring 2008, 2009

Teaching assistant for PHYS 0300, Mechanics, Fall 2007, 2008

Acknowledgements

This thesis represents much more than my past four years of research at Brown. I have been shaped and supported by many people throughout my life and have benefited immensely from the friendship and wisdom of my family, friends, and colleagues over the years. The boundaries between these three categories are extremely blurry.

First I want to express my sincere gratitude to my advisor, Savvas Koushiappas. Perhaps the relationship between a beginning faculty member and their first student is a privileged one. From my vantage point, however, I think our relationship reflects Savvas's very special personality and ability as a mentor, scientist, and friend. Over the past four years he has shared an incredible amount of wisdom about our field and about the interplay between politics, personalities, and science. I feel so pleased and honored that he gave me the room to explore, allowing my curiosity to guide our research, while always staying in very close contact and keeping his eye on our goals. He buoyed my spirits countless times and it has been a great pleasure to work together as collaborators.

The Brown physics faculty has been nothing but supportive for the past six years. I was very fortunate to have my office not ten feet from from Ian Dell'Antonio's, whose depth of knowledge is matched only by his kind, caring, and gentle personality. Never once did he turn me away as I popped in constantly, pestering him with many many many questions about astrophysics. I would like to express my thanks to Rick

Gaitskell for serving on my committee along with Ian and Savvas, and especially for his extremely insightful comments every time I shared my progress with him. Dave Cutts and Bob Lanou have been supportive and I'm very honored that they have taken an interest in this work. I have learned a seemingly infinite amount from my collaborators at other institutions. Ben Zitzer, Karen Byrum, Bob Wagner, and Matt Walker have been phenomenal and I look forward to great experiences with them in the future.

I would still be struggling with my first project if not for the generous support and friendship of Jackie Chen, who worked a few desks away from me for about two years just as I was beginning in astrophysics. Though it must have been frustrating to be constantly distracted with endless questions she always took the time to help me. I have tried, not nearly as successfully, to carry on this tradition with the new students who ask me questions. To that end, it has been a pleasure to get to know Urmila Chadayammuri, Alejo Stark, and Deivid Ribeiro. I am so impressed by their progress and I have great confidence in all of them.

Surviving (even thriving) over the past six years would simply be impossible without a wonderful group of friends. I must thank Alex Metaj, Andy Blaeser, and Dave Malling for their close companionship, intense late-night debating, sharing of their thoughts and concerns, and for being just awesome and kind people. Thank you to my dear Florian Sabou, who shared so many new ideas with me over many meetings where we looked up and somehow eight hours had passed. I feel so lucky to be friends with Mirna Mihovilovic, Antun Skanata, Son Le, and Alexandra Junkes and I hope I was able to provide them a deeper and more complex window into life halfway around the world. I have great memories of the ski trips (except for the last one). A special thank you to Kyle Helson for interrupting my days at all the right moments. I will always be grateful for having been surrounded by excellent

classmates and friends: Juliette Alimena, Erica Barth, Saptaparna Bhattacharya, Jeremy Chapman, Dave Cohn, Andrew Favaloro, Dan Griffin, Carlos Hernandez-Faham, Il-Yong Jung, Ata Karakci, Nate Korey, Mike Luk, Jacqueline McCleary, Elizabeth Mermel, Dhriti Nandan, Tim Raben, Mike Segala, James Verbus, Chenjie Wang, and Qibin (Ace) Ye. If I didn't have to turn in this document tomorrow I would fill pages about you all.

I am fortunate to have had the chance to travel and meet wonderful people in the physics world outside of Brown. I look forward to collaborating with the friends I've made around the country: Andrew Hearin, Gabe Lee, and Eric Baxter.

Finally, the long view is perhaps most important. I would not be in my position now but for the love and support of my entire family and longtime friends. In particular, I am so grateful for my twenty year friendship with Jason Su, whom I've been connected with since elementary school. As time goes on I realize just how very lucky I am to have the family I do. My mom and dad, Wendy Geringer and Bob Sameth, and especially my brother and dearest friend Ethan, are such valuable parts of my life. It is hard to express what a luxury it is to have had their unending love and encouragement every day of my life. My grandparents Eda and Leonard Geringer provided an infinitely warm, comfortable, and supportive environment for all of the grandkids. Thank you to my aunt and uncle, Kim Geringer and Colin Dunn, and my dear cousins Rachel and Adam for being such a major part of my life. Our group of ten has been together for many many milestones. My brother's graduation was the first one that our grandmother Eda has missed; mine will be the second, and all the ones that follow will be without her as well. But it is a beautiful thought that so much of our characters, temperaments, senses of humor, and, yes, manners, were indelibly touched and shaped by her life and her love for us — what a blessing her memory is.

Contents

Vitae iv

Acknowledgments viii

1 Introduction 1
- 1.1 Cosmology is applied physics . . . 3
- 1.2 A combination of concordant theories . . . 4
  - 1.2.1 Big bang nucleosynthesis and the concept of freeze-out . . . 6
  - 1.2.2 Cosmic microwave background . . . 8
  - 1.2.3 Structure . . . 10
  - 1.2.4 Dark matter is cold . . . 11
- 1.3 Astroparticle physics: What *is* dark matter? . . . 12
  - 1.3.1 Example: Supersymmetry . . . 12
  - 1.3.2 WIMPs . . . 14
  - 1.3.3 Relic abundance . . . 14
- 1.4 The experimental effort . . . 20
  - 1.4.1 Annihilation and indirect detection . . . 20
  - 1.4.2 Scattering and direct detection . . . 28
  - 1.4.3 Capture and annihilation in solar system bodies . . . 31
  - 1.4.4 Creation and colliders . . . 31
- 1.5 Structure of this thesis . . . 32

2 Search for continuum annihilation from dark matter 34

3 Development of the event weighting framework 50
- 3.1 Hypothesis testing and confidence intervals . . . 51
  - 3.1.1 Test statistics . . . 52
- 3.2 General form of the test statistic . . . 53
- 3.3 Designing the weight function . . . 54
  - 3.3.1 Signal-to-noise method . . . 57
  - 3.3.2 Likelihood ratio method . . . 59

3.4 Probability distribution of the test statistic . . . 62
3.5 Carrying out the tests . . . 63
3.6 Expected results . . . 64

4 Search for gamma-ray lines 67

5 Detecting unresolved moving sources in a diffuse background 80
5.1 Introduction . . . 81
5.2 Overview of the problem . . . 82
5.3 Definitions . . . 86
5.4 2-dimensional model . . . 89
5.4.1 Ingredients . . . 89
5.4.2 The form of $V(p)$ in 2 dimensions . . . 91
5.4.3 Coordinate systems . . . 92
5.4.4 The form of $\xi(V)$ in 2 dimensions . . . 94
5.5 The error in ξ . . . 96
5.6 Point spread function and computational considerations . . . 98
5.7 Examples of the 2-Dimensional formalism . . . 101
5.7.1 Example 1: Moving sources only . . . 103
5.7.2 Example 2: Moving sources and a random component . . . 105
5.7.3 Example 3: Moving sources, fixed sources, and a random component . . . 108
5.8 Objects in 3 dimensions . . . 109
5.8.1 Summary of the measurement of ξ . . . 111
5.8.2 The form of $V(p)$ in 3 dimensions . . . 112
5.8.3 Ingredients needed to derive $C(p;V)$ in 3-D . . . 115
5.8.4 Derivation of $C(p;V)$ in 3 dimensions . . . 116
5.8.5 The form of ξ in 3 dimensions . . . 120
5.8.6 Mock Fermi search for solar system bodies . . . 122
5.8.7 Errors and flux-limited vs. counts-limited surveys . . . 125
5.9 Generalizations . . . 127
5.9.1 Including spectral information . . . 127
5.9.2 n-point functions . . . 128
5.10 Discussion and Conclusions . . . 128

6 Extracting the unresolved pulsar contribution to the gamma-ray background 135
6.1 Introduction . . . 136
6.2 General Methodology . . . 138
6.2.1 Cookbook . . . 141
6.3 Specific implementation . . . 142
6.3.1 Choice of periodicity test . . . 143
6.3.2 Statistics of the power spectrum peak for random data . . . 146
6.3.3 Statistics of the power spectrum peak when a pulsar is present 147
6.3.4 Rejecting the null hypothesis of "No pulsars" . . . 150

6.4 Application to Fermi-LAT . . . 152
6.4.1 Results . . . 155
6.5 Discussion . . . 160
6.5.1 Caveats and Improvements . . . 161
6.5.2 Pulsar population parameter estimation . . . 166
6.6 Conclusions . . . 168

A The A test **170**
A.1 Motivation . . . 171
A.2 Details . . . 173
A.3 Properties of A . . . 175

Bibliography **178**

List of Figures

2.1 This figure illustrates the ingredients and data required to derive upper limits on the dark matter annihilation cross section. Each plot corresponds to a different dwarf galaxy. Sampling the counts in 0.5° regions surrounding each dwarf results in an empirical background probability mass function (PMF) shown in red. The blue curves are Poisson distributions having the same mean as the empirical background PMFs. The vertical line represents the number of counts observed in the ROI centered on the dwarf's location. The dashed curve is the convolution of the background PMF with the Poisson distribution representing the contribution from dark matter annihilation when $\Phi_{\rm PP} = 5.0 \times 10^{-30}\,{\rm cm}^3\,{\rm s}^{-1}\,{\rm GeV}^{-2}$ (the 95% upper limit on $\Phi_{\rm PP}$). This convolution is the probability distribution of the sum of signal and background. The label w is the weight given to each dwarf in the construction of Neyman confidence belts. It is given by the ratio of the strength of the expected dark matter signal to the mean expected background. 40

2.2 Illustration of the Neyman confidence belt construction used to generate upper limits on $\Phi_{\rm PP}$. Each axis represents the number of events that could be observed from a given dwarf (here, Dwarf A has a larger J value than Dwarf B does). The shaded area, bordered by the solid line, represents the confidence belt for a particular value of $\Phi_{\rm PP}$. The dashed lines are the borders of the confidence belts for different values of $\Phi_{\rm PP}$, with $\Phi_{\rm PP}$ increasing from left to right. The borders are chosen to be normal to a vector of "sensitivities", which weights each dwarf according to the relative strength of its dark matter signal. Once a measurement is made (shown by the star) the confidence interval for $\Phi_{\rm PP}$ contains all values of $\Phi_{\rm PP}$ whose confidence belt contains the measured point. The dotted line shows the border for an alternative construction of the confidence belts which gives equal weight to each dwarf. 42

2.3 Derived 95% upper limit on $\langle \sigma_A v \rangle$ as a function of mass for dark matter annihilation into $b\bar{b}$ and $\tau^+\tau^-$. The shaded area reflects the 95-percentile of the systematic uncertainty in the dark matter distribution of the dwarfs. The canonical annihilation cross section for a thermal WIMP making up the total observed dark matter abundance is shown by the dashed line. The inset figure shows detail for lower masses. 45
2.4 Dark matter annihilation cross section limits for various Standard Model final states. The best-fit J values are assumed to avoid the clutter of the systematic error bars. The curves are for annihilation into $b\bar{b}$ (red), $\tau^+\tau^-$ (blue), W^+W^- (black), and $\mu^+\mu^-$ (green). Annihilation into other quark final states gives nearly identical results as for $b\bar{b}$. 47

4.1 A snapshot of every photon having an energy between 10 GeV and 1 TeV that has been detected within 1° of each of the seven dwarfs. The black dashed line is at 130 GeV [182, 183]. The gray region is ±15% around 130 GeV, a rough gauge of the energy dispersion of the LAT. The vertical axis is scaled according to solid angle so that an isotropic distribution of photons will be spread uniformly along this axis. 75
4.2 Results of the a search for line emission using an optimized combined search of seven dwarf galaxies. The horizontal axis represents the energy of the gamma-ray line searched for. The left vertical axis is the significance of the detection (in terms of Gaussian standard deviations). The right vertical axis incorporates a trials factor of 24, roughly the number of independent energies searched. The non-significant peak at 200 GeV is due to a single photon from Sculptor (see Fig. 4.1). 77
4.3 95% upper limits on $\langle \sigma_A v \rangle$ for annihilation into a pair of photons each having energy E_γ. The black line is the limit using the best fit J values for the dwarfs. The blue region corresponds to the 95% systematic uncertainty in the estimates of J. The two points are the dark matter interpretations for the tentative signals observed by [182, 183] under the assumption of an Einasto dark matter profile and annihilation into two gamma-rays, with 95% error bars. 78

5.1 Illustration of the two limits in the problem. The upper figure contains 5 objects each with event rate 10 and the one on the lower left contains 50,000 objects with event rate 0.01. The lower two figures contain the same number of events but those on the right are distributed randomly. Naively, it is impossible to tell which of the last two figures contains random events and which contains moving objects. 83

5.2 For a galaxy-galaxy correlation function we look in rings of a certain size centered on each galaxy and count the number of galaxies that lie inside each ring. The ring shown is $V(p)$, centered on the galaxy (represented by the black $\times$) having coordinates p. 88
5.3 The spacetime regions $V(r_1, r_2;\, t_1, t_2)(p)$ and $V(v_1, v_2;\, t_1, t_2)(p)$ where p is at the origin. The vertical axis is time and the horizontal axes are the x and y coordinates. In the upper figure the region between the two cylinders contains all events which have a radial distance from p between r_1 and r_2. In the lower figure the region between the two cones represents the possible worldlines of an object starting at p and having a speed between v_1 and v_2. Imposing a time separation between t_1 and t_2 gives the filled regions. 90
5.4 A toy example demonstrating the use of the spacetime correlation function to discover the presence of localized event sources with non-zero speeds. The $t = 0$ slice of $\xi(v, t)$ is plotted showing the theoretical prediction (red $\times$'s), the measured value (blue squares), and the measured value for the case of completely random events (black triangles). The hypothesis that the pattern of events in the sky map is Poisson ($\xi(v, t) = 0$) is clearly rejected at high significance. The error bars in the measured quantities are explained in the discussion surrounding (5.16). The sky map contained 3.5 million events, all from moving objects, though each object contributed only 0.1 events on average. The blue data points are measured from a larger version of the map shown in the lower left panel of Fig. 5.1 while the black points are measured from a larger version of the map shown in the right panel. . 104
5.5 The 2-point function ξ measured for two simulations color-coded as in Fig. 5.4. Each contained 7 million events. Objects had the same event rate as the first simulation. *Top:* Moving sources and random noise. Half the events came from moving objects and half were generated completely randomly to represent noise. *Bottom:* Moving sources, stationary sources and random noise. A third of the events are from moving objects, a third from stationary objects, and the last third were generated randomly. 107
5.6 *Top*: All events which occured in an area of the sky map with dimensions 150×150 during the entire observation time. *Bottom*: The same events but identified as objects (blue) and random events (orange). Events which came from the same object are connected with a line. Less than 5% of events come from objects which caused more than one event. 110

5.7 Results from a simulation of moving objects in the solar system, along with stationary sources and random noise. The correlation function is plotted for angular velocities between 0 and 500°/yr. Red ×'s represent the theoretical value of ξ calculated from (5.36) while the blue squares show the measured value of ξ from the sky map. The width of each angular velocity bin is 20°/yr. Error bars are derived using (5.16). The spike at zero angular velocity is due to the presence stationary background sources. The correlation function is also non-zero between $\omega = 196°$/yr and 389°/yr, corresponding to moving sources orbiting between 0.95 and 1.5 AU. 124

6.1 A demonstration of the statistical power of the method to detect the presence of pulsars over the entire sky. The color coding represents the probability of rejecting the null hypothesis of "no pulsars" at 99.7% significance. Φ_p is the photon flux of each individual pulsar in the energy range $[0.8 - 6.4]$GeV. The quantity γ represents the fraction of the total gamma-ray background due to pulsars. Solid contours give the number density of pulsars (in units of pulsars per square degree). The proposed method can reveal the presence of a pulsar population contributing as little as 10^{-3} of the diffuse gamma-ray background. Note that, within the range of pulsar fluxes shown, every individual pulsar is *flux*-unresolved because Φ_p is less than LAT's point source sensitivity threshold. Many of these flux-unresolved sources may be individually discovered based solely on an analysis of their time series: the dashed line represents the 5σ detection threshold for individual pulsars based on the height of their power spectrum peak (see text for details). 156

6.2 Same as Fig. 6.1 but for an observation area of 1,000 square degrees corresponding to a study of the Galactic center. Here, solid contours depict the total number of pulsars present in the observed region. The dashed line denotes the 5σ detection threshold of individual pulsars based on power spectrum peak height as in Fig. 6.1. 159

Chapter One

Introduction

The past hundred years has seen the birth and development of two successful and far-reaching theories in physics. Cosmology describes the structure and evolution on the largest scales while the Standard Model of particle physics explains the interactions between elementary particles. Both theories have proven to have remarkable explanatory power when applied to diverse observations.

For most of the twentieth century these fields proceeded in parallel, each without input from the other. By the 1970s both cosmology and particle physics stood on solid experimental foundations. However, the standard cosmological model appeared to require the existence of a new type of matter in great abundance: **dark matter** dominated the structure, dynamics, and stability of galaxies. Around the same time several conceptual conundrums of the Standard Model could be solved by extensions which predicted the existence of new species of particles at the weak scale. Perhaps these candidate theories could explain the cosmic dark matter as well.

Beginning in the 1970s and 1980s a remarkable confluence between disciplines began and serious consideration arose about the microscopic nature of dark matter. If it was a new particle, what were its properties? How did it fit into the current taxonomy of elementary particles and how did it interact with them? Could experiments and observations be performed that would reveal the nature of dark matter? The modern field of astroparticle physics seeks to answer this question. In this thesis I will describe progress toward understanding the nature of dark matter particle through astrophysical observations.

1.1 Cosmology is applied physics

Modern cosmology is an edifice built out of a collection of interdependent theories. In fact, cosmology has never been a fundamental branch of physics in the manner of electromagnetism or quantum theory. It does not postulate the existence of new physical objects (like electromagnetic fields and wave functions) and new dynamical laws that describe them. It does not require us to alter our interpretations of reality as we must do to conceive of relativistic spacetime or that the world is described by superpositions of quantum states. At an essential level, cosmology is the application of general relativity, thermodynamics, nuclear physics, and particle physics within the framework of an expanding universe.

For example, our modern cosmological model is based on the simple "Cosmological Principle" that space is homogeneous and isotropic [5], an assumption well borne out by observation [e.g. 6]. We know that general relativity governs the dynamics of space on large scales and so we are immediately led to equations governing the structure and evolution of such symmetric spacetimes [7–9]. The spacetime is described by the Friedmann metric which contains a single dynamical quantity, the scale factor $a(t)$. The scale factor governs how the proper distance between two freely-falling observers (e.g. those living in "typical" galaxies) changes with time. Generically, $a(t)$ is not constant but grows over time. The observational consequence is an apparent expansion of the Universe: distant galaxies appear to recede from us, and the more distant the galaxy, the faster it recedes [10, 11].

The time-evolution of the scale factor is determined by the contents of the Universe — the energy densities of matter, radiation, and dark energy — through the

Friedmann equation

$$H^2(t) + \frac{kc^2}{a^2(t)} = H_0^2 \frac{\rho(t)}{\rho_{\rm crit}}, \tag{1.1}$$

where $H = \dot{a}/a$ is the Hubble constant, H_0 is its value today, $\rho_{\rm crit} = 3H_0^2/(8\pi G)$ is the critical density of the Universe today, $k = -1$, 0, or 1 describes the intrinsic curvature of space, and $\rho(t)$ quantifies the energy density in the various constituents of the Universe; it is the sum of the densities of all types of particles, radiation, and dark energy (or an effective density due to a cosmological constant). We will use the notation $\Omega_i = \rho_i/\rho_{\rm crit}$, where i labels a component contributing to the energy density (e.g. non-relativistic matter, photons), and ρ_i is the value of the density at the present time.

Every species of particle we know of is present in the Universe to a greater or lesser extent and contributes to the total $\rho(t)$. Therefore, the balance of species in the Universe controls the expansion rate. On the other hand, the expansion history affects the particle content through thermodynamic processes (e.g. changing density and temperature) coupled with particle interactions (e.g. particle-antiparticle creation and annihilation, Coulomb scattering, and nuclear fusion and decay). This interplay between the dynamics of spacetime and the contents of the Universe provides a fertile framework for making testable predictions.

1.2 A combination of concordant theories

There are a number of individual theories which explain various aspects of the observable Universe. All of them rely on a set of basic ingredients. Observations show that on the largest scales the Universe is homogeneous, isotropic, and can be described by a spatially flat metric ($k = 0$ in Eq. 1.1). The matter in the Universe is composed

of photons, "baryons"[1] (protons, neutrons, electrons and positrons), three neutrino species, and cold dark matter. The dark matter, as far as existing observations have constrained it, is a phenomenological category and does not involve any microscopic understanding of particle interactions. In the standard cosmological model, cold dark matter is some substance which couples to the metric (has gravitational mass) and has no known interactions either with itself or with particles of the Standard Model. It is "cold" in the sense that it behaves as a non-relativistic fluid with small velocity dispersion at least as far back as the time when the Universe had a temperature $T \gtrsim$ MeV. While all extant observations are consistent with dark matter having no interactions with the Standard Model this is not required. In fact, discovering such interactions will be key if we wish to have a microscopic understanding of the nature of dark matter — an idea that will concern us over the next hundred or so pages.

Along with a set of initial conditions on the nature of metric and curvature perturbations in the early Universe, these ingredients suffice to compute a multitude of effects. The particulars of these effects depend on the various values of the cosmological parameters (e.g. on the abundance of baryons Ω_b or of cold dark matter Ω_c). At the present time, all cosmological observations can be explained by a *particular* set of these values. That is, a diverse abundance of phenomena support a common model. In this model Ω_c is required to be greater than 0 with extremely high confidence. In fact, baryonic matter makes up only about 15% of all matter ($\Omega_b = 0.183\,\Omega_c$) [12].

In the following sections I will review the combination of independent probes, spanning vast spatial scales and all temporal epochs, that together provide firm evi-

[1] When discussing the energy density of normal matter (e.g. non-relativistic particles of the Standard Model) I will refer to all such matter as baryons. While leptons (electrons and Standard Model neutrinos) play a vital role in many cosmological phenomena, their contribution to the energy density is negligible compared with that of the protons and neutrons. The energy density of non-relativistic particles is equivalent to their mass density. The neutrality of the Universe requires equal numbers of protons and electrons but the mass of a nucleon is $\sim 1800\times$ that of an electron.

dence for the standard cosmological model, including the existence of a vast amount of cold dark matter in the Universe.

1.2.1 Big bang nucleosynthesis and the concept of freeze-out

The light atomic nuclei were built up by nuclear processes during the seconds and minutes after the big bang [e.g. 13–20]. Therefore, measurements of the abundances of these elements are a direct probe of the conditions in the Universe at these early times. The following description of big bang nucleosynthesis serves two purposes. First, the theory allows for the determination of the total baryonic matter density, therefore pointing to the existence of additional (dark) matter. Second, big bang nucleosynthesis illustrates the concept of the freeze-out of particles as they decouple from thermal equilibrium. In Sec. 1.3.3, I will describe how this freeze-out mechanism can naturally explain the abundance of dark matter in the Universe.

When the temperature of the Universe is above about[2] 1 MeV protons and neutrons are kept in equilibrium by the weak interactions:

$$\mathrm{n} + \nu_\mathrm{e} \rightleftharpoons \mathrm{p} + \mathrm{e}^- \qquad\qquad \mathrm{n} + \mathrm{e}^+ \rightleftharpoons \mathrm{p} + \bar{\nu}_\mathrm{e} \tag{1.2}$$

Equilibrium between particles is maintained as long as the relevant reaction rates are sufficiently fast. The cosmological expansion provides a natural timescale to compare with a given reaction rate: the Hubble parameter $H = \dot{a}/a$ is a measure of the instantaneous expansion rate. Intuitively, if the reaction rate Γ for a process

[2] It is important to note that nuclear interactions at MeV energies are quite well understood and tested experimentally on Earth. The early Universe is simply a particular laboratory in which nuclear reactions took place, the only intricacy being the concurrent expansion of space.

is larger than H the process occurs many times before the Universe can appreciably expand. If $\Gamma \ll H$ the process will not have a chance to occur before the present day. This is handwaving but the intuition is correct. A thorough analysis based on the Boltzmann equation makes the analysis rigorous and bears out this simple interpretation (see discussion in Sec. 1.3.3.

Conditions for equilibrium change because of the Universal expansion. The Hubble parameter is a dynamical quantity. So is the reaction rate $\Gamma = n_T \langle \sigma v \rangle$, where n_T is the number density of target particles and $\langle \sigma v \rangle$ is the velocity-averaged cross section for the process [e.g. 9, 21]. Both factors in Γ can change with time; in particular, $\langle \sigma v \rangle$ changes because the velocity distribution of a species is a function of its temperature.

In the case of big bang nucleosynthesis the relevant reactions are those shown in Eqs. 1.2. The reaction rate for these processes is $\Gamma_{\mathrm{n} \leftrightarrow \mathrm{p}} \propto T^5$, while the expansion rate in the radiation dominated era is $H \propto T^2$ (where T is photon temperature). Thus, as the temperature drops the reaction rate falls below the Hubble rate and this occurs around $T \sim 1$ MeV.

From this time on, the abundance of protons and neutrons are not determined by equilibrium statistics and neutrons will either become bound up in nuclei or decay. The buildup of nuclei proceeds through various reaction networks, which in the process produce (among other nuclei) deuterium, lithium, and helium. The formation of these nuclei does not begin until about a minute after the big bang, when the temperature of the Universe is far below the binding energy of nuclei. This is because the high density of radiation photo-dissociates nuclei as soon as they form and the formation can only proceed once the temperature is sufficiently low. The key point is that the abundances of nuclei are controlled by the baryon-to-photon

ratio η. Accurate measurements of the cosmic microwave background temperature (hence the photon density), allow a conversion between η and the cosmic density of baryons Ω_b.

One can predict the fraction of baryonic mass in the form of ^{4}He (and other nuclei) as a function of η. When the helium fraction is measured (e.g. in extremely metal-poor galaxies and gas clouds) it is found to be $Y_{\rm p} = 0.249 \pm 0.009$ [20, 22–25], corresponding to a particular value of η. The measured abundance of deuterium is more sensitive to η and is found to be in excellent agreement with the value derived from the helium abundance [e.g. 26–28].

1.2.2 Cosmic microwave background

Even after nucleosynthesis took place the temperature of the primordial Universe was still too high to allow the recombination of electrons with nuclei into neutral atoms. When the temperature dropped below ~ 0.3 eV the ionized plasma became neutral [e.g. 29–31]. Shortly thereafter, photons stopped scattering off of electrons and travelled freely, making the Universe "transparent". As with nucleosynthesis, these events are governed by the balance between cosmic expansion and cooling and the time scales for particle interactions (in this case Thompson and Compton scattering of photons on electrons and the ionization-recombination of neutral hydrogen). This entire process — from ionized to neutral along with the photon decoupling — occurred over a rapid timescale and the free-streaming photons can be observed today in the form of the cosmic microwave background (CMB). The detection of this relic radiation [32, 33] was a major achievement in support of the big bang and the thermal picture of the Universe.

Because the recombination process took place over such a short period, the microwave background radiation we observe today was essentially emitted from a very thin shell. Therefore, the image of this radiation represents a snapshot of the early Universe. The linear growth of primordial perturbations [e.g. 9, 34] leaves a characteristic imprint on temperature fluctuations of the CMB [35, 36]. Thirty years after the discovery of the CMB the anisotropies induced by gravitational perturbations were measured by Smoot *et al.* [37]. The key observable is the correlation function of temperature anisotropies across the sky. This is represented as a power spectrum (correlation as a function of wavenumber). Recent studies of the shape of this power spectrum [e.g. 38, 12, 39, 40] have led to impressively precise measurements of cosmological parameters.

The physics governing the structure of the CMB anisotropies can be solved nearly exactly because, at the relevant times and observable angular scales, perturbations were small enough to be treated by first order perturbation theory to an excellent approximation. The mathematical structure describing the growth of perturbations is quite similar to that of a harmonic oscillator [34, 41]. The Universe was seeded with metric perturbations at very early times. When a perturbation enters the horizon it begins to grow due to gravitational collapse. The perturbation attracts matter and radiation. However, radiation pressure of the photons resists the collapse. The result is that the amplitude of the perturbation behaves similarly to a harmonic oscillator. Baryonic matter, tightly coupled to radiation by Compton scattering, is analogous to the mass of the oscillator. That is, it affects the amplitude of the oscillations. Cold dark matter, on the other hand, interacts with the photons and baryons only through gravity and is therefore much more weakly coupled to the photons. The complex (but treatable) balance between metric perturbations and matter/radiation perturbations is partially tuned by the abundances of the various components (e.g.

Ω_c, Ω_b). The latest results from the Planck collaboration indicate that $\Omega_c = 5.451\,\Omega_b$ — there is a matter component in the Universe which does not couple to photons in the way that baryonic matter does.

1.2.3 Structure

The observational confirmation of the theories of big bang nucleosynthesis and CMB anisotropies do far more than reveal the presence of dark matter in the Universe. They give insight into physical processes which took place when the Universe was very young. In contrast, dark matter makes its presence known through the dynamics and formation of structure at the present time. In fact, evidence that there is unseen mass in galaxies and galaxy clusters predated the precision measurements discussed earlier [e.g. 42–46].

The visible Universe we see today is populated by galaxies which are arranged into groups and clusters. The kinematics of the visible material in these objects is governed by all the mass in the system, not just the baryonic mass. Generally, one studies the distribution of visible matter through optical observations and compares this to total mass inferred from dynamics. For instance, the light emitted by a galaxy is a tracer of its baryonic mass, and the cataloguing of stellar populations allows a more or less robust correspondence between baryonic mass and luminosity. For galaxy clusters, most of the baryonic mass is in the form of hot x-ray emitting gas. The temperature and luminosity of the gas can be related to its density and pressure using relatively straightforward thermodynamics. The assumption of hydrostatic equilibrium of the system leads to conclusions about the gravitational pressure exerted by the total mass in the cluster. Gravitational lensing induced by a cluster can also be used to determine its total mass, metric deformations being

insensitive to the type of mass in the system. Recently, colliding clusters of galaxies have been studied which show a clear separation between the baryonic gas and the dark matter [47–49]. As the clusters passed through each other the gas, being a collisional system, is disrupted and bow shocks form. Mass maps made through lensing, on the other hand, show that the non-interacting dark matter halos of the two clusters passed directly through each other. In general, a vast array of astrophysical systems all show the presence of an unseen and non-interacting cold dark matter component [e.g. 50–53].

1.2.4 Dark matter is cold

Currently, all the evidence we have about dark matter comes only by virtue of its gravitational attraction with itself and with normal matter and radiation. A vital clue that may point toward the nature of dark matter is the evidence that dark matter in the Universe is cold, i.e. it behaves as a non-relativistic particle. This is a requirement of the theory of structure formation. In order to reproduce the observed power spectrum of density fluctuations at small scales dark matter must have a very small velocity dispersion. If dark matter posses significant velocities (i.e. is hot) small-scale structure will be unable to form. The upshot would be a suppression of the matter power spectrum at small scales [e.g. 54–57]. Simulations also confirm this requirement of minimal velocity dispersion [e.g. 58–60]. The concept of "warm" dark matter is viable, though constraints on its abundance exist [e.g. 61–65]. The constraints on the primordial velocity dispersion of dark matter can directly translate to requirements on its particle mass in individual theories [e.g. 61].

1.3 Astroparticle physics: What *is* dark matter?

I don't know — but this thesis documents progress towards answering the question. The wealth of cosmic observations over the past century firmly establishes the existence of dark matter in the Universe. In fact, dark matter's fundamental role in cosmology is matched only by its conspicuous absence from the very successful Standard Model of particle physics. Any explanation of the nature of dark matter will require new physics beyond the Standard Model. What sort of particle is the dark matter and how does it interact with those of the Standard Model? These central questions, lying at the boundary of astrophysics and particle physics, are the subject of a vast contemporary experimental and observational effort.

The convergence of the fields of astrophysics and particle physics began as the Standard Model was becoming confirmed experimentally. A number of problems and coincidences were quickly identified which all seemed to point toward the existence of new physics at the weak scale. Such theories generally entail existence of a new particle having properties consistent with cosmic dark matter. Furthermore, the new particle will have (feeble) interactions with the Standard Model, which directly leads to the prospect of detection and discovery.

1.3.1 Example: Supersymmetry

From an internal consistency perspective, the naive Standard Model seems to require extreme fine-tuning to keep the mass of the Higgs boson light [e.g. 66]. The electroweak symmetry breaking mechanism contains a parameter associated with the Higgs mass, a quantity directly measured to be 125 GeV [67, 68]. However, one

expects this mass parameter to receive quantum corrections from virtual loops of all particles to which the Higgs couples (quarks and leptons in particular). The correction from each such loop is quadratically divergent unless cut off at some energy scale, e.g. when some new physics becomes important. The next energy scale we know of above the electroweak scale is the Planck scale, about 17 orders of magnitude larger than the Higgs mass. Therefore, each quark and lepton contributes a term of order 34 orders of magnitude to the (squared) Higgs mass. In order to have a 125 GeV Higgs, these terms would have to cancel with a stupendous degree of precision.

This exact canceling does arise naturally if the Standard Model is extended to include supersymmetry (SUSY). In analogy to CP symmetry which relates particles and antiparticles, SUSY is a symmetry between fermions and bosons. This implies at least a doubling of the number of particles: every particle has a supersymmetric partner with spin different by 1/2. Members of a pair (or multiplet) will exactly cancel each other's corrections to the Higgs mass (up to a logarithmic divergence) [e.g. 69]. For consistency with experimental constraints, SUSY particles need to be heavier than their Standard Model partners — i.e. SUSY must be broken. Again, to keep the Higgs mass where it is, this breaking scale must be around the weak (TeV) scale. The lightest of these SUSY particles have a mass at this scale and must also be stable, protected from decaying into Standard Model particles by so-called R-parity [70, 71]. This symmetry prevents lepton number and baryon number from being violated in supersymmetric extensions to the Standard Model (e.g. SUSY without R-parity allows proton decay). Thus SUSY provides a dark matter candidate: the lightest SUSY particle is a stable particle with a mass at the weak scale, a so-called WIMP.

1.3.2 WIMPs

Supersymmetry is but one of a number of extensions to the Standard Model that provide a dark matter candidate. I will not describe this zoo of theories in detail — see, for example, Bertone *et al.* [72, Sec. 3] — but there is a general, phenomenological class of models which arise in many different theories. These are the weakly interacting massive particles (WIMPs); massive, in this case, referring to particles in the GeV to TeV range. While often predicted from the particle physics world, WIMPs are, in some sense, a natural candidate from a cosmological perspective. The process of freeze-out predicts that WIMPs should exist today in significant abundance. Perhaps more importantly, the two properties (GeV masses and weak interactions) immediately imply a number of potential observable phenomena. In fact, nearly all the experimental probes search for a signal that depends simply on the mass of the particle and its various interaction cross sections. This class of models is therefore characterized by a very small set of parameters, making experimental and observational results relevant to a large class of models.

1.3.3 Relic abundance

As early as 1965 Zel'dovich had begun to tackle the issue of the relic abundance of new massive particles [73, 74]. In the West it would take another decade before the problem was taken up in earnest [e.g. 75–83, 21, 84]. As discussed in Sec. 1.2.1, the abundance of a species of particle is determined by balancing the expansion rate of the Universe with the rate of interactions keeping the particle in equilibrium. Here I will give a more thorough description of the calculation of the relic abundance. The result connects the (measurable) abundance of dark matter Ω_c with its annihilation

cross section $\langle \sigma_A v \rangle$. Thus cosmological measurements provide us with a quantitative estimate of a WIMP's interaction with the Standard Model.

The argument is powerful and general because it makes very minimal assumptions. Assume that a WIMP exists — i.e. there is some new particle χ which participates in weak interactions and has a mass $\gtrsim \mathcal{O}(\text{GeV})$. By virtue of its weak interactions, it has some cross section for annihilation with its antiparticle into Standard Model particles. Likewise, there is the chance that given enough energy, a collision of Standard Model particles can produce a $\chi\bar{\chi}$ pair. At early enough times, the temperature of the Universe is larger than the mass M_χ of the new particle and $\chi\bar{\chi}$ pairs are continuously being created and destroyed. During this time the number density of χ is governed by simple equilibrium thermodynamics,

$$n = n_{\text{R}} = \frac{3\zeta(3)}{4\pi^2} g_\chi T^3,$$

where n is the local number density (number of χ per volume), $\zeta(3) \approx 1.2$ is the zeta function, T is the temperature of radiation in the Universe (i.e. the photon temperature), and n_{R} is the equilibrium number density for a relativistic particle ($T \gg M_\chi$) [9]. The quantum degrees of freedom g_χ depends on what type of particle χ is. If χ is a Majorana fermion with spin 1/2 then $g_\chi = 2$ (in this case χ is its own antiparticle).

As the Universe cools, and the temperature falls below M_χ, the creation process no longer takes place because the average collision of Standard Model particles does not have enough energy to produce $\chi\bar{\chi}$. The abundance n begins to drop exponentially as the temperature decreases. It is important to note that this is still an equilibrium process — the annihilation rate and the Standard Model particle collision rate are large relative to the Hubble rate $H = \dot{a}/a$. In this regime the number

density goes as,

$$n = n_{\rm NR} = g_\chi \left(\frac{M_\chi T}{2\pi}\right)^{3/2} \exp\left(\frac{-M_\chi}{T}\right),$$

where $n_{\rm NR}$ is the equilibrium number density for a particle when the temperature is much less than the particle mass.

At some later time the annihilation rate drops below the expansion rate. After this point (known as freeze-out) χ particles can no longer find each other and annihilate. The system goes out of equilibrium and from this time forward the comoving number density of χ is constant. The physical number density today is simply

$$n_0 = n_{\rm f} \left(\frac{a_{\rm f}}{a_0}\right)^3, \tag{1.3}$$

where $n_{\rm f}$ is the physical number density at freeze-out and $a_{\rm f}$ (a_0) is the scale factor at freeze-out (today).

The present day abundance Ω_χ has simple dependencies on the phenomenological parameters M_χ and $\langle\sigma_A v\rangle$. First, Ω_χ is inversely proportional to $\langle\sigma_A v\rangle$. It is easy to qualitatively understand this behavior. After χ becomes non-relativistic its abundance starts to drop until the annihilation rate becomes too small. The annihilation rate (per particle) is given simply by

$$\Gamma = n\langle\sigma_A v\rangle. \tag{1.4}$$

The larger $\langle\sigma_A v\rangle$ the more time it takes before the annihilation rate becomes small. More $\chi\bar{\chi}$ pairs will have had time to annihilate and the total abundance will be lower.

Second, Ω_χ is independent of the mass of the WIMP. This is not an exact re-

sult but holds to an excellent precision over a wide range of WIMP masses. To see how this comes about one can perform the very simple derivation of the relic abundance layed out in Jungman *et al.* [69, Sec. 3.1]. Freeze-out takes place once the annihilation rate drops below the Hubble rate. Using Eq. 1.4 this condition is

$$H = n\langle\sigma_A v\rangle \quad \text{when } T = T_\mathrm{f}. \tag{1.5}$$

I assume that $\langle\sigma_A v\rangle$ is independent of time (equivalently temperature), an assumption I will return to later. The above equality determines n_f, the abundance at freeze-out. Equation 1.3 is then used to evolve n_f forward to today to find n_0. All that needs to be done is relate H and a to the temperature.

Matter-radiation equality occurs at a temperature of a few eV but the freeze-out process occurs when the temperature is approximately $T_\mathrm{f} \approx M_\chi/20$ [69]. Therefore, freeze-out takes place during the radiation dominated era of the early Universe. Inserting the energy density of blackbody radiation into Eq. 1.1 allows the Hubble rate to be written in terms of temperature:

$$H = 1.66 g_*^{1/2} \frac{T^2}{M_\mathrm{Pl}}, \tag{1.6}$$

where $M_\mathrm{Pl} \approx 10^{19}$ GeV is the Planck mass and g_* counts the degrees of freedom of all the relativistic species in the Universe contributing to the energy density at temperature T [e.g. 9] (it is about 70-100 at the relevant epochs [84, 69, 85]). The conservation of the entropy of the Universe can be used to relate the scale factor at freeze-out to the scale factor today. Entropy conservation takes the form $s_* a^3 T^3 =$ const, where s_* counts the number of degrees of freedom contributing to the entropy

density [e.g. 9]. Combining Eqs. 1.5 and 1.6 with entropy conservation gives

$$\rho_\chi = M_\chi n_0 = \frac{1.66}{M_{\rm Pl}} \left(g_{*\rm f}^{1/2} \frac{s_{*0}}{s_{*\rm f}} \right) T_0^3 \, \frac{M_\chi}{T_f} \frac{1}{\langle \sigma_A v \rangle}. \tag{1.7}$$

Finally, recall that the freeze-out temperature is proportional to the mass of the particle, eliminating both M_χ and T_f from Eq. 1.7. Normalizing to the critical density $\rho_c = 3(100h\,\mathrm{km/s/Mpc})^2/(8\pi G)$ we find the relic abundance of the WIMP

$$\frac{\Omega_\chi h^2}{0.120} = \frac{1.65 \times 10^{-26} \mathrm{cm}^3/\mathrm{s}}{\langle \sigma_A v \rangle}, \tag{1.8}$$

where I have set $g_{*\rm f} = s_{*\rm f} = 100$ [84], $s_{*0} = 3.91$ [86], $T_0 = 2.725\,\mathrm{K}$ [87] and $M_\chi/T_{\rm f} = 20$ [69]. The quantity 0.120 is the best-fit value of $\Omega_c h^2$ from Ade *et al.* [12]. The cross section required to explain the observed dark matter abundance is known as the thermal (relic abundance) cross section. The remarkable fact about the result in Eq. 1.8 is that $10^{-26}\,\mathrm{cm}^3/\mathrm{s}$ is at the scale of weak interaction cross sections. Nothing about the microphysics of the χ particle ever entered the calculation, in particular the strength of its interactions. The *cosmological observation* of $\Omega_c h^2 \sim 1$ itself points to the existence of a WIMP, a particular dark matter candidate. The effect of this "coincidence" on the direction of experimental and theoretical physics over the last 30 years cannot be overstated.

Before we move on, I would like to discuss the assumptions and approximations made in the above exercise. I supposed that χ is its own antiparticle. If this is not the case then Eq. 1.8 holds separately for χ and $\bar{\chi}$, leading to twice the *total* dark matter density compared to when $\chi = \bar{\chi}$. In this case, the cross section $\langle \sigma_A v \rangle$ must be twice as large in order to explain the observed relic abundance $\Omega_c h^2 = 0.120$.

In practice, the relic abundance must be calculated by using the Boltzmann

equation [e.g. 41] to formulate a differential equation for the abundance as a function of temperature. This procedure correctly takes into account the changing degrees of freedom $g_*(T)$ and provides a cross section accurate at the percent level [84].

I took $\langle \sigma_A v \rangle$ to be a constant, independent of temperature. Because the particles are non-relativistic at freeze-out the cross section can be expanded as, $\sigma_A v = a + bv^2 + \ldots$, where the first term represents s-wave annihilation and the second term represents a combination of s- and p-wave annihilation [e.g. 69]. These two terms suffice to treat most possible models. It is certainly possible to compute the relic abundance for purely p-wave (and higher) interactions but such models will have cross sections today that are extremely weak — well below the reach of current probes [84]. The velocity-averaging can be written in a way [21] that allows the computation of the relic abundance for complicated interactions (e.g. resonances or poles in the interaction amplitude) where the cross section cannot be simply expanded in powers of v^2.

Finally, the cross section required to reproduce the given relic abundance is not truly independent of the mass of the particle. For $M_\chi \gtrsim 10$ GeV the abundance Ω_χ has a logarithmic dependence on the mass and the approximation $\Omega_\chi h^2 \propto 1/\langle \sigma_A v \rangle$ is quite accurate. However, for particle masses below 10 GeV there is a significant variation due to the decreasing number of relativistic degrees of freedom as the strongly interacting quark-gluon plasma breaks up into mesons and eventually into baryons [84, 88].

1.4 The experimental effort

Weakly interactive massive particle dark matter is an attractive candidate from the theoretical point of view and if it exists, it exists in the right amount. It is also a testable theory and a large experimental effort over the past several decades has sought proof of the WIMP hypothesis. The WIMP category is general enough that these experiments are sensitive to a wide variety of specific particle models. WIMP phenomenology is based on three basic properties: particle mass, cross section for annihilation into Standard Model particles, and cross section for scattering off Standard Model particles. WIMPs may participate in other interactions and may have multiple cross sections describing interactions with various particles. But this simple set of interactions (annihilation and scattering) allows generic predictions of physical phenomena. If one assumes a specific model (e.g. supersymmetry) precise calculations can be performed and the masses and cross sections can be related to each other and to fundamental parameters of the theory.

1.4.1 Annihilation and indirect detection

This thesis is mainly concerned with the detection of WIMPs through the observations of Standard Model products of dark matter annihilation[3] . The search for WIMP annihilation is well-motivated because of the freeze-out process — WIMPs must have annihilated in the early Universe to explain their current abundance. However, the freeze-out mechanism, by its very nature, requires that annihilation cease after the expansion rate overtakes the per particle annihilation rate. This is

[3] Dark matter may also **decay** into Standard Model particles. The observable consequences are often quite similar to annihilation, though the details of calculating the expected signal differ. Generally any experiment designed to search for annihilation can place constraints on theories predicting unstable dark matter.

only true if one assumes a homogeneous distribution of matter that becomes more and more rarified as time goes on. In reality, inhomogeneities grow in the matter-dominated epoch and structure begins to form hierarchically (that is, small, dense regions collapse first and subsequently merge into larger halos) [e.g. 89, 29, 41]. In these overdensities dark matter can continue to annihilate (though never at a rate which affects its total abundance).

It makes sense, therefore, to seek direct evidence of annihilation in the local Universe as well as in the structure along any line of sight. The annihilation products can be observed directly and can emit secondary radiation which can be detected. Most probes search for high-energy particles as signatures of dark matter — since WIMPs are typically more massive than Standard Model particles the annihilation products are relativistic. In all of these searches the principal difficulty is distinguishing a signal from background. Astrophysical sources, both known and unknown, generate high-energy cosmic rays which can mimic a dark matter signal. In this section I will discuss the observational efforts to discover evidence of dark matter annihilation.

Dark matter must be electrically neutral and therefore produces equal numbers of particles and antiparticles in an annihilation event. In fact, the most likely outcome is the production of a particle-antiparticle pair. These products are relativistic and typically create cascades of other Standard Model particles. For instance, a pair of relativistic strongly-interacting particles (quarks, gluons, gauge bosons) will produce hadronic jets. These eventually give rise to all stable particles in the Standard Model: protons, electrons, gamma-rays and neutrinos (and their antiparticles) [90]. Dark matter annihilation into a pair of leptons again gives rise to all stable particles. The ratios of the final products depend on the annihilation channel — this is quantified by the collection of branching ratios B_f, the probability that an annihilation event produces final state particles f (see Eq. 2.2).

A vital ingredient required to predict annihilation rates is the distribution of dark matter in the system of interest (e.g. the Milky Way, nearby galaxies or clusters, or throughout the Universe). Typically this is done through kinematic analysis of the visible objects in the system combined with insights from N-body simulations. As will be seen later, such modeling of the distribution represents a major source of systematic uncertainty in WIMP constraints derived from astrophysical observations.

Antiprotons

Antimatter searches are attractive because background cosmic rays are dominated by matter (as opposed to antimatter). In particular, antiprotons make up a tiny fraction ($10^{-6} - 10^{-4}$ depending on energy) of cosmic rays [91]. They are produced by cosmic ray spallation on hydrogen atoms [92, 69]. These spallation processes, however, are unable to produce antiprotons with energies much below a few GeV. Such low energy antiprotons require a collision with a high energy primary protons but these events are rare since the proton energy spectrum falls sharply [93]. Antiprotons produced in WIMP annihilation suffer no such low energy cutoff. The current strongest measurements on the cosmic antiproton flux as well as the antiproton-proton ratio come from the PAMELA satellite [91, 94]. PAMELA measures the antiproton spectrum down to 60 MeV and observes the expected cutoff due to an astrophysical formation mechanism. Donato *et al.* [95] provide constraints on WIMP models based on the PAMELA antiproton spectrum. The Alpha Magnetic Spectrometer (AMS) [96] will soon provide a precise measurement of the antiproton (and perhaps antideuteron) spectrum.

Electrons and positrons

Cosmic ray electrons and positrons at GeV energies are extremely subdominant compared with protons. They lose their energy quickly in Galactic magnetic fields (traveling only a few kpc) [97] and therefore provide a probe of the local dark matter distribution. Furthermore, astrophysical uncertainty is minimized because of this localization.

Two notable features of the positron and electron spectra have been identified in recent years. The first is the fraction of positrons to electrons as a function of energy (see [98, Fig. 1] for a comparison of recent measurements). Unlike antiprotons, which are produced above a certain threshold by spallation, the positron fraction is expected to decrease with energy [99]. However, several experiments have now confirmed the surprising result that the positron fraction increases with energy above about 5 GeV. Of the current generation of detectors, PAMELA provided the first unambiguous detection of the excess [100]. The Fermi Large Area Telescope (LAT) [101] was able to make an independent measurement confirming the rising positron fraction to a slightly higher energy, though with a somewhat offset normalization [102]. AMS recently published a precision measurement of the positron fraction [103] that agrees nicely with the PAMELA result (above a few GeV). They also set an upper limit on the degree of anisotropy of the positron fraction signal.

This unanticipated finding is in stark contrast to conventional hypotheses on astrophysical sources of electrons and positrons. The feature is consistent with the injection of equal numbers of electrons and positrons [103] and was immediately seized upon as a possible discovery of dark matter annihilation (see e.g. [104] and *many* more). Dark matter, being cold, can only produce annihilation products with energies less than the mass of the WIMP. Therefore, an essential signature would be

the precipitous drop in the positron fraction at an energy equal to the WIMP mass. At the present time, the fraction continues to increase up to the energy limits that experiments can probe. In the future AMS will measure the positron fraction to higher energies, perhaps revealing the characteristic drop at the dark matter mass.

The second unusual feature associated with cosmic ray leptons was first reported by two balloon-borne cosmic ray detectors ATIC [105] and PPB-BETS [106]. These experiments measured the spectrum of electrons and positrons and found a significant "bump" around 400 GeV. Such a sharp feature is difficult to explain using conventional sources. Two years later Fermi published a more precise measurement of the total electron-positron spectrum [107] which did not contain such a pronounced bump. The Fermi spectrum, however, does appear to show some feature in the 200 GeV to 1 TeV range — perhaps a less pronounced bump.

The dark matter interpretation of both the positron fraction and the lepton spectrum features is somewhat difficult to explain. It would appear to require a "leptophillic" model, where dark matter annihilated to muons and antimuons or directly to electron-positron pairs to avoid disturbing the antiproton fraction [e.g. 95]. Furthermore, the annihilation cross section required is at least an order of magnitude larger than that required to reproduce the dark matter relic abundance. This concern can be mitigated if the Earth is particularly near a dark matter subhalo. On the other hand, it appears one or more nearby pulsars could be providing the requisite numbers of electrons and positrons to account for the positron excess and lepton spectrum [e.g. 108, 109]. Both hypotheses are the subject of very active investigation.

Neutrinos

Detecting neutrino annihilation products is a significant challenge. Beacom *et al.* [110] present a conservative upper limit on the dark matter annihilation cross section by assuming annihilation into neutrinos only. The flux from annihilation throughout the history of the Universe is calculated and data from three neutrino experiments is used to constrain any possible model. A more direct search by the IceCube collaboration set constraints on the annihilation cross section by searching for energetic neutrinos from the Galactic halo [111]. These searches are not yet competitive with other indirect probes but they offer the only prospect of detection if WIMPs annihilate predominantly into neutrinos. In Sec. 1.4.3 I will discuss another exciting prospect for WIMP detection from neutrinos, but this first requires a discussion of WIMP scattering.

Gamma-rays

The search for gamma-rays from WIMP annihilations is the main subject of this thesis. Photons and neutrinos are distinct from the other annihilation products in that they are electrically neutral — therefore, they do not bend in the Galactic magnetic field but travel in straight lines from their sources. This allows targeted searches of specific locations in the sky. The annihilation rate at some location is proportional to the square of the dark matter density at that location. High-density, nearby regions are therefore the most attractive targets in principle. However, astrophysical contaminants are typically more numerous in highly dense regions. There is often a tradeoff, therefore, between strong signal and low backgrounds.

There are many targets for dark matter searches with gamma-rays. The closest is

the Galactic center, about 8 kpc away. Numerical simulations uniformly predict that dark matter halos have central density peaks. However, the exact matter distribution within such a peak strongly affects the expected annihilation signal. For galaxies, the central regions are dominated by baryonic matter, which is very difficult to simulate numerically. The upshot is that the dark matter distribution near the center of our galaxy is subject to large uncertainties. There is also the issue of astrophysical backgrounds. The Galactic center is home to a concentrated population of gas clouds, supernova remnants, and pulsars. Thus it is not surprising that LAT data show significant gamma-ray emission from the Galactic center. What is more interesting is recent work showing that the emission is spatially extended and spectrally consistent with annihilation of a low mass ($M_\chi \sim$ 10–30 GeV) dark matter particle [112–114] (see also [115]). Other authors have suggested that the unconstrained population of pulsars at the Galactic center explain the signal [116, 117]. Searches of other targets (e.g. dwarf galaxies [e.g. 1, 118]) can provide a check on the dark matter hypothesis.

The all-sky survey of Fermi allows for the search for emission from elsewhere in the Galactic halo. That is, one can look away from the disk (heavily contaminated by astrophysical point sources and emission from gas) and search for gamma-ray annihilation at slightly higher galactic latitudes. Ackermann *et al.* [119] have used this strategy to place limits on the WIMP cross section. The results are highly dependent on the modeling of the density profile of the Galactic halo. Depending on the choice of profile the limits are within an order of magnitude of the relic abundance cross section (Eq. 1.8).

Beyond the Milky Way, nearby clusters of galaxies may be detectable in gamma-rays. Clusters contain more dark matter mass than in any other collapsed objects in the Universe and the densities at their centers should by quite significant. No clusters have been unambiguously detected in gamma-rays yet. However, even if one

were to be seen, it would be unclear whether the emission was due to dark matter annihilation — clusters are filled with hot gas which is known to emit gamma-rays through cosmic ray collisions that produce pions. Currently, clusters provide gamma-ray constraints on the annihilation cross section that are several orders of magnitude above the thermal cross section [120–126]. There is currently no way to probe the substructure in clusters. Depending on the distribution of dark matter in subhalos of various densities the predicted annihilation signal can vary by orders of magnitude.

Finally, one can consider dark matter annihilation along a line of sight throughout the entire history of the Universe. This should give rise to a completely isotropic gamma-ray signal. The amplitude of the emission depends on the formation history of cosmic structure, and is particularly sensitive to the nonlinear evolution. Semi-analytic and numerical solutions can be used to get a handle on the history of the the nonlinear structure but uncertainties remain. At cosmological distances, gamma-rays may be attenuated by pair production of electron-positron pairs in interactions with starlight and the cosmic microwave background. The current measurement of the isotropic gamma-ray background can be found in Abdo *et al.* [127]. There are numerous astrophysical contributors to this background including star forming galaxies, active galactic nuclei including blazars, and unresolved gamma-ray bursts. Additionally, local populations of unresolved sources such as Galactic pulsars and Solar System bodies may masquerade as an extragalactic background. Current dark matter constraints based on the isotropic gamma-ray background can be found in [e.g. 128–130].

The future of gamma-ray astronomy is a combination of space-based and ground-based detectors. Fermi will continue to operate for the foreseeable future and will eventually release a complete re-analysis of their data, increasing the effective area, angular resolution, and energy resolution of the instrument. The AMS-02 experi-

ment has just begun releasing results and is sensitive to photons as well as charged particles.

On the ground, imaging atmospheric Cherenkov telescope arrays (ACTs) can detect gamma-rays at even higher energies (up to hundreds of TeV) [131]. These telescopes detect Cherenkov radiation emitted by the shower of particles created when an energetic photon strikes an atom in the atmosphere. The shower direction and energy can be reconstructed through observations of the Cherenkov cone by multiple separated telescopes. The angular resolution of these detectors is generally much better than that of Fermi. Unlike Fermi, ACTs perform pointed observations and have a small field of view, making it difficult to measure the isotropic gamma-ray flux. However, ACTs are well suited to perform deep observations of dark matter dominated targets like the Galactic center and nearby dwarf galaxies.

The current generation of ACTs consists of VERITAS [132], MAGIC [133], and H.E.S.S. [134], all of whom actively conduct dark matter searches. The next generation project is the Cherenkov Telescope Array (CTA) [135], which will extend the energy range at both the high and low ends by several orders of magnitude. The sensitivity will also enjoy an improvement of about an order of magnitude over existing ACTs [131].

1.4.2 Scattering and direct detection

Weakly interacting dark matter generally has a cross section for scattering with Standard Model particles. This is implied by crossing symmetry of the Feynman diagram describing annihilation. In 1985 the concept of direct detection was proposed by Goodman and Witten [136]. The idea is quite straightforward. Dark matter

particles that make up the Milky Way halo continually pass through the Earth. In a very low background detector one may observe the recoil of a nucleus after it scatters off a WIMP. The rate of scattering events in such an experiment is determined by the intrinsic WIMP properties (mass and scattering cross section) and by the number density and velocity distribution of WIMPs at the location of Earth. While the average dark matter density can be determined by the motions of relatively nearby stellar populations the ultra-local structure of the dark matter halo is unknown. Therefore, it may be the case that the Earth sits on a local underdensity or overdensity [e.g. 137, 138]. Unfortunately, unlike annihilation there is no analog to the relic abundance argument that provides a natural scattering cross section. Experiments must probe smaller and smaller cross sections with no floor.

Many groups currently compete to perform the most sensitive searches for dark matter scattering. As with indirect detection the key imperative is understanding the backgrounds in the detector. Radioactivity and cosmic rays will induce nuclear and electron recoils within the detector volume and it is vital to be able identify such events. The spectrum of dark matter induced nuclear recoils falls exponentially with energy. The field evolves by lowering the energy threshold and by increasing the number of target nuclei in the detectors.

The current state of affairs is quite interesting with several groups reporting excess events above the expected background. An early, novel approach taken by the DAMA/LIBRA experiment is to sacrifice background rejection by looking for an annual modulation of the recoil rate. This modulation is due to the Sun's motion relative to the Milky Way dark matter halo [139]. In June, the Earth is moving along with the Sun and in December it moves in the opposite direction. This induces a yearly oscillation in the WIMP scattering rate. The experiment has been running for thirteen years and has detected an annual modulation unambiguously [e.g. 140].

The challenge is whether or not there is another explanation for the modulation. Since the background rejection is minimal compared to other direct detection efforts there may be an unaccounted for background source.

Over subsequent years other experiments [e.g. XENON100 141] appear to have ruled out the parameter space (mass and scattering cross section) that corresponds to the DAMA/LIBRA WIMP. However, at the current time three other experiments report excess events. The CRESST-II dark matter search reports events inconsistent with a background-only hypothesis at 4σ [142]. Similarly, the CoGeNT collaboration has seen an excess of low-energy events [143]. The dark matter interpretations for both results appears to be ruled out by the XENON100 data, though not by a large margin. There is no shortage of explanations and dark matter models that explain the DAMA/LIBRA, CRESST-II, and CoGeNT events and the null XENEON100 result [e.g. 144].

Most recently, the CDMS II collaboration reported three excess events in their silicon detectors with an estimated background of 0.41 [145]. As with the other experiments this result is in tension with the XENON100 null result. Interestingly, all of the tentative detections indicate a low mass WIMP (mass around 10 GeV). It is important to note, however, that the excess events occur very near the lower energy thresholds of the detectors. The various tentative hints for dark matter will be confirmed or ruled out by the current and future generations of direct detection experiments. A small sample of notable upcoming efforts include LUX [146] and LZ [147], SuperCDMS [148], XENON1T [149], ArDM [150], and DEAP-3600 [151].

1.4.3 Capture and annihilation in solar system bodies

The ideas underlying direct and indirect detection can be combined in a creative way to use neutrino detectors to search for WIMPs. The phenomena requires both scattering and annihilation. If a WIMP passes through a solar system body (e.g. the Sun or Earth) it may scatter off a nucleus and lose enough energy that it becomes gravitationally bound to the body. Scatters on subsequent orbits will cause the WIMP to "sink" to the center of the body. Therefore, we generically expect the Sun, for example, to contain a reservoir of WIMPs at its center. These particles can then annihilate into Standard Model products. Of these products, neutrinos will freely escape and may be detected on Earth. This idea has led to searches for high-energy neutrinos from the direction of the Sun with the IceCube and AMANDA-II experiments [152]. In most dark matter models the capture rate is the limiting factor making the annihilation rate a function of the scattering cross section (and independent of the annihilation cross section). These neutrino experiments thus provide a complementary search to direct detection experiments.

1.4.4 Creation and colliders

Again using crossing symmetry of the Feynman diagram describing WIMP annihilation, we find that it may be possible to *create* WIMPs in high-energy particle physics experiments. Unfortunately, one can never be sure that a new particle discovered (e.g. at the LHC) is the *cosmic* dark matter. However, based on the new particle's properties one can calculate the relic abundance and see if it agrees with Ω_c. Additionally, the mass and other couplings would be vital in directing the progress of dedicated dark matter experiments, both direct and indirect.

Colliders perform searches for "missing momentum" where new particles are created but leave the detector unseen. The total momentum in the direction transverse to the beam is zero. Dark matter particles created in a collision may carry some momentum out of the detector leaving a net transverse momentum of the hadronic jets, photons, and other Standard Model particles. The current strongest collider constraints on such new particles come from the CMS [153] and ATLAS [154] at the LHC.

Perhaps the most important dark matter search that can be performed by colliders is the search for new physics beyond the Standard Model. For example, if the LHC collaborations discover evidence for supersymmetry they will immediately provide a dark matter candidate. This particle can then be targeted directly by other means.

1.5 Structure of this thesis

The following chapters contain the contents of the four papers [1–4] along with some unpublished supplementary material.

Chapters 2, 3, and 4 develop new statistical frameworks for analyzing data from multiple datasets. The techniques are applied to search for gamma-rays from dark matter annihilation in Milky Way dwarf spheroidal galaxies with data from the Fermi Gamma-ray Space Telescope. In Chapter 2 (based on Geringer-Sameth and Koushiappas [1]) a search for continuum emission is performed.

After the publication of this paper I generalized the methods to take full account of the information contained in the data, resulting in the individual event weighting

framework described in Chapter 3. This chapter is based on work for a forthcoming article. This event weighting framework is applied in Chapter 4 (based on Geringer-Sameth and Koushiappas [2]) to search for gamma-ray line emission from the same collection of dwarf galaxies.

I then turn the reader's attention to the subject of astrophysical backgrounds. Understanding these backgrounds is vital in any dark matter search (indeed in any gamma-ray observation). In Chapter 5 (based on Geringer-Sameth and Koushiappas [3]) I discuss a new method developed to identify the presence of moving sources in a diffuse background. The technique is not specific to Fermi but it will be useful in understanding a potentially important population contributing to the gamma-ray background.

Finally, in Chapter 6 (based on Geringer-Sameth and Koushiappas [4]) I explore a new technique to identify the presence of unresolved pulsars. This study grew out of the previous one: instead of focusing on correlations induced in the background by moving objects, I study correlations in the time domain caused by stationary sources.

Chapter Two

Search for continuum annihilation from dark matter

Introduction

Dwarf spheroidal galaxies are known to be excellent targets for the detection of annihilating dark matter [e.g. 155, 156]. In this chapter I present limits on the annihilation cross section of Weakly Interacting Massive Particles (WIMPs) based on the joint analysis of seven Milky Way dwarfs using a frequentist Neyman construction and Pass 7 data from the Fermi Gamma-ray Space Telescope. The analysis excludes generic WIMP candidates annihilating into $b\bar{b}$ with mass less than 40 GeV that reproduce the observed relic abundance. To within 95% systematic errors on the dark matter distribution within the dwarfs, the mass lower limit can be as low as 19 GeV or as high as 240 GeV. For annihilation into $\tau^+\tau^-$ these limits become 19 GeV, 13 GeV, and 80 GeV respectively.

It is well known that Milky Way dwarf galaxies are excellent targets to search for the signature of dark matter annihilation: they are dark matter dominated objects with no astrophysical backgrounds (no hot gas). Measurements of the velocity dispersion of stars in these systems allows the reconstruction of the gravitational potential and thus the density profile of the dark matter distribution [157–159].

In order to place constraints on the annihilation cross section, we must quantify how the value of $\langle \sigma_A v \rangle$ influences the number of γ-ray events detected with the Large Area Telescope (LAT) onboard the Fermi Gamma-ray Space Telescope (Fermi). There are two sources of detected photon events: those arising from dark matter matter annihilation (signal), and those produced by any other processes (background).

Expected signal

In the canonical picture, dark matter annihilates and gives rise to a γ-ray flux that is a function of two independent terms, one describing the dark matter particle physics and one involving the astrophysical properties of the dwarf galaxy. The expected number of signal events is

$$\mu(\Phi_{\rm PP}) \equiv (A_{\rm eff} T_{\rm obs}) \times \Phi_{\rm PP} \times J, \tag{2.1}$$

where $A_{\rm eff}$ is the effective area of the detector and $T_{\rm obs}$ is the observation time. The product $A_{\rm eff} T_{\rm obs}$ is called the exposure. The goal is to place limits on the quantity $\Phi_{\rm PP}$ which encompasses the particle physics. For self-conjugate particles it is defined as

$$\Phi_{\rm PP} \equiv \frac{\langle \sigma_A v \rangle}{8\pi M_\chi^2} \int_{E_{\rm th}}^{M_\chi} \sum_f B_f \frac{dN_f}{dE}\, dE, \tag{2.2}$$

where M_χ is the mass of the dark matter particle and $\langle \sigma_A v \rangle$ is its *total* velocity-averaged cross section for annihilation into standard model particles. The index f labels the possible annihilation channels and B_f is the branching ratio for each. For any channel, dN_f/dE is the final γ-ray spectrum. This quantity is integrated from a threshold energy $E_{\rm th}$ to the mass of the dark matter particle.

The quantity J contains information about the distribution of dark matter and is defined by

$$J \equiv \int_{\Delta\Omega(\psi)} \int_{\ell} [\rho(\ell, \psi)]^2 \, d\ell \; d\Omega(\psi).$$

Here, the square of the dark matter density is integrated along a line of sight in a direction ψ, and over solid angle $\Delta\Omega$.

Strategy for backgrounds

Typically, the background is derived through detailed modeling of possible contributions [160]. This was the approach taken in the Fermi Collaboration analysis [161–163, 118]. In this work I eschew such detailed modeling of the origin and spectral properties of the γ-ray background, and instead use the photon events in the region near each dwarf to empirically derive the background from all unresolved sources.

The fundamental assumption of the strategy is this: *whatever the processes are which give rise to the photon events nearby each dwarf, these same processes are also at work in the direction of the dwarf.* That is, the probability that background processes produce photons at the location of a dwarf can be determined by the empirical probability distribution found by sampling the observed counts in the surrounding region. The region surrounding each dwarf is a "sideband" used to determine the background. This approach requires zero free parameters and the entire analysis depends only on the value of $\Phi_{\rm PP}$.

Data selection

This analysis is uses data from the dwarf galaxies Boötes I, Draco, Fornax, Sculptor, Sextans, Ursa Minor, and Segue 1 because none are in a crowded field or near known γ-ray sources. We utilize the updated values of J presented in Ackermann *et al.* [118] (see also Charbonnier *et al.* [164]). The J values are derived based on modeling the velocity dispersion profiles of stars in each dwarf [157–159].

For this work, a Region of Interest (ROI) is a region of the sky with a radius of 0.5°

containing all `Pass 7` photons of `evclass=2` available publicly on the Fermi Science Support Center (FSSC) [165], in the Mission Elapsed Time interval of [239557417-334619159] seconds (August 4, 2008 15:43:36 UTC to August 9, 2011 21:45:57 UTC), and with energies [1-100] GeV (at these energies, the point spread function (PSF) is always less than 1°). For each ROI, we use the publicly available version `v9r23p1` of the `Fermi Science Tools` to extract photons (with `zmax=100`), select good time intervals (with all standard recommendations as stated on the FSSC), and compute the exposure ($A_{\rm eff}T_{\rm obs}$), which also takes into account the shape of the PSF within the ROI using the Instrument Response Function `P7SOURCE_V6`. Because the PSF is energy dependent, the exposure must be averaged with the annihilation energy spectrum. For a range of power-law indices of the spectrum the exposure within an ROI changes by at most 5%, making this a negligible effect in the cross section limits.

Empirical background distributions

We identify and mask all sources present within 10° of each dwarf using the 2nd Fermi Source Catalogue [166] (with a masking size of 0.8°). We calculate the probability of observing background events at the location of the dwarf by sampling 10^5 ROIs which are randomly selected within a distance of 10° from each dwarf, and counting the events in each. A window is rejected if it overlaps with a masked location or with the boundary. There are approximately $(10/0.5)^2 = 400$ independent ROIs for each dwarf. The background probability mass function (PMF) is given by the fraction of ROIs that contained a given number of counts (the PMF is not sensitive to increasing the mask size to 2°). This PMF is taken to be the probability distribution governing the number of background photons which contribute to the central ROI.

The accuracy of this strategy requires the total exposure not vary within a 10° radius around each dwarf and we find that it varies by at most $\sim 5\%$. If a γ-ray source is close to a dwarf it may contribute photons to the central ROI. These source photons are not accounted for in the empirical background PMF. Therefore, such photons are considered more likely to be from dark matter annihilation and will weaken the derived limit. In this sense, our analysis is conservative. The PMFs are well fit by Poisson distributions and do not contain features that would be expected from source contamination. Figure 2.1 shows the PMFs derived from the background sampling for each dwarf ROI. The red distribution is the empirical PMF found by sampling. The blue curve represents a best-fit Poisson distribution (i.e. a Poisson PMF having the same mean). The interpretation of the vertical and dashed black lines will be discussed below.

Statistical framework

In statistical inference one wants to generate confidence intervals for a model parameter μ based on observed data x. In a frequentist analysis the main task is to decide on an *algorithm* which constructs a region in μ-space for any value of x. This region is said to be an α-confidence interval if the algorithm has "coverage" α (see e.g. [167, 168]). An algorithm has coverage α if the chances of it "working" is α. That is, no matter what the true value of μ actually is, there is an α chance that the constructed confidence interval (region of μ-space) contains the true value.

One way to construct and visualize confidence intervals is by using the Neyman construction [168, 169]. The ingredients needed are the parameter space of possible μ values, a space of possible measurements x, and a likelihood function $\mathrm{P}(x|\mu)$, which gives the probability of observing x if μ were the true value of the parameter (μ and x

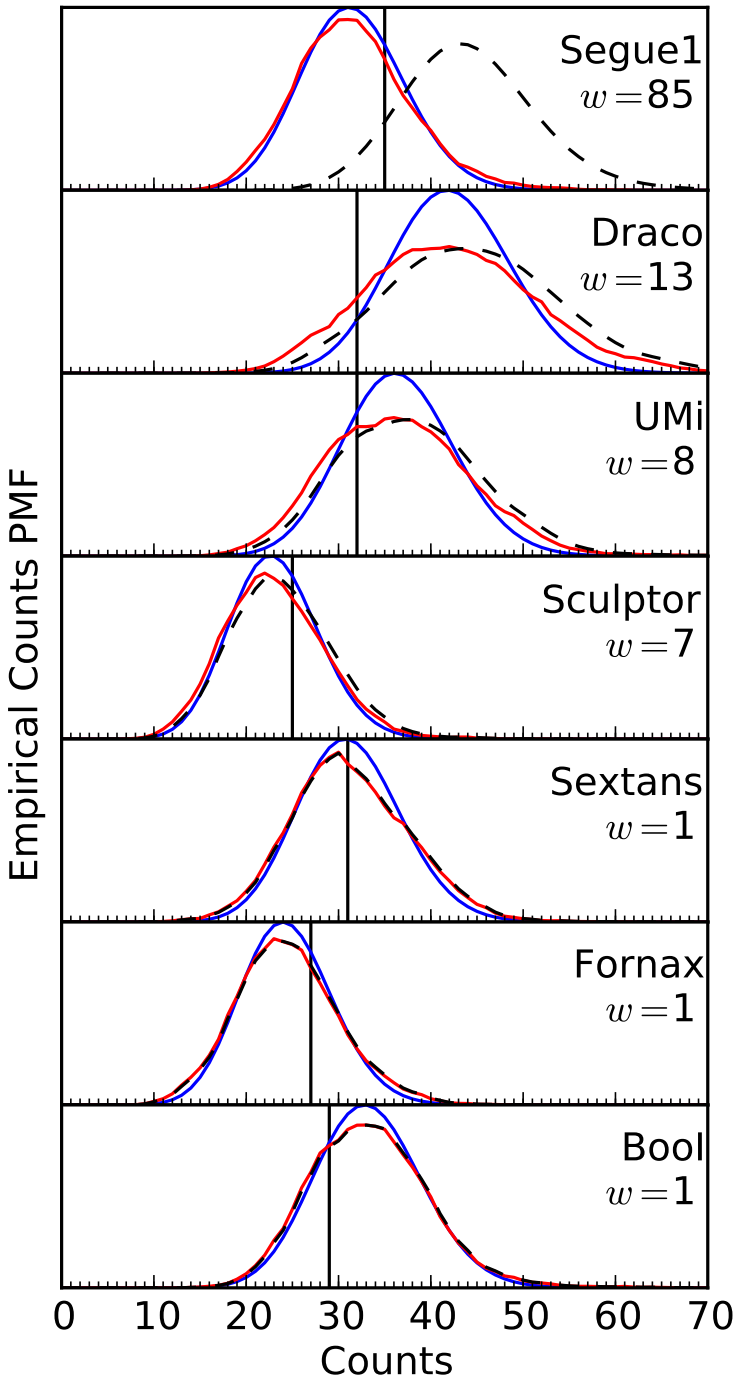

Figure 2.1: This figure illustrates the ingredients and data required to derive upper limits on the dark matter annihilation cross section. Each plot corresponds to a different dwarf galaxy. Sampling the counts in 0.5° regions surrounding each dwarf results in an empirical background probability mass function (PMF) shown in red. The blue curves are Poisson distributions having the same mean as the empirical background PMFs. The vertical line represents the number of counts observed in the ROI centered on the dwarf's location. The dashed curve is the convolution of the background PMF with the Poisson distribution representing the contribution from dark matter annihilation when $\Phi_{\rm PP} = 5.0 \times 10^{-30}\,{\rm cm}^3\,{\rm s}^{-1}\,{\rm GeV}^{-2}$ (the 95% upper limit on $\Phi_{\rm PP}$). This convolution is the probability distribution of the sum of signal and background. The label w is the weight given to each dwarf in the construction of Neyman confidence belts. It is given by the ratio of the strength of the expected dark matter signal to the mean expected background.

can both live in any number of dimensions). For each possible value of the parameter μ one selects a region $D(\mu)$ of the measurement space such that $\int_{D(\mu)} \mathrm{P}(x|\mu) = \alpha$ (i.e. the probability of measuring x to be in $D(\mu)$ is α if the true value of the parameter were μ). The regions $D(\mu)$ are called confidence belts. For an actual measurement x^*, these pre-selected belts can be used to generate an α-confidence region for μ: the confidence region is simply the collection of all the μ values whose belt $D(\mu)$ contains x^*. This algorithm for constructing a region in μ-space out of a measured value x^* provides the proper coverage: whatever the true value μ_t is, there is an α chance that x^* will lie in $D(\mu_t)$ (by construction) and therefore an α chance that the resulting confidence interval will contain μ_t.

Combining multiple observations

In this analysis, the observations consist of the number of counts N_i from the central ROI containing each dwarf ($i = 1, \ldots, 7$). These can be considered the components of a vector $\mathbf{N}$ living in a 7-dimensional integer lattice. To apply the Neyman construction we must choose a confidence belt in this 7-dimensional "N-space" for every possible value of Φ_{PP} such that the probability that $\mathbf{N}$ is measured to be in this belt is α.

There is complete freedom in the choice of belts (provided they have coverage α). Nevertheless, it is vital that the shape of the belts for each Φ_{PP} not be based on the measured data. This offense is known as "flip-flopping" [168]. It may result in confidence levels having lower coverage than stated. Here, the confidence belts are constructed *without prior knowledge* of the number of counts within the central ROI around each dwarf. Under the assumption that the empirically derived background PMFs, exposures, and J values are correct, the belts have the proper coverage.

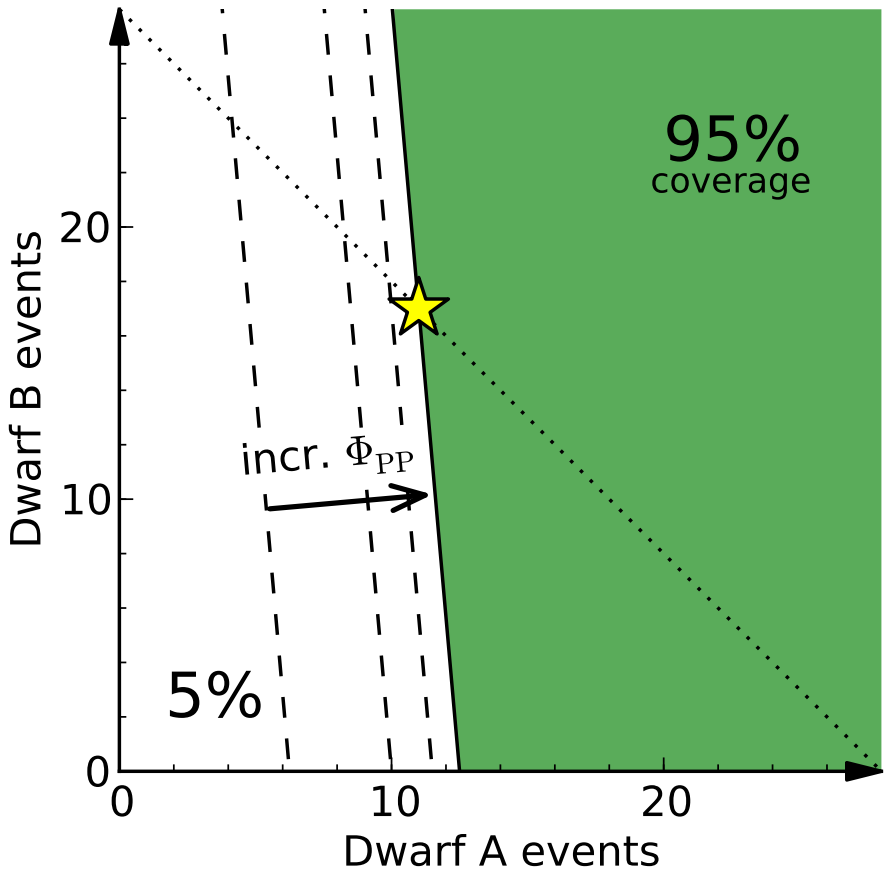

Figure 2.2: Illustration of the Neyman confidence belt construction used to generate upper limits on Φ_{PP}. Each axis represents the number of events that could be observed from a given dwarf (here, Dwarf A has a larger J value than Dwarf B does). The shaded area, bordered by the solid line, represents the confidence belt for a particular value of Φ_{PP}. The dashed lines are the borders of the confidence belts for different values of Φ_{PP}, with Φ_{PP} increasing from left to right. The borders are chosen to be normal to a vector of "sensitivities", which weights each dwarf according to the relative strength of its dark matter signal. Once a measurement is made (shown by the star) the confidence interval for Φ_{PP} contains all values of Φ_{PP} whose confidence belt contains the measured point. The dotted line shows the border for an alternative construction of the confidence belts which gives equal weight to each dwarf.

In order to derive an upper limit on $\Phi_{\rm PP}$, the N-space should be divided into two simple parts and the belt $D(\Phi_{\rm PP})$ should consist of the "large" **N** values (i.e. the region containing $N_i = \infty$). This is illustrated in Fig. 2.2 for an example joint analysis of two dwarfs. The simplest choice for the confidence belt boundaries are planes with normal vectors parallel to $(1, \ldots, 1)$, represented in Fig. 2.2 by the dotted line. A measured set of N_i is in such a confidence belt if the sum of the N_i is greater than some value. This is equivalent to "stacking" the events from each dwarf and then analyzing this single image. However, because the dwarfs are treated equally, photons from a dwarf with a small J value are considered as likely to have come from dark matter as are photons from a dwarf with large J. This is an inefficient choice for the confidence belts. Naively, one extra photon from Draco ($J \propto 0.63$) should raise the upper limit more than an extra photon from Boötes I ($J \propto 0.05$) because, a priori, a given photon from Boötes I is much more likely to be from background than a photon from Draco.

To overcome this obstacle we take advantage of the recent idea by Sutton [170] to use planes at angles other than 45° as boundaries of the confidence belts. Sutton suggests letting the normal vector to the planes be equal to a vector representing the "sensitivity" of each observation. We take the sensitivity (or weight) of each dwarf observation to be proportional to the ratio of the expected dark matter flux ($A_{\rm eff} T_{\rm obs}\, J$) to the mean expected empirical background flux. In contrast, giving every dwarf the same weight can weaken the limits by as much as 25% for this set of dwarfs.

Probability distributions

The number of photons received in the central ROI containing each dwarf is the sum of the number of photons from dark matter annihilation and the number produced by all background processes. The number of signal photons is governed by a Poisson distribution with mean $\mu(\Phi_{\rm PP})$ (Eq. 2.1). The number of background photons is described by the empirical background PMF. Therefore, the total number of events detected is distributed according to the convolution of these two probability distributions. An illustration of this convolution is represented as the black dashed curves in Fig. 2.1 for a particular choice of $\Phi_{\rm PP}$. The counts found for each dwarf are independent variables and so the joint probability of measuring $\mathbf{N}$ is given by the product of the individual PMFs.

Results

Using this statistical framework we derive a 95% upper bound of $\Phi_{\rm PP} = 5.0^{+4.3}_{-4.5} \times 10^{-30}\,{\rm cm}^3\,{\rm s}^{-1}\,{\rm GeV}^{-2}$. In order to translate the bound on $\Phi_{\rm PP}$ into a bound on $\langle\sigma_A v\rangle$ as a function of M_χ we need to assume a specific annihilation channel and its spectrum dN/dE. It is generally assumed that a WIMP annihilates primarily into hadrons (e.g. $b\bar{b}$) or heavy leptons (e.g. $\tau^+\tau^-$), which then decay by fairly well constrained channels into γ-rays. We compute dN/dE for these channels using DarkSUSY [171, 172].

Figure 2.3 shows the derived 95% upper bound on $\langle\sigma_A v\rangle$ as a function of WIMP mass. For annihilation into $b\bar{b}$ ($\tau^+\tau^-$) WIMP masses less than 40 GeV (19 GeV) are excluded using the central J values. The dominant source of systematic uncertainty comes from the poorly constrained J for each dwarf and is shown by the shaded

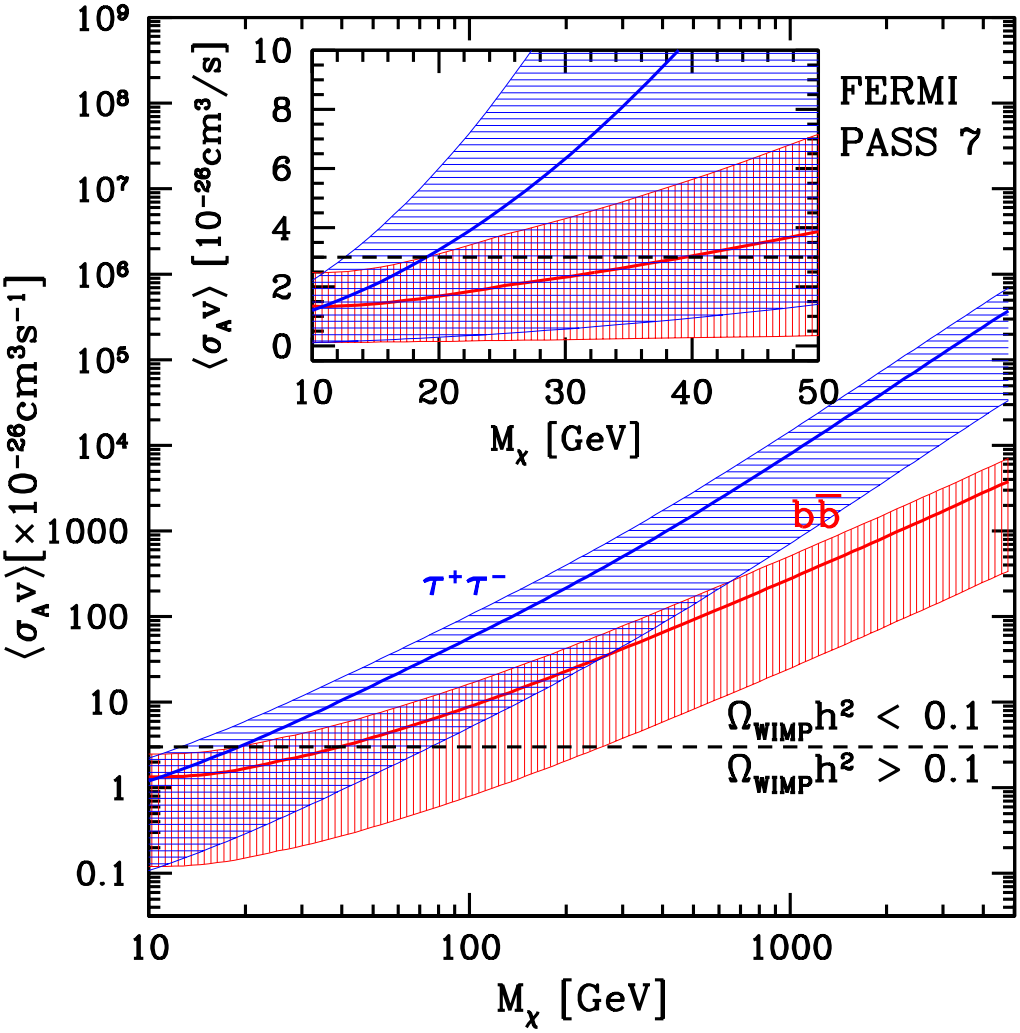

Figure 2.3: Derived 95% upper limit on $\langle\sigma_A v\rangle$ as a function of mass for dark matter annihilation into $b\bar{b}$ and $\tau^+\tau^-$. The shaded area reflects the 95-percentile of the systematic uncertainty in the dark matter distribution of the dwarfs. The canonical annihilation cross section for a thermal WIMP making up the total observed dark matter abundance is shown by the dashed line. The inset figure shows detail for lower masses.

regions in Fig. 2.3. The $\Phi_{\rm PP}$ limit is recalculated for each dwarf as its J varies between its upper and lower 95% error bar given in Ackermann *et al.* [118]. The results for each dwarf are then added in quadrature (this procedure gives a nearly identical region as that derived by scanning over the log-normal priors on J for each dwarf [157, 158, 118]). Figure 2.4 shows 95% cross section limits for WIMP annihilation into various Standard Model final states (quarks, leptons, gauge bosons).

Interpretation of systematic uncertainties

If we knew the exact J value of each dwarf, the width of the shaded regions in Fig. 2.3 would shrink to zero. However, due to the uncertainties in J, we have no knowledge of where this upper limit lies within the shaded region. Presenting the limit in this fashion separates the inherent statistical uncertainties (Poisson-distributed photon counts) from the systematic errors in the J's, which in principle could be known exactly (each dwarf has some particular, though unknown, dark matter distribution). At the present time there is no consensus on the dark matter distribution within Milky Way dwarfs. The systematic error bands should be thought of as an exploration of possible models for the dark matter distribution (for an alternative analysis of J values see Charbonnier *et al.* [164]). Nevertheless, for any model (set of J values) the construction presented here gives a rigorous 95% upper limit on $\Phi_{\rm PP}$.

For the most (least) conservative model the lower limit on the mass is 19 GeV (240 GeV) for $b\bar{b}$, while for $\tau^+\tau^-$ these limits are 13 GeV (80 GeV). Segue 1 is responsible for most of the uncertainty in the limit due to its high weight and uncertain dark matter content. However, if Segue 1 has a low J value, the statistical construction downgrades its weight relative to other dwarfs such as Draco and Ursa Minor. This

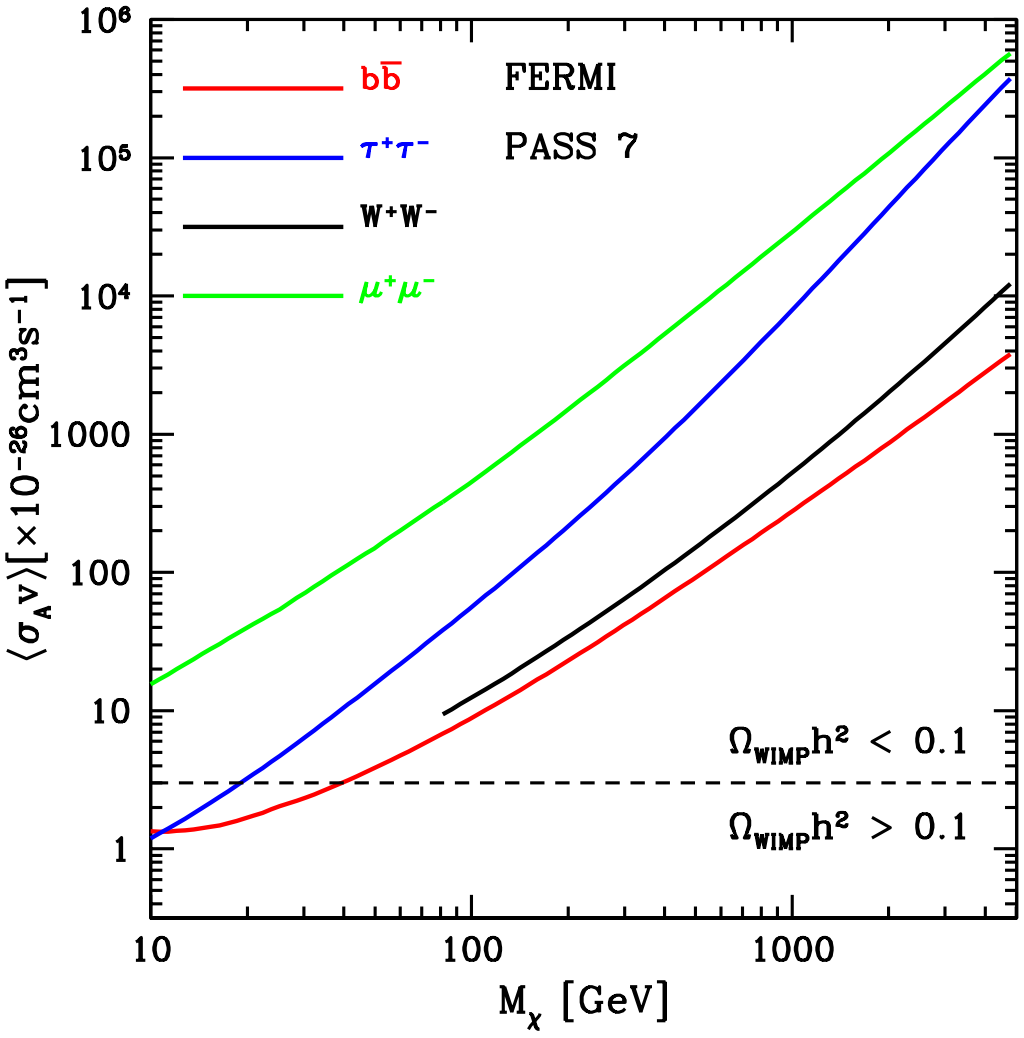

Figure 2.4: Dark matter annihilation cross section limits for various Standard Model final states. The best-fit J values are assumed to avoid the clutter of the systematic error bars. The curves are for annihilation into $b\bar{b}$ (red), $\tau^+\tau^-$ (blue), W^+W^- (black), and $\mu^+\mu^-$ (green). Annihilation into other quark final states gives nearly identical results as for $b\bar{b}$.

is one of the powerful features of the statistical framework.

Sensitivity to background PMFs

The strength of the analysis relies on the validity of the assumption that the background at the location of each dwarf is adequately described by the empirical PMF. In general, if the assumed background PMF is skewed toward higher numbers of counts the upper limit on $\Phi_{\rm PP}$ becomes stronger. This is because more of the observed counts can be attributed to background and therefore fewer to dark matter annihilation. We can quantify the effect of an error in the empirical PMF by considering the radical case where we are certain there is no background at all. This is a false assumption, but is one which will produce the most conservative limit on $\Phi_{\rm PP}$. If we force the background PMFs to be equal to 1 when the number of counts is 0 and equal to 0 otherwise, the 95% limit on $\Phi_{\rm PP}$ increases by a factor of 4.4 over the actual limit. This represents the case where every photon received from a dwarf is believed to be due to dark matter annihilation. We interpret this as a test of the robustness of the method, not as any sort of actual confidence limit. We can also test our conclusions against less violent changes to the background PMF. For each dwarf we replace the background PMF with a Poisson distribution having the same mean, and find that the limit on $\Phi_{\rm PP}$ decreases by 7%. These Poisson PMFs are shown as the blue curves in Fig. 2.1.

Discussion

What is the significance of this new bound on $\langle \sigma_A v \rangle$? It signals, perhaps, that we are imminently approaching an epoch of discovery. Three decades of experimental

design have given rise to many detectors sensitive enough to probe a very generic class of dark matter candidates. The prime motivation for WIMP dark matter is the coincidence that a weak-scale annihilation cross section naturally reproduces the observed relic abundance. Unlike the scattering cross section probed in direct detection experiments, cosmology gives a lower limit for the annihilation cross section. The parameter space in which a WIMP can hide is therefore bounded at both ends. This work, together with the Fermi-LAT collaboration result [162, 118, 163], pushes the contact point between the upper and lower bounds on $\langle \sigma_A v \rangle$ to increasing WIMP masses, suggesting that observations have become powerful enough to either discover or rule out the best-motivated and most sought-after dark matter candidates.

Chapter Three

Development of the event weighting framework

3.1 Hypothesis testing and confidence intervals

In the frequentist paradigm we interrogate the data through the framework of hypothesis testing. For example, to find out whether observations of a dwarf show evidence for dark matter annihilation we may start by testing the hypothesis H_b : the observed data D were generated from background processes only. We find a way to calculate the probability $\mathrm{P}(D|H_b)$ of observing D if H_b were true. If this probability is small, say $\mathrm{P}(D|H_b) = 0.01$, the hypothesis is "rejected at 99% significance" — i.e. it is very unlikely to have measured the data we did if there were no dark matter annihilation.

Confidence intervals on dark matter model parameters can be generated by performing an ensemble of hypothesis tests. For simplicity, imagine that dark matter annihilation is governed by two parameters, the particle mass M and the (velocity-averaged) annihilation cross section $\langle\sigma v\rangle$. For every possible pair of values of these parameters we perform the hypothesis test "dark matter has mass M and annihilation cross section $\langle\sigma v\rangle$." We classify a point in parameter space by whether its associated hypothesis is rejected at a given level α (e.g. $\alpha = 0.05$ for a 95% confidence region). That is, we divide the parameter space into allowed regions where $\mathrm{P}(D|M, \langle\sigma v\rangle) > \alpha$ and excluded regions where $\mathrm{P}(D|M, \langle\sigma v\rangle) < \alpha$. The allowed region constitutes an α-level confidence region for mass and cross section. The interpretation of the two regions is straightforward (e.g. for $\alpha = 0.05$): whatever the true values of M and $\langle\sigma v\rangle$ are, there is only a 5% chance that the hypothesis associated with those true values will be rejected. Equivalently, there is a 95% chance that the constructed confidence region contains the true parameters.

3.1.1 Test statistics

The implementation of this scheme is made possible by the construction of a test statistic T, a single number that is a function of the data we measure. The test statistic is a random variable and when we make a measurement we sample this variable. For a given a hypothesis, a probability distribution function (PDF) governs the measurement of T. Before making the measurement, we decide on a critical region $\mathcal{C}$[1] of T-space such that $\mathrm{P}(T \in \mathcal{C}|H) = \alpha$. Should T be measured to lie in the critical region we reject the hypothesis H at level α.

The use of a test statistic allows us to make precise the "probability of observing the data given a hypothesis". For this purpose it is useful to choose a test statistic that reflects how "signal-like" or "background-like" the data are, with larger values of T indicating the presence of a signal (e.g. dark matter annihilation). For instance, when testing the hypothesis H_b that there is no dark matter annihilation we might choose a special value T^* to define the critical region as $\mathcal{C} : T > T^*$, where $\mathrm{P}(T > T^*|H_b) = 0.01$ (i.e. $\alpha = 0.01$). The interpretation of $\mathcal{C}$ is that there is only a 1% chance of the data being so "signal-like" if there were no dark matter annihilation. If the measured T is larger than T^* the hypothesis H_b is rejected at 99% significance.

Constraints on the the particle physics parameters should take the form of upper limits on the annihilation cross section. Upper limits on $\langle\sigma v\rangle$ are generated by choosing the critical region to be $\mathcal{C} : T < T^*$, where $\mathrm{P}(T < T^*|M, \langle\sigma v\rangle) = \alpha$. We will reject the hypothesis that dark matter has a particular mass M and cross section $\langle\sigma v\rangle$ if T is found to be smaller than T^* (i.e. the measurement is too background-like). This choice of critical region for T (i.e. $T < T^*$ as opposed to $T > T^*$) generates upper limits on the cross section: for large cross sections T^* will increase

[1] $\mathcal{C}$ is equivalent to the $D(\mu)$ of Chaper 2.

since the data is likely to be more "signal-like". For sufficiently large cross sections the associated hypothesis will be always be rejected, leading to upper limits on $\langle \sigma v \rangle$.

3.2 General form of the test statistic

In principle, T can be an arbitrary function of the data. However, some functions are better than others in a well-defined sense. Here I detail the construction of an optimal test statistic.

The gamma-ray data is in the form of a list of discrete detector events. We wish to jointly analyze the gamma-ray signal from multiple targets simultaneously and to take full advantage of the information contained in the data. Each event is assigned a numerical weight $w(Q)$ based on its properties Q and the hypothesis we are testing. We use a test statistic that is simply the sum of the weights of all the events in the entire data set

$$T = \sum_{i=1}^{N} w(Q_i), \tag{3.1}$$

where i runs over all detected events. The total number of events N and the collection $\{Q_i\}$ are random variables.

For the dataset we are working with the dark matter physics is encoded in three properties of each detected event: which dwarf ν field the event came from, the reconstructed energy E of the photon, and the reconstructed direction θ of the photon (i.e. the angular separation between the event and the location of the dwarf galaxy). Therefore, in our study $Q = (\nu, E, \theta)$ is the set of these three variables, the first being discrete and the second two continuous.

This general form for the test statistic is capable of reproducing many other analyses by making particular choices for the weight function. For example, a standard event counting analysis can be performed by setting $w(Q) = 1$ for events in some energy range and within some angular separation of one of the dwarfs, and $w(Q) = 0$ for all other events. In this case the test statistic T just counts the number of events detected. As a second example, the analysis performed in [1] (Chapter 2) is recovered by having $w(Q)$ be a function only of which dwarf field the event came from (and not of the energy or angular separation of the event). The test statistic then becomes a simple weighted sum of counts observed from each dwarf.

3.3 Designing the weight function

Given this general form of test statistic the important work lies in designing the weight function. In this section I show that there is a statistically most powerful weight function.

Recall that α denotes the probability of rejecting the hypothesis when the hypothesis is true. The power of a statistical test is the probability of rejecting the hypothesis when the hypothesis is false (i.e. when it *ought* to be rejected). Therefore, we seek a test statistic that maximizes the power for a given α. The power of a test is an ambiguous concept because it depends on what the truth actually is. That is, a test that is powerful at rejecting H_0 when H_1 is true may not be powerful at rejecting H_0 when H_2 is true [167, §21.16-18]. We therefore restrict our task to finding the test statistic that maximizes the power of rejecting H_0 for a suitable single alternative hypothesis H_1.

As discussed above, for constructing upper limits on dark matter particle parameters we test hypotheses of the form "dark matter has mass M and annihilation cross section $\langle\sigma v\rangle$". For these cases we take the alternative hypothesis to be H_b, the background-only hypothesis of no dark matter annihilation. This gives the most constraining upper limits on $\langle\sigma v\rangle$ if dark matter has an annihilation cross section too low for the instrument to detect. When performing a search for annihilation we see if we can reject the hypothesis H_b. In this case the test statistic is chosen to maximize the power versus an alternative hypothesis that dark matter has a particular mass and an infinitesimal annihilation cross section. That is, the test is designed to be sensitive to weak signals. The choice of particle parameters besides the cross section will be dealt with using a "trials factor". We may test H_b against several different masses and branching ratios.

Below we present two ways to construct a most-powerful weight function $w(Q)$. The first is heuristic and more intuitive, the second more rigorous. Both yield similar conclusions.

It will be useful to write the test statistic (3.1) in an alternate form by introducing a new set of random variables that are easier to work with. The random variable Z_Q is the number of events that were detected with properties in an infinitesimal bin centered on Q. Using the set $Q = (\nu, E, \theta)$ described above, Z_Q is the number of events from dwarf ν that have energy between E and $E + dE$ and were detected between θ and $\theta + d\theta$ from the location of the dwarf. The size of these bins are infinitesimal so that Z_Q is almost always 0 and is occasionally 1. Making a measurement is equivalent to measuring the infinite collection $D = \{Z_Q\}$ (for a finite set of Q, Z_Q will be 1; for the rest, Z_Q will be 0). The weight of a photon with properties

Q is denoted w_Q. The test statistic can be written in terms of the variables Z_Q as

$$T = \sum_Q w_Q Z_Q, \tag{3.2}$$

where the sum is over all possible properties of a detected event. In our case the notation $\sum_Q$ is shorthand for $\sum_\nu \int_E \int_\theta$. The test statistic is determined by the infinite collection of random variables $\{Z_Q\}$ and the infinite collection of numerical weights $\{w_Q\}$. Defining a weight function $w(Q)$ is equivalent to fixing values for each of the $\{w_Q\}$.

In our situation it is useful to write each Z_Q as the sum $Z_Q = X_Q + Y_Q$, where X_Q is the number of events detected with properties Q that originated from dark matter annihilations in a dwarf galaxy (signal events) and Y_Q is the number of detected events originating from all other sources (background events). The collection of $\{X_Q\}$ are independent random variables and are also independent of all of the $\{Y_Q\}$. The probability distribution for X_Q is

$$\mathrm{P}(X_Q) = \begin{cases} 1 - s_Q & \text{for } X_Q = 0, \\ s_Q & \text{for } X_Q = 1, \end{cases} \tag{3.3}$$

where s_Q is the (infinitesimal) expected number of detected dark matter events having properties Q. The probability distribution describing Y_Q may not be as simple because different Y_Q may be correlated (e.g. if the background has a contribution from unresolved sources). In deriving an optimal choice of weights we will make the assumption that the Y_Q are independent and each is described by

$$\mathrm{P}(Y_Q) = \begin{cases} 1 - b_Q & \text{for } Y_Q = 0, \\ b_Q & \text{for } Y_Q = 1, \end{cases} \tag{3.4}$$

with b_Q the expected number of background events having properties Q. Because of this assumption the choice of weights may not be strictly the most powerful but we expect the deviations from optimality to be minimal. We note that the calculation of the PDF of T does not use this simplifying assumption and correctly includes the effects of any correlations present in the background.

3.3.1 Signal-to-noise method

To construct confidence regions we test the hypothesis that dark matter is present and has a particular set of particle physics parameters. This test is to be most powerful against the alternative that the data is generated by background processes only. The two hypotheses are referred to as H_{s+b} and H_b.

The problem of maximizing the power of H_{s+b} versus H_b can be visualized as trying to maximally separate the PDFs of T for the two hypotheses. The specific shapes of the PDFs are controlled by the weight function $w(Q)$. An approximate way of describing the PDFs is by their means and standard deviations: μ_{s+b}, μ_b, σ_{s+b}, σ_b. The "separation" of the two PDFs can be quantified by constructing a signal-to-noise ratio:

$$\text{SNR} = \frac{\mu_{s+b} - \mu_b}{\sigma_b} \tag{3.5}$$

We will write the quantities in the above equation in terms of the weights w_Q and find the collection of w_Q that maximizes the signal-to-noise ratio. Using (3.2), (3.3), (3.4), the independence of the $\{X_Q\}$ and $\{Y_Q\}$, and the fact that all s_Q=0 if

H_b is true, it is straightforward to show that

$$\mu_b \equiv \mathrm{E}\left[T|H_b\right] = \sum_Q w_Q b_Q,$$
$$\mu_{s+b} \equiv \mathrm{E}\left[T|H_{s+b}\right] = \sum_Q w_Q (s_Q + b_Q),$$
$$\sigma_b^2 \equiv \mathrm{Var}\left[T|H_b\right] = \sum_Q w_Q^2 b_Q,$$

where $\mathrm{E}[T|H]$ and $\mathrm{Var}[T|H]$ are the mean and variance of T assuming the hypothesis H is true. Inserting these results into (3.5) yields

$$\mathrm{SNR} = \frac{\sum w_Q s_Q}{\sqrt{\sum w_Q^2 b_Q}}.$$

We find the weights that maximize this quantity by differentiating it with respect to an arbitrary weight w_R and setting the derivative to zero. This leads to the following condition that holds for each R:

$$w_R \frac{b_R}{s_R} = \frac{\sum w_Q^2 b_Q}{\sum w_Q s_Q}.$$

The solution to this set of equations is

$$w_Q = \frac{s_Q}{b_Q}. \tag{3.6}$$

Had we used σ_{s+b} instead of σ_b in the definition of SNR (3.5) the resulting optimal weights would be

$$w_Q = \frac{s_Q}{s_Q + b_Q}. \tag{3.7}$$

Note that even though s_Q and b_Q are each infinitesimal their ratio is finite.

This argument tells us that each event should be given a weight determined by

the ratio of the expected signal to the expected background for events of that type. This makes intuitive sense: events which are more likely to be signal are given a larger weight than those likely to be due to background processes. One upshot of this weighting applied to the dark matter search is that events which have an energy larger than the mass of the dark matter particle we are considering in H_{s+b} will be ignored (given a weight of 0) because they must be due to background.

3.3.2 Likelihood ratio method

An alternative derivation of the optimal weights is based on famous statistical theorem. The Neyman-Pearson lemma [173, 167, §21.10] states that the most powerful test between two simple hypotheses such as H_{s+b} and H_b can be performed by using a likelihood ratio as the test static. The likelihood $\mathrm{P}(D|H)$ is the probability of observing the data D if the hypothesis H were true. In our case, to test the hypothesis H_{s+b} against the alternative H_b we would calculate the likelihood ratio

$$\Lambda = \frac{\mathrm{P}(D|H_{s+b})}{\mathrm{P}(D|H_b)} \tag{3.8}$$

and reject the hypothesis H_{s+b} if Λ is found to be smaller than a critical value Λ^*. This critical value is determined by α, the desired level of the test: $\mathrm{P}(\Lambda < \Lambda^*|H_{s+b}) = \alpha$.

In the case under consideration (independent $\{X_Q\}$ and $\{Y_Q\}$) it is easy to write down the likelihoods under the two hypotheses. Let $\{Q_i \mid i = 1 \ldots N\}$ denote the properties Q of the N observed events. That is, Z_Q was found to be 0 for all but the finite set $\{Q_i\}$ for which $Z_Q = 1$. The probability of measuring this collection of Z_Q

under the two hypotheses is

$$\begin{aligned} \mathrm{P}(\{Z_Q\}|H_b) &= \prod_Q (1-b_Q) \prod_i b_{Q_i}, \\ \mathrm{P}(\{Z_Q\}|H_{s+b}) &= \prod_Q (1-s_Q-b_Q) \prod_i (s_{Q_i}+b_{Q_i}). \end{aligned} \tag{3.9}$$

In these equations, the first product contains the infinite set of all Q except for the finite set $\{Q_i\}$ while the second product only contains N factors corresponding to the $\{Q_i\}$. In the limit that the binning of event space becomes infinitesimal, b_Q and s_Q approach zero and it makes no difference whether the first product omits a finite collection of Q. One can also show that in this limit these infinite products converge exactly to exponentials:

$$\begin{aligned} \prod_Q (1-b_Q) &\to \exp\left(-\sum_Q b_Q\right), \\ \prod_Q (1-s_Q-b_Q) &\to \exp\left(-\sum_Q (s_Q+b_Q)\right). \end{aligned} \tag{3.10}$$

Using (3.9) and (3.10), the likelihood ratio (3.8) is given by

$$\Lambda = \exp\left(-\sum_Q s_Q\right) \prod_i \left(1+\frac{s_{Q_i}}{b_{Q_i}}\right).$$

It makes no difference if we use $\log\Lambda$ as the test statistic since the logarithm is a monotonic function:

$$\log\Lambda = -\sum_Q s_Q + \sum_{i=1}^{N} \log\left(1+\frac{s_{Q_i}}{b_{Q_i}}\right).$$

The first term is a constant that does not depend on the data so it has a trivial effect on the probability distribution governing the test statistic. Ignoring this term leaves

us with a test statistic that is most powerful at distinguishing H_{s+b} from H_b:

$$T = \sum_{i=1}^{N} \log\left(1 + \frac{s_{Q_i}}{b_{Q_i}}\right), \tag{3.11}$$

where H_{s+b} should be rejected if T is below T^*, specified by the condition $\mathrm{P}(T < T^*|H_{s+b}) = \alpha$. Comparing (3.11) with (3.1) we see that if we set the weight function to be

$$w(Q) = \log\left(1 + \frac{s_Q}{b_Q}\right) \tag{3.12}$$

the test statistic (3.1) is equivalent to a likelihood ratio test statistic. Therefore, using the weight function (3.12) gives rise to the most powerful test statistic. Note that if we are testing the hypothesis H_b and want the test to be optimally sensitive to H_{s+b} we can use precisely the same weight function (3.12). The only difference is that H_b will be rejected when T is larger than T^*, as determined by $\mathrm{P}(T > T^*|H_b) = \alpha$.

It is interesting to observe that the log-weighting in (3.12) is in some sense a compromise between the two weighting schemes derived in (3.6) and (3.7). Considered as functions of $x \equiv s_Q/b_Q$ we see that $x/(1+x) \leq \log(1+x) \leq x$ for all physical values of x (non-negative s_Q and b_Q). When considering a very weak signal ($s_Q \ll b_Q$) all three become equivalent to (3.6). In this case the test statistic is actually independent of the annihilation cross section since $\langle\sigma v\rangle$ enters as a multiplicative factor in s_Q (e.g. Eqs. 4.6 and 2.1) and two test statistics are equivalent if they differ by a constant factor. This implies that when searching for the presence of a small signal (i.e. testing the background-only hypothesis) the test statistic is optimal against all alternative hypotheses H_{s+b} with small cross section (keeping other model parameters fixed).

3.4 Probability distribution of the test statistic

Here we derive the PDF of the test statistic defined by (3.1) for any choice of weight function $w(Q)$. First note that T is the sum of two terms

$$T = T_s + T_b, \tag{3.13}$$

where T_s is the total weight of all detected photons originating from dark matter annihilation in dwarfs (signal) and T_b is the total weight of all other detected events (background). The signal events and background events are statistically independent of one another. Therefore, the the PDF of T is the convolution of the PDFs of T_s and T_b. The PDF of T_b is found by sampling the events from the regions surrounding each dwarf galaxy as described in Chapters 2 and 4.

To find the PDF of T_s note that the number of detected signal events N_s is a random variable distributed according to a Poisson distribution. The weights of the detected signal events $\{w(Q_i) \mid i = 1 \dots N_s\}$ are independent and identically distributed random variables. Therefore, the random variable T_s is the sum of independent variables where the number of terms in the sum is itself a Poisson random variable. Such a quantity is distributed according to a compound Poisson distribution (e.g. [174, 175]).

This compound Poisson distribution is determined by two quantities. The first is the mean μ of the Poisson distribution determining the total number of signal events observed. In terms of the definitions given in (3.3) we have $\mu = \sum_Q s_Q$. The second input is the single-event weight distribution $f(w)$. Specifically, $f(w)dw$ is the probability that a detected signal event has properties Q that cause it to be given a weight $w(Q)$ between w and $w + dw$. It is completely determined from the

collection s_Q once the weight function has been chosen. To compute $f(w)$ we divide the Q-space into small tiles (i.e. for each dwarf we divide the E-θ plane into small bins) and find the weight w_Q and the (unnormalized) probability s_Q in each bin. The weights w_Q are binned into a histogram where each w_Q adds a probability of s_Q to the histogram. This procedure can be made arbitrarily accurate by dividing the Q-space into small enough bins. In practice, we chose the bins to be small enough so that our results do not depend on the binning.

The Fourier transform $\phi_T(k)$ of the PDF of a compound Poisson distribution takes a simple form [175]:

$$\phi_T(k) = \exp\left[\mu\left(\phi_W(k) - 1\right)\right], \tag{3.14}$$

where $\phi_W(k)$ is the Fourier transform of the single-event weight distribution $f(w)$. Numerically, this function can computed quickly using fast fourier transforms (FFTs). Working in Fourier-space also makes convolutions efficient — one can simply multiply the Fourier transforms. After this processing an inverse FFT is used to produce the PDF.

3.5 Carrying out the tests

We are concerned with two related hypothesis tests. First, we can perform a search for dark matter annihilation by asking whether the data is consistent with the hypothesis H_b that there is no annihilation in the dwarf galaxies against the alternative hypotheses H_{s+b} that dark matter has particular properties. If H_b cannot be rejected we construct limits by testing the ensemble of hypotheses H_{s+b} to find which dark

matter properties are ruled out (i.e. which of the H_{s+b} are rejected at, say, 95% confidence). In both cases the optimal test statistic is determined by the two hypotheses under consideration.

For the annihilation search the weight function is (3.12), which reduces to (3.6) for an infinitesimal signal amplitude (e.g. small annihilation cross section). The probability distribution of the test statistic is calculated. In this case the PDF of T receives no contribution from dark matter annihilation: $T = T_b$. Then the observed value of the test statistic $T_{\rm obs}$ is measured and the significance calculated by finding $\mathrm{P}(T > T_{\rm obs} \mid H_b)$. If this probability is small the background-only hypothesis is rejected.

To construct upper limits we perform a hypothesis test for every possible annihilation cross section. We find the value of the cross section $\langle\sigma v\rangle$ such that $\mathrm{P}(T < T_{\rm obs} \mid \langle\sigma v\rangle) = \alpha$. Hypotheses with a larger $\langle\sigma v\rangle$ will be rejected and those with smaller $\langle\sigma v\rangle$ are not rejected. Therefore this value of the cross section represents an α-upper limit.

3.6 Expected results

A very powerful benefit of being able to find the PDF of T for any hypothesis is the straightforward computation of expected results. Computing the PDF of the test statistic is equivalent to simulating the results of the observations under a particular hypothesis. Instead of simulating millions of realizations of the raw data (e.g. collections of photon and background events) we can exactly compute the probability distribution of the test statistic that would have been derived form the

raw data. Therefore, without "uncovering" the actual photon data we can predict how our methods are likely (in a precise sense) to perform.

For example, suppose we wish to predict how strong our upper limits will be if there was no dark matter annihilation in the dwarf galaxies. We can perform the usual hypothesis test of H_{s+b}. However, instead of using the actual observed data to compute T_{obs} we can *assume* that the observed test statistic will just be sampled from the background-only PDF of T. That is, we compute $\mathrm{P}(T \mid H_b)$ and sample T_{obs} from this distribution. A central estimate of the expected limit can be found by taking T_{obs} to be the median of the background-only distribution. To find the statistical uncertainty in the limit we can compute limits when T_{obs} is at, say, the 25th and 75th percentile of the background distribution to find where the upper limit is likely to be found.

Likewise, we can simulate the results of a search for dark matter annihilation by sampling T_{obs} from the PDF of T including the component T_s due to dark matter annihilation. When searching for a signal we test the background-only hypothesis H_b multiple times against signal hypotheses H_{s+b} with different dark matter properties for each. It is important to determine how "finely-grained" the H_{s+b} are. For example, for how many trial dark matter masses should the search be performed for? Should the search be performed for different annihilation channels? Or will a dark matter signal be detected regardless of the specific alternative hypothesis we are testing against?

There are several additional benefits to being able to compute the distribution of expected results. In frequentist statistical analysis it is vital that the choice of test statistics and critical regions not be influenced by the observed data. One issue that has not been addressed is the selection of what events to consider for the analysis.

In our case this entails selecting which dwarf galaxies to consider. We also need to decide on the energy range of the events we consider and the maximum angular separation from a dwarf an event can have. These choices define our Regions of Interest (ROIs) for each dwarf galaxy. We can use the expected limits formalism to find out how different choices of ROI parameters will affect the annihilation limits.

Finally, we can use this formalism to make predictions for future experiments: with more observation time, different detector properties, and different targets, how strong are the dark matter limits expected to be?

Chapter Four

Search for gamma-ray lines

Introduction

The search for dark matter annihilation directly into a photon final state is extremely important because the line emission occurs at an energy that corresponds to the mass of the dark matter particle (or thereabouts if the second particle is a heavy neutral particle) [176–180, 69, 181]. In addition, line emission is free of background contamination as no known astrophysical process can result in line emission at the energies of interest (a few GeV up to tens of TeV).

Recently there have been claims of the presence of a gamma-ray line at $E_\gamma = 130$ GeV [182–184]. These studies, based on 3.5 years of data from Fermi, find a line emission signature from the direction of the Galactic center. The interpretation of these results as dark matter annihilating directly to a photon final state implies a cross section of $\langle \sigma v \rangle \approx [10^{-27} - 10^{-26}]$ cm^3/s. It is important to emphasize that this annihilation cross section is much larger than what one would expect from second order diagrams that lead to a two-photon final state (or a single photon and a Z gauge boson or h — for a summary see e.g., [69]). Several dark matter interpretations for the alleged line feature have been offered [e.g. 183, 185–191] while other work raises doubts about the statistical significance of the line and its interpretation as dark matter [192, 193]. A recent search by the Fermi collaboration did not detect the presence of line emission in the Galactic halo (including the Galactic center) [194].

The Galactic center is clearly a place of interest when it comes to dark matter annihilation because of its large expected dark matter density [195]. As the annihilation rate is proportional to the square of the number density of dark matter particles, its high density, coupled with its proximity to Earth, makes the Galactic center an attractive target for the search for an annihilation signal [e.g. 113].

In this chapter I discuss an independent search for dark matter annihilation to a photon final state in Milky Way dwarf galaxies using data from the Fermi Gamma-ray Space Telescope (Fermi). By virtue of their pristine dark matter environment (absence of high-energy baryonic processes) and high concentration of dark matter, dwarf galaxies have been used to place the strongest bounds to-date on the s-wave annihilation cross section of dark matter [1, 118]. Given the paucity of background contamination along the lines of sight to the dwarf galaxies, it is natural to consider what limits the dwarfs may place on the annihilation cross section of dark matter into photon final states.

Statistical framework

The approach we take is a generalization of Geringer-Sameth and Koushiappas [1] described in Chapter 2. We perform a line search by testing, at each line energy E_γ, the null hypothesis that the observed data was generated by background processes. Each hypothesis test is based on a test statistic T, which can be an arbitrary function of the data; however, it is vital that the choice of test statistic be made without reference to the data actually measured in the direction of the dwarf galaxies. A detailed development of the statistical framework is found in Chapter 3.

We choose a simple form for the test statistic that combines the photon information from each of the dwarfs. Each photon i within a Region of Interest (ROI) of size 1° is assigned a weight w based on which dwarf ν it came from, its energy E, and its angular separation θ from location of the dwarf. We denote this set of properties as $Q_i : \{\nu, E, \theta\}$. The test statistic T is the sum of the weights of the photons detected

within the ROIs centered on each dwarf:

$$T = \sum_{\nu} T_{\nu} \tag{4.1}$$

where the single-dwarf test statistic T_ν is

$$T_{\nu} = \sum_{i=1}^{N_\nu} w(Q_i). \tag{4.2}$$

Here, N_ν is the number of photons detected within the ROI centered on dwarf ν. The weights $w(Q_i)$ and the total number of photons N_ν from each dwarf are random variables[1].

To calculate the statistics of T it is useful to divide the parameter space of energy and angular separation (for each dwarf) into infinitesimal bins, each labeled by $Q = \{\nu, E, \theta\}$. The number of photons detected in each bin is a random variable Z_Q. This total number of photons is the sum of two random variables: the number of photons from dark matter annihilation X_Q and the number originating from background processes Y_Q (i.e., $Z_Q = X_Q + Y_Q$). In Eq. 3.6 I showed that the weight function that maximizes an expected signal to noise ratio for a line emission search (in the weak-signal regime) is

$$w(Q) = \frac{s_Q}{b_Q}, \tag{4.3}$$

where s_Q and b_Q are the expected number of signal and background counts in the parameter space bin Q.

Note that while s_Q and b_Q are infinitesimal quantities (being proportional to

[1] In Chapter 2, describing the analysis of the continuum gamma-ray emission from a combination of dwarf galaxies [1], the weight of each photon was determined only by which dwarf it came from. The test statistic was therefore the weighted sum of the total number of photons collected from each dwarf.

the size of the infinitesimal Q bin) their ratio is finite. In addition, s_Q depends on signal characteristics in such a way that the expected signal in any infinitesimal Q bin is directly proportional to the annihilation cross section. Therefore, changing the annihilation cross section will simply scale the test statistic by a constant factor and will not affect any statistical conclusions, i.e. this weight function is optimally powerful for any cross section.

The quantity T_ν (Eq. 4.2) is the sum of two terms: the weights of photons from dark matter plus the weights of background photons. These terms are independent variables so the probability distribution function (PDF) for T_ν is the convolution of these individual PDFs. As in Geringer-Sameth and Koushiappas [1] (described in Chapter 2) we model the background processes using data from the region surrounding each dwarf galaxy. The fundamental assumption made is that the processes which give rise to the background nearby the dwarf also generate the background at the location of the dwarf.

For each dwarf we find the PDF of T_ν due only to background processes by sampling the photons in the region within 15° of the dwarf. Sources from the second Fermi LAT source catalog [196] are masked with 0.8° masks (the 95% containment angle for photons with energies greater than 10 GeV [197]). The sampling is performed by randomly placing 1° ROIs over the 15° field of view (rejecting those ROIs which overlap with a masked source, the ROI centered on the dwarf, or the boundary of the field of view). The photons in these ROIs are then weighted according to Eq. 4.3 and summed as in Eqs. 4.1 and 4.2.

In order to derive the PDF of T due to an annihilation signal, consider first a single dwarf T_ν as given in Eq. 4.2. The quantity T_ν is the sum of N_ν independent, positive random variables (the weights), where N_ν is drawn from a Poisson distri-

bution with mean μ_ν, the expected number of dark matter photons from dwarf ν. This distribution is known as a compound Poisson distribution [174]. The PDF for T due to dark matter (Eq. 4.1) for all the dwarfs is therefore the convolution of the individual compound Poisson distributions for each of the dwarfs. The PDF for each weight in the sum T_ν is the same and is found by dividing the energy-angular separation plane into infinitesimal bins and computing the probability that a detected dark matter photon will land in each bin. The weight assigned to a photon landing in each bin is set by Eq. 4.3.

There are several methods for finding the PDF of the compound Poisson distribution T_ν for dwarf ν. An early algorithm was developed by Panjer [198] but we take advantage of a straightforward and efficient fast Fourier transform (FFT) method [175] which has also found use in astrophysics [199–201].

For a single dwarf ν, let $\mathcal{F}_{w,\nu}$ be the Fourier transform (or characteristic function) of the probability distribution for the weight of a detected dark matter photon from ν. The Fourier transform of the PDF for T_ν (due to dark matter annihilation), denoted $\mathcal{F}_{T_\nu}$, is given by (see e.g. [175]),

$$\mathcal{F}_{T_\nu} = \exp[\mu_\nu \, (\mathcal{F}_{w,\nu} - 1)]. \tag{4.4}$$

To incorporate both signal and background photons into the PDF for T we use the fact that a convolution is equivalent to multiplication in Fourier space. The full PDF for T is

$$\mathcal{F}_T = \prod_\nu \exp[\mu_\nu(\mathcal{F}_{w,\nu} - 1)] \times \prod_\nu \mathcal{F}_{B,\nu} \tag{4.5}$$

where $\mathcal{F}_{B,\nu}$ is the Fourier transform of the empirically measured distribution of the sum of weights due to background processes for dwarf ν.

In practice the Fourier transforms are performed using an FFT on a discrete grid of possible T values. The single-event weight PDFs and the background PDFs are "tilted" [175] before taking the FFTs to form $\mathcal{F}_{w,\nu}$ and $\mathcal{F}_{B,\nu}$ and the PDF of T is "tilted back" after applying the inverse FFT to $\mathcal{F}_T$. The tilting prevents aliasing which can be induced by the FFT.

Expected signal and background

The search for a line proceeds by first using Eqs. 4.5 and 4.3 to derive the PDF of T under the null hypothesis that there is no dark matter signal (all μ_ν's are 0). The measured value of T, called T^*, is obtained by summing the weights of all photons in the 1° ROIs centered on each of the dwarfs. The significance of the detection is the probability that T would be measured to be less than T^* if the null hypothesis were true. For example, if there is 99.7% chance that $T < T^*$ then a line has been detected at 99.7%, or 3σ, significance.

The expected number of background counts b_Q is found by fitting a power law to all photons within 15° of the dwarf (excluding the central 1° and the masked sources). For purposes of weighting, the background is assumed to be statistically isotropic, i.e. independent of angular separation from the ROI center. This may not be true in practice due to the presence of unresolved sources; however, the background sampling automatically includes any non-Poisson aspect of the background in the PDF of T_ν (or equivalently in $\mathcal{F}_{B,\nu}$).

The expected number of dark matter annihilation events s_Q, detected from a particular dwarf, with energy between E and $E + dE$ and with angular separation

in a solid angle interval $d\Omega(\theta)$ is

$$s_Q = J \frac{\langle \sigma_A v \rangle}{8\pi M_\chi^2} \frac{dN_\gamma(E)}{dE} \epsilon(E)\, \mathrm{PSF}(E,\theta)\, dE\, d\Omega(\theta). \tag{4.6}$$

In the above M_χ is the mass of the dark matter particle, $\langle \sigma_A v \rangle$ is the velocity-averaged annihilation cross section into a pair of gamma-rays, and dN_γ/dE is the number of photons per energy interval emitted per annihilation. The point spread function $\mathrm{PSF}(E,\theta)$ is the probability per solid angle of detecting a photon of energy E an angular distance θ from the source, and $\epsilon(E)$ is the detector exposure in units of $\mathrm{cm}^2\mathrm{s}$. The quantity J quantifies the dark matter distribution within a particular dwarf [157, 158, 164, 202, 203, 161, 159, 155, 204].

We use the publicly available data from the Fermi Science Support Center (FSSC)[2] and version `v9r27p1` of the Fermi Science Tools. We extract all photons of `evclass` = 2 using the tool `gtselect` in the Mission Elapsed Time interval [239557417 - 357485329] in the energy range between 8 GeV and 1 TeV, and with `zmax` = `100`. We select good time intervals (with all standard recommendations as stated on the FSSC), and compute $\epsilon(E)$ and $\mathrm{PSF}(E,\theta)$ using `gtpsf` with the `P7SOURCE_V6` instrument response functions.

The dark matter annihilation is modeled as point source emission from each dwarf, and we utilize the values for J given by Ackermann *et al.* [118]. For a line search the energy dispersion of the detector can be important. We incorporate this uncertainty by giving a width to dN_γ/dE. The spectrum due to line emission is simply $dN_\gamma/dE = 2\delta(E - E_\gamma)$ (but see also [183, 205]). The 68% containment on the energy uncertainty of Fermi is approximately 10% for photon energies above 10 GeV. We model this energy uncertainty by setting the annihilation spectrum dN_γ/dE to

[2] `http://fermi.gsfc.nasa.gov/ssc/data/analysis/`

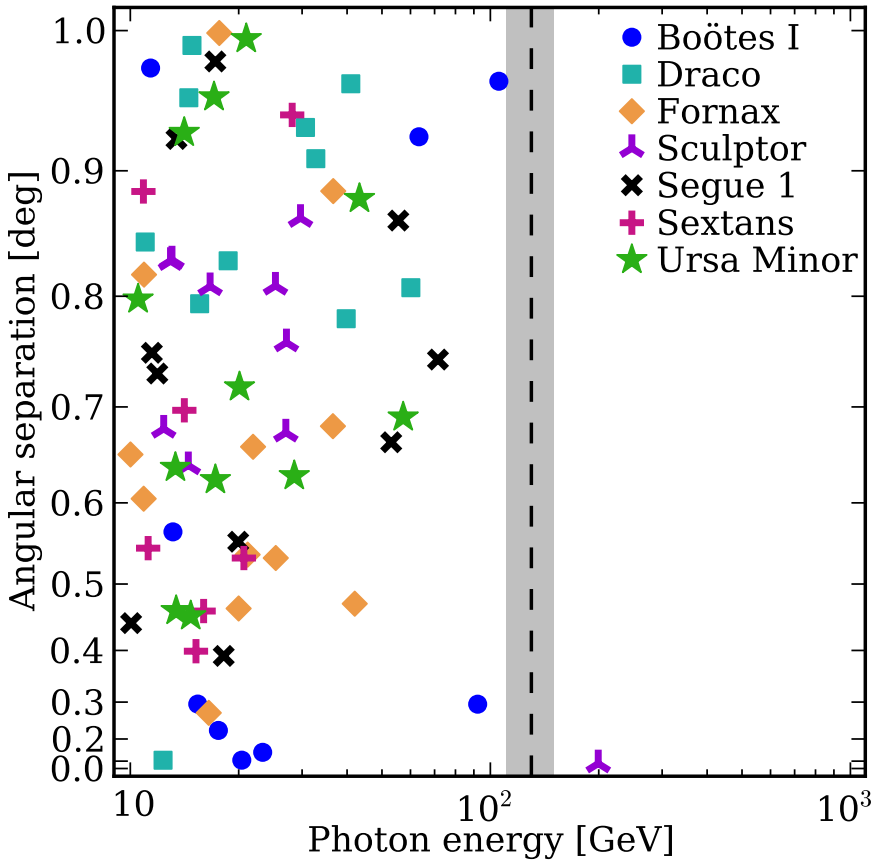

Figure 4.1: A snapshot of every photon having an energy between 10 GeV and 1 TeV that has been detected within 1° of each of the seven dwarfs. The black dashed line is at 130 GeV [182, 183]. The gray region is ±15% around 130 GeV, a rough gauge of the energy dispersion of the LAT. The vertical axis is scaled according to solid angle so that an isotropic distribution of photons will be spread uniformly along this axis.

be a Gaussian centered on M_χ, normalized to 2, with a standard deviation of 10% of the mean. We have reproduced the analysis with top hat distributions with widths from 5% to 30%. The effects are small and leave our conclusions unchanged.

Results

Figure 4.1 shows the individual photon events between 10 GeV and 1 TeV that were detected within 1° of each of the seven dwarfs. The vertical axis measures the angular separation between the event and the center of the dwarf. It is scaled according to

solid angle so that an isotropic distribution of events should be distributed uniformly over the vertical axis. There are no photons with energy within 15% of 130 GeV (gray shaded region). The 68% energy resolution of the LAT ranges from about 8% at 10 GeV to about 14% at 1 TeV while the 68% containment angle (PSF) varies from 0.3° to 0.2° over this energy range (95% containment is about 0.8°) [197]. We conclude that the *dwarfs show no evidence of a gamma-ray line at 130 GeV.*

Using the formalism described above we perform a search for line emission over a range of energies. A Gaussian energy spectrum with a standard deviation of 10% is used to calculate s_Q (Eqs. 4.3 and 4.6). We perform a separate search for each possible line energy, taking 100 log-spaced steps from 10 GeV to 1 TeV. The results of the search are illustrated in Fig. 4.2. Note that the inclusion of a trials factor dilutes the significance of any line. We can make a very rough estimate of the number of "independent" trials by assuming that a search for a line at E_γ uses the photons in the window $E_\gamma(1 \pm \alpha)$. If the energy of the $(-\alpha)$ edge of the window is E_1 the upper edge of the window is at an energy $E_2 = E_1\,(1+\alpha)/(1-\alpha)$. Therefore the number of "independent" (i.e. non-overlapping) windows n between $E_{\rm min} = 8$ GeV and $E_{\rm max} = 1$ TeV is specified by $E_{\rm max} = E_{\rm min}[(1+\alpha)/(1-\alpha)]^n$. An energy window of $\alpha = 0.10$ corresponds to about 24 trials. On the right vertical axis of Fig. 4.2 we plot the significance including a trials factor of 24 as a rough guide to the true significance of any tentative line. It is clear that the data do not strongly suggest that line emission is present at any energy.

Given that there is no evidence of line emission from the dwarfs we can place upper limits on the annihilation cross section into two photons. In this case, the weight choice analogous to Eq. 4.3 that maximizes the signal to noise ratio is $w(Q) = s_Q/(b_Q + s_Q)$ (see Eq. 3.7). For each mass we find the cross section above which there is less than a 5% chance of measuring the test statistic T to be smaller than

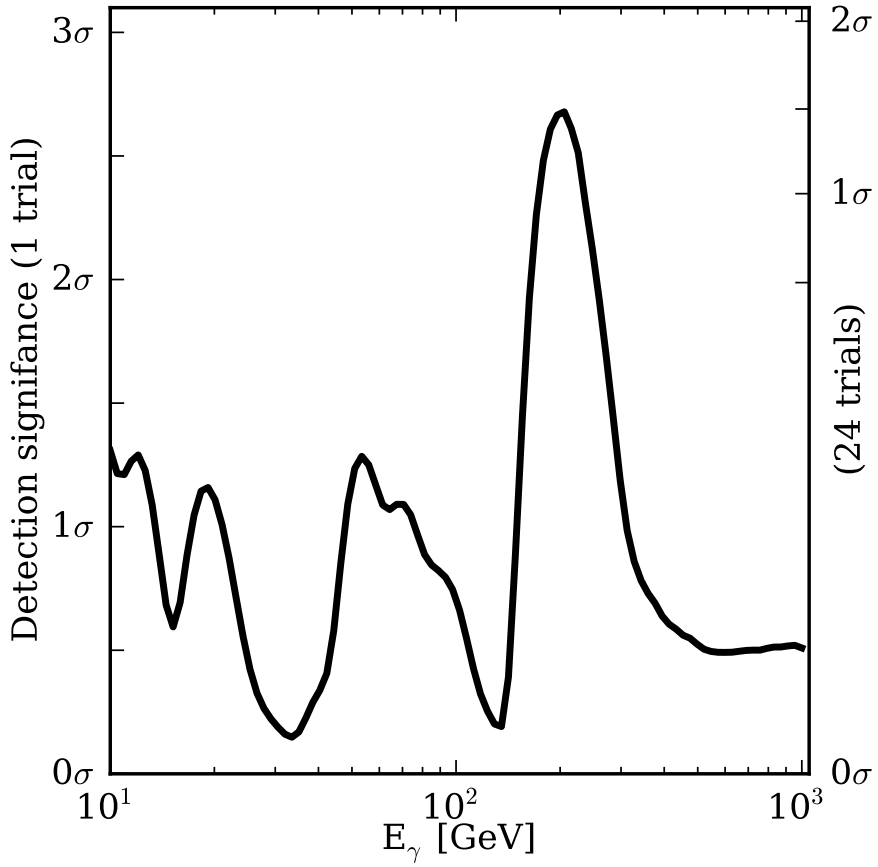

Figure 4.2: Results of the a search for line emission using an optimized combined search of seven dwarf galaxies. The horizontal axis represents the energy of the gamma-ray line searched for. The left vertical axis is the significance of the detection (in terms of Gaussian standard deviations). The right vertical axis incorporates a trials factor of 24, roughly the number of independent energies searched. The non-significant peak at 200 GeV is due to a single photon from Sculptor (see Fig. 4.1).

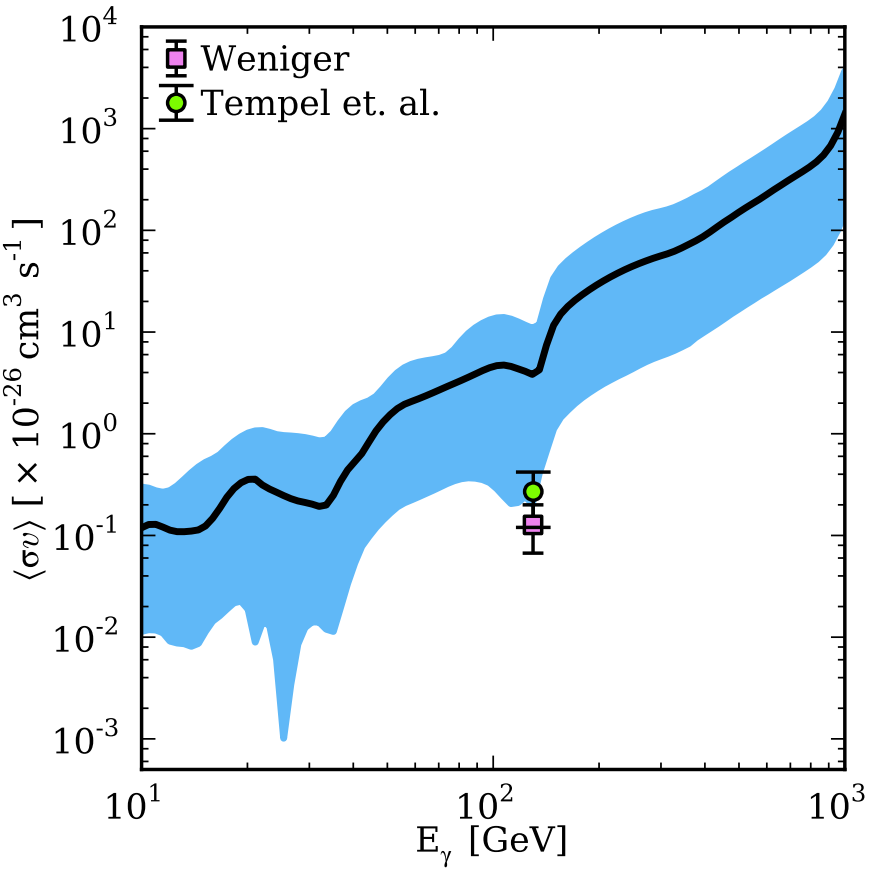

Figure 4.3: 95% upper limits on $\langle\sigma_A v\rangle$ for annihilation into a pair of photons each having energy E_γ. The black line is the limit using the best fit J values for the dwarfs. The blue region corresponds to the 95% systematic uncertainty in the estimates of J. The two points are the dark matter interpretations for the tentative signals observed by [182, 183] under the assumption of an Einasto dark matter profile and annihilation into two gamma-rays, with 95% error bars.

observed. The resulting upper limits are plotted in Fig. 4.3 (together with the results from [182, 183]). By far, the largest source of systematic uncertainty is in the J values for the dwarfs. The black line in the figure is the limit found when the J values are set to their best fit values found in Ackermann *et al.* [118]. The effect of varying the J values within their observational uncertainties is shown by the blue shaded region. One at a time, we set the J value for each dwarf to its upper or lower 95% error bar and recompute the 95% cross section upper limit. The differences induced by each dwarf are added in quadrature to produce the boundaries of the shaded region. This procedure gives an estimate of the systematic effect due to the difficulty of determining each dwarf's dark matter distribution.

Discussion

For annihilation channels producing continuum emission (e.g. into heavy quark or lepton pairs) dwarf galaxies provide strong limits on the annihilation cross section [1, 118, 161, 202, 206–213]. It is challenging to produce such limits from the Galactic center: despite the high dark matter density (J value hundreds to thousands of times larger than the dwarfs) the astrophysical background cannot be easily subtracted or modeled. However, a gamma-ray line search is not hindered by these backgrounds to the degree that a continuum search is. For this reason, the Galactic center may be a more attractive target when searching for line emission. The upper limits obtained by [214, 182] are much stronger than those obtained here from the dwarf data. A recent search by the Fermi collaboration for gamma-ray lines in the Galactic halo (including the Galactic center) [194] did not show evidence for a 130 GeV line and places stronger upper limits than found here.

It appears that the large increase in dark matter density, and the proximity of the Galactic center are much more constraining than are dwarf galaxies when it comes to line emission searches. At the present time dwarf galaxies can neither confirm nor deny a dark matter line interpretation of the Galactic center data.

Chapter Five

Detecting unresolved moving sources in a diffuse background

5.1 Introduction

Diffuse background light is very important in understanding conditions and classes of objects in the Universe. This is due to the fact that the spectral, spatial, and amplitude information in a diffuse background is linked to the properties of the otherwise unresolved contributing sources. For example, microwave background measurements include contributions of cosmic origin [215], as well as foregrounds of Galactic origin [216–220]. As another example, γ-ray background measurements include contributions from unresolved blazars [221–230], inverse Compton scattering of CMB photons by electrons accelerated at shocks around galaxy clusters and cosmic filaments [231–234], starburst galaxies [235], cosmic ray interactions with atomic and molecular gas in the Milky Way [236, 237], as well as the possible annihilation of dark matter [238–243, 200, 244–247, 201]. All searches for new sources of emission require an as-complete-as-possible understanding of the astrophysical backgrounds.

Background events may be divided into two classes. Some events are generated by localized sources while others are generated by mechanisms which cannot be localized. In the first class the sources can be either spatially fixed (in celestial coordinates) or may exhibit proper motion (i.e. over a period of time their displacements are larger than the angular resolution of the detector).

Using again the diffuse γ-ray background as an example, unresolved blazars, starburst galaxies, and emission from structure formation shocks would be considered spatially fixed sources of background. Cosmic ray events with interstellar gas would be considered a non-localized random process. Sources of background which will exhibit proper motion include the interaction of energetic cosmic rays with solar system bodies (e.g., small objects in the asteroid belt or objects in the Kuiper belt

and the Oort cloud) [248–250], dark matter annihilation around primordial black holes [251, 252], and potentially nearby remnants of high density dark matter density peaks [253–256]. In all these cases, individual emission from any single object is not distinguishable, but the sum of these contributions may contribute to the diffuse γ-ray background.

Correlations between individual events can help disentangle the contribution of various sources to the background. In this chapter I present a formalism and a technique that can be used to identify the presence of background sources that exhibit spatial motion. In Sec. 5.2 I present an overview of the problem. Section 5.3 contains detailed definitions that are used in the statistical techniques that follow. This allows us to write down the formal definition of the spacetime 2-point correlation function, which can be used to extract the moving signal in the diffuse background. In Sec. 5.4 I derive the form of the spacetime correlation function in 2 dimensions. A quantitive account of the uncertainty in the method is found in Sec. 5.5. In Sec. 5.7 I demonstrate the method's robustness in toy experiments and comment about the use of an instrumental point spread function. I extend the formalism to realistic problems in 3 dimensions in Sec. 5.8, discuss generalizations of the formalism in Sec. 6.5m and explore applications and conclude in Sec. 5.10.

5.2 Overview of the problem

Suppose we have some objects moving on a 2-dimensional surface, each with a constant velocity. Every so often the objects emit photons, which, when detected, we call "events". We record the location and time of each photon detection. The problem we are interested in is to take this collection of events and extract information

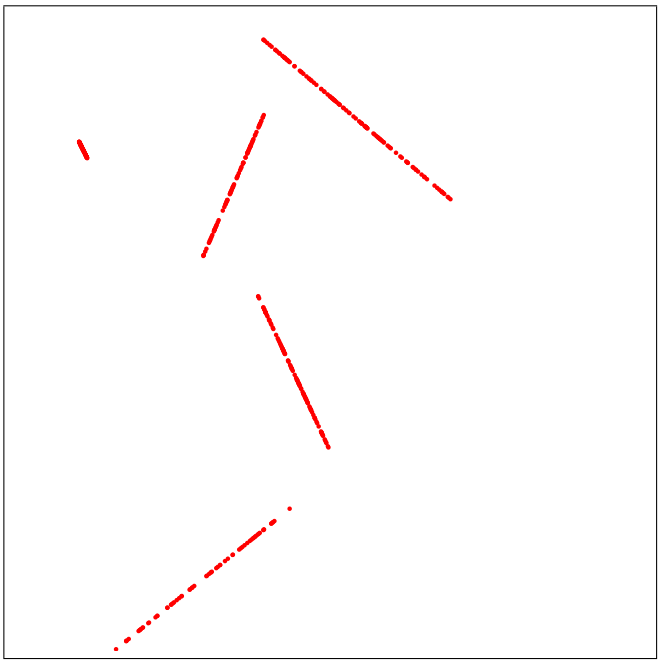

Figure 5.1: Illustration of the two limits in the problem. The upper figure contains 5 objects each with event rate 10 and the one on the lower left contains 50,000 objects with event rate 0.01. The lower two figures contain the same number of events but those on the right are distributed randomly. Naively, it is impossible to tell which of the last two figures contains random events and which contains moving objects.

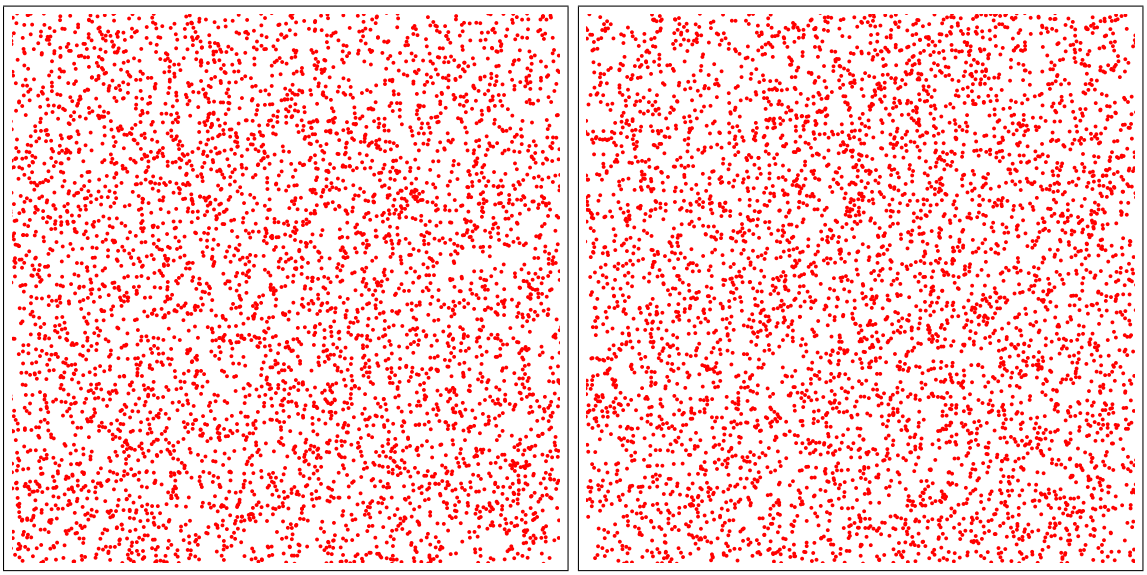

about the objects: their existence, their velocity distribution, their density distribution, and their event rate or luminosity (i.e. the rate at which photons are emitted from each object).

There are two natural variables in this problem which ought to determine how difficult it will be to extract this information: the event rate of the objects and their number density. If there are very few objects and their luminosities are very high it should be easy to identify the path of each object individually. In the opposite limit the objects' luminosities are small but their number density is large. In this case it will be difficult to identify the sequences of events that trace the paths corresponding to individual objects.

These two limits are represented in Fig. 5.1. Each panel in Fig. 5.1 is a plot of the location of all events in 10 arbitrary units of time[1]. The top panel contains 5 objects each having a luminosity of 10 and an average speed of 5. The lower left panel contains 50,000 objects each with an event rate of 0.01 and drawn from the same velocity distribution as before. The lower right panel contains the same number of events as on the left, but they occur at random positions and times (i.e., there are no "objects"). In the top panel it is easy to measure the speed and event rate of every object (each generating about 100 events in total). This task is impossible, by eye, for the lower left panel where each object generates 0.1 events on average. Indeed, it is even difficult to say whether or not the events come from objects at all, or if they are simply generated randomly as in the right panel. In practice, the top panel is analogous to resolvable sources in the absence of any contaminating backgrounds while the lower left and right panels represent diffuse backgrounds in the sky. Our goal is to be able to distinguish between the lower left and right panels

[1]In these examples time and distance have arbitrary units and from now on these units will be set equal to 1. A phrase like "luminosity equal to 10" means an event rate of 10 per unit time; "an average speed of 5" means 5 units of distance per unit time, etc.

while learning something about the objects on the left panel.

The technique we employ is an application of the 2-point correlation function. One takes every pair of events and calculates their time separation and "velocity separation" (their spatial separation divided by their temporal separation). One can then bin this data and make a 3-dimensional plot of number of pairs as a function of both time separation and velocity separation. The shape of this surface reveals information about the contributing objects. For instance, if all the objects are moving exactly at speed v, there will be lots of pairs of events whose velocity separation is v. The effect will be a ridge in this 2-dimensional parameter space.

The situation can be made more realistic. Instead of the moving objects all having speed v, their speeds could be drawn from a distribution. Their event rates could also be drawn from a distribution. In fact we might have many different populations of objects each having a different set of distributions for speed and luminosity. On top of this we could add a set of completely random events: a Poisson process such that there is some constant probability that an event occurs in any small region of spacetime. Below we will systematically discuss all these possibilities. First we present the simple 2-dimensional case with one class of moving objects along with a component of random events. This is the easiest way to present our formalism. Then we straightforwardly generalize to a realistic case where a diffuse background is made up of signals coming from various populations of objects as well as random processes.

5.3 Definitions

The analysis takes place on a 2-dimensional sky map, which is a collection of discrete signals that we define as "events". Each event is assigned a spatial coordinate (position) and a time coordinate. For example, in the case of the Fermi Gamma-ray Space Telescope (Fermi), discrete signals are γ-ray events recorded by the Large Area Telescope (LAT). The position is the location on the sky where the photon originated, and the time is the time of detection. It is important to note that in realistic experiments the data comes not as a list of (position, time) for each event but as a list of (point spread function, time) for each event. The analysis that follows can be reworked for this more realistic situation. However, we will start out by assuming that we simply have a collection of events where each event is specified by a position and a time.

As we are interested in sources of events that can have velocities we also need a notion of distance. For realistic sky maps, the distance between two events is defined to be their angular separation. In our toy model with objects moving on a 2-dimensional surface, the distance between events is their Euclidean distance. We also define the "velocity separation" between two events to be the distance between them divided by their time separation. With these definitions, the appropriate way to visualize the data is in a spacetime diagram where each event has both position and time coordinates.

We will employ the 2-point function in a similar way to its use in galaxy-galaxy correlation studies. The galaxies correspond to what we have called events. To calculate the galaxy 2-point function for a particular angular separation θ one counts the number of pairs of galaxies in the sky map whose angular separation is between

θ and $\theta + \Delta\theta$. That is, for every galaxy one looks in a ring of radius θ and width $\Delta\theta$ around the galaxy and counts the number of other galaxies in this ring. The count is denoted by $C(\theta, \theta + \Delta\theta)(p)$, where p is an index labeling the central galaxy (see Fig. 5.2). If the events were distributed randomly one expects to find on average $\rho V(\theta, \theta + \Delta\theta)$ galaxies in this ring, where ρ is the overall density of galaxies (number of galaxies in the sky map divided by the area of the map) and $V(\theta, \theta + \Delta\theta)$ is the area of the ring, equal to $2\pi(\cos(\theta) - \cos(\theta + \Delta\theta))$. One then computes the correlation function ξ at separation θ according to

$$\xi(\theta, \theta + \Delta\theta) = \left\langle \frac{C(\theta, \theta + \Delta\theta)(p) - \rho V(\theta, \theta + \Delta\theta)}{\rho V(\theta, \theta + \Delta\theta)} \right\rangle, \tag{5.1}$$

where the average is taken over the index p of each galaxy. The correlation function $\xi(\theta, \theta + \Delta\theta)$ is interpreted as the fractional increase in probability (above random) that there is a galaxy in a ring between θ and $\theta + \Delta\theta$ around any given galaxy. This is most easily seen by rearranging (5.1) into the form $C = \rho V(1 + \xi)$. Notice that the correlation function is inherently a function of the shape and size of the ring in which the search for pairs of events is performed.

Now we apply the 2-point function in our situation. We denote spacetime by $\mathcal{S}$ and we label spacetime events with the abstract index p, which carries all the information we have about the event. For example, for the event p, $p(t)$ is the time the event occurred, $p(x)$ is the x-coordinate of the event, etc. We define the spacetime 2-point function as follows. For an event at p, let $V(p) \subset \mathcal{S}$ denote some volume of spacetime which is analogous to the shaded region in Fig. 5.2. When there is no confusion $V(p)$ may also refer to the spacetime volume of the region $V(p)$. Two choices for $V(p)$ are illustrated in Fig. 5.3. Let the number of events that occur within the region $V(p)$ be denoted by $C(p)$. When it is important to remember that $C(p)$ depends on the region $V(p)$ we will write it as $C(p; V)$. The spacetime 2-point

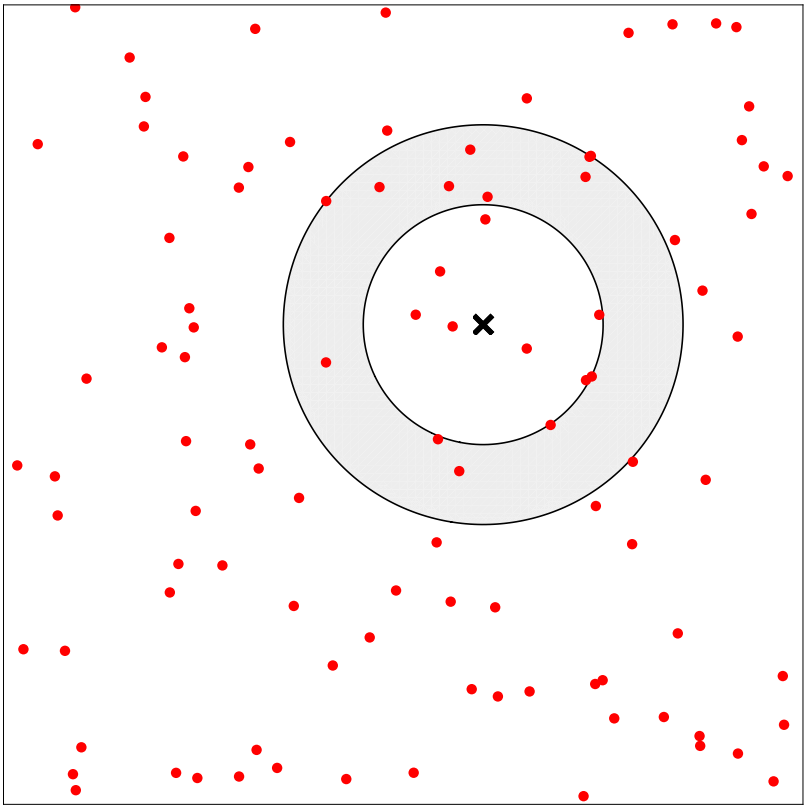

Figure 5.2: For a galaxy-galaxy correlation function we look in rings of a certain size centered on each galaxy and count the number of galaxies that lie inside each ring. The ring shown is $V(p)$, centered on the galaxy (represented by the black $\times$) having coordinates p.

function is then given by

$$\xi(V) \equiv \left\langle \frac{C(p;V) - \rho V(p)}{\rho V(p)} \right\rangle, \tag{5.2}$$

where the average[2] is taken over every event in the sky map (i.e. over p) and $V(p)$ denotes the spacetime volume of the region $V(p)$. As before, ρ is equal to the overall spacetime density of events (total number of events divided by the spacetime volume of the sky map). In a realistic application ρ will have dimensions of flux: events per square degree per time.

If the events were all generated by a completely random Poisson process we would expect $C(p;V) = \rho V(p)$ on average and $\xi(V)$ would be 0. The 2-point function $\xi(V)$ is therefore to be interpreted as the fractional probability above random that the region $V(p)$ contains an event given that there is an event at p. In the rest of this paper we will develop a formalism for deriving $\xi(V)$.

5.4 2-dimensional model

5.4.1 Ingredients

Consider objects moving over a two dimensional surface with constant speeds and each having the same event rate (a "blinking rate", so to speak). Each event is

[2]In order to be thorough we should really define ξ by $\xi(p;V) \equiv \langle [C(p;V) - \rho V(p)]/\rho V(p) \rangle_{\mathrm{U}}$, where the average is taken over an ensemble of Universes. Then we assume that our physical situation is spacetime translation invariant so that $\xi(p;V)$ actually does not depend on the location p. Finally, in order to *estimate* ξ from a set of data we claim that the average of $\xi(p;V)$ over an ensemble of Universes is equal to the average taken over all the events in our dataset. These are exactly the assumptions which must be made in the theory of galaxy n-point functions (referred to as ergodic conditions). We will have more to say on the subject of estimators below.

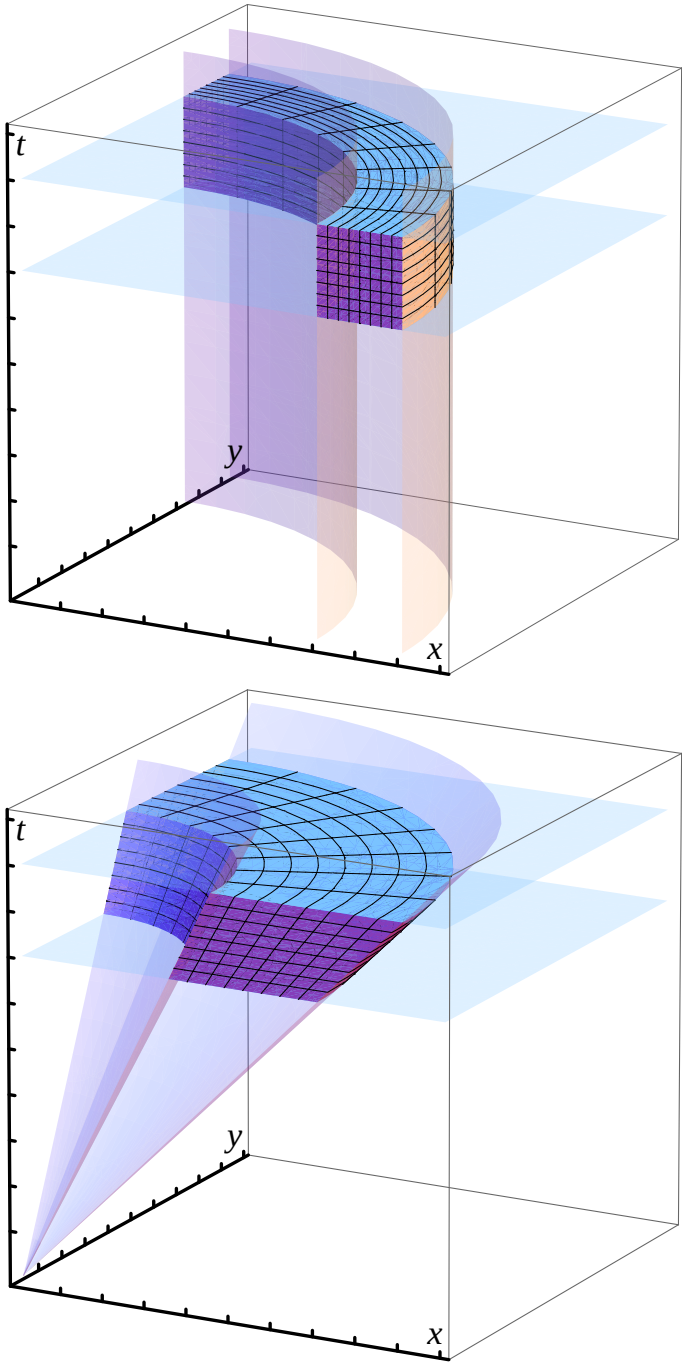

Figure 5.3: The spacetime regions $V(r_1, r_2; t_1, t_2)(p)$ and $V(v_1, v_2; t_1, t_2)(p)$ where p is at the origin. The vertical axis is time and the horizontal axes are the x and y coordinates. In the upper figure the region between the two cylinders contains all events which have a radial distance from p between r_1 and r_2. In the lower figure the region between the two cones represents the possible worldlines of an object starting at p and having a speed between v_1 and v_2. Imposing a time separation between t_1 and t_2 gives the filled regions.

then associated with an x, y, and t value and our "sky map" consists of the list of (x, y, t) for each event. The "blinking" of an object is a Poisson process with mean rate λ: during the time dt each object has a λdt chance of generating an event. Let the average density of objects be given by n, which has units of objects per area. The objects have speeds drawn from the distribution $P_{\rm v}(v)$: the probability for any given object to have a speed between v and $v + dv$ is $P_{\rm v}(v)dv$. We consider the case where the velocity distribution is isotropic (accommodating the more general case, $P_{\vec{\rm v}}(\vec{v})d^2\vec{v}$, is straightforward). Finally, some fraction of the events will come from a random (Poisson) component with spacetime density ρ_0: there is a $\rho_0\, dx\, dy\, dt$ probability of having such an event in any spacetime volume $dx\, dy\, dt$.

5.4.2 The form of $V(p)$ in 2 dimensions

There are many possible choices for the spacetime region $V(p)$. The simplest one is

$$\begin{aligned} V(r_1, r_2; t_1, t_2)(p) \equiv & \{p' \in \mathcal{S} : t_1 \leq p'(t) - p(t) < t_2 \\ & \wedge\ r_1 \leq d(p', p) < r_2\}, \end{aligned} \tag{5.3}$$

where $d(p', p)$ is the spatial separation of spacetime events p and p' and $\wedge$ is the logical AND operator. This volume corresponds to all the events whose temporal separation from p is between t_1 and t_2 and whose spatial separation is between r_1 and r_2: a ring in spacetime with rectangular cross section (see upper panel of Fig. 5.3). The volume of such a region is simply

$$V(r_1, r_2; t_1, t_2) = \pi(r_2^2 - r_1^2)(t_2 - t_1). \tag{5.4}$$

A more convenient choice for $V(p)$ is

$$\begin{aligned} V(v_1, v_2; t_1, t_2)(p) \equiv & \{p' \in \mathcal{S} : t_1 \leq p'(t) - p(t) < t_2 \\ & \wedge\ v_1 \leq \frac{d(p', p)}{|p'(t) - p(t)|} < v_2\}. \end{aligned} \tag{5.5}$$

This region is interpreted as the volume of spacetime that an object might explore between time t_1 and t_2 if it started at p and had any speed in the range from v_1 to v_2. $V(v_1, v_2; t_1, t_2)(p)$ is illustrated in the lower panel of Fig. 5.3 for the case where p is at the origin of spacetime coordinates. If the event was an object which had velocity between v_1 and v_2 its worldline would lie between the cones $x^2 + y^2 = v_1 t^2$ and $x^2 + y^2 = v_2 t^2$ and we only consider the region where $t_1 \leq |p'(t) - p(t)| < t_2$. The volume of this region may be found by slicing the shaded region in the $x - t$ plane, and rotating each small piece around the $t-$axis. The result is

$$V(v_1, v_2; t_1, t_2) = \int_{t_1}^{t_2} \int_{v_1 t}^{v_2 t} 2\pi x dx dt = \frac{\pi}{3}(v_2^2 - v_1^2)(t_2^3 - t_1^3). \tag{5.6}$$

5.4.3 Coordinate systems

The forms of $V(p)$ presented in the previous section are easiest to visualize in the cartesian coordinate system (x, y, t) (see Fig 5.3). However, a more appropriate choice of spacetime coordinates are (v, t, ϕ), defined by

$$\begin{aligned} v &= \sqrt{(x^2 + y^2)}/|t| \\ t &= t \\ \phi &= \tan^{-1}(y/x). \end{aligned} \tag{5.7}$$

These are just cylindrical coordinates (r, z, ϕ) but with r scaled by the absolute value of z. The Jacobian for this change of variables is

$$dV(v,t,\phi) \equiv dx\,dy\,dt = vt^2 dv\,dt\,d\phi. \tag{5.8}$$

The volume V of any region of spacetime $V(p)$ is given by

$$V = \int\limits_{V(p)} dV(v,t,\phi) = \int\limits_{V(p)} vt^2 dv\,dt\,d\phi\,. \tag{5.9}$$

For example, we can recover (5.4) as

$$V(r_1, r_2;\, t_1, t_2) = \int_{t_1}^{t_2} \int_{r_1/t}^{r_2/t} \int_0^{2\pi} dV(v,t,\phi)$$

and (5.6) as

$$V(v_1, v_2;\, t_1, t_2) = \int_{t_1}^{t_2} \int_{v_1}^{v_2} \int_0^{2\pi} dV(v,t,\phi).$$

For later use we define the $(v,t,\phi)_p$ coordinate system which is the same as the coordinate system described in (5.7) except the center of coordinates ($v = 0$, $t \to 0$) is at the spacetime point p. We also define the corresponding volume element $dV_p(v,t,\phi)$ or dV_p for short. The region $dV_p(v,t,\phi)$ is the infinitesimal version of (5.5), i.e $dV_p(v,t,\phi) = V(v, v+dv;\, t, t+dt)$, only not rotated about the t-axis.

Finally we should note that it is just as easy to derive our results for rectangular coordinates. One just uses the coordinate system (v_x, v_y, t) where

$$\begin{aligned} v_x &= x/t \\ v_y &= y/t \\ t &= t, \end{aligned} \tag{5.10}$$

instead of (5.7). The analogue of (5.8) is then

$$dV(v_x, v_y, t) \equiv dx\, dy\, dt = t^2 dv_x\, dv_y\, dt. \tag{5.11}$$

5.4.4 The form of $\xi(V)$ in 2 dimensions

Our goal is to write down an analytic expression for (5.2). In the previous subsection we showed how to calculate the volume $V(p)$. Now we move on to $C(p;V)$, which can be interpreted as follows. Given an event at p, $C(p;V)$ is the probability[3] of finding another event in the spacetime region $V(p)$.

There are two processes by which an event might occur in $V(p)$. Accordingly, we can break up $C(p;V)$ into the sum of two terms: $C(p;V)$ = [the probability of getting an event from an object that was at p] + [the probability of getting an event from any other source]. The first term can be thought about in a series of steps: given an event at p find the probability that it came from an object, that this object moves into the region $V(p)$, and that this object triggers a new event while in this region.

The probability p_1 that any given event came from a moving object (as opposed to being generated by the Poisson component of the background) is the ratio of the flux from moving objects to the total flux:

$$\mathrm{p}_1 = \frac{n\lambda}{n\lambda + \rho_0} = \frac{\rho_1}{\rho}, \tag{5.12}$$

where $\rho_1 \equiv n\lambda$ is the average flux of the moving objects, n is the number density

[3] Or, if it is greater than 1, $C(p;V)$ is the expected number of events in the region $V(p)$.

of objects, and λ is the event rate for an object. As before, ρ is the total spacetime density of all events (i.e. the overall flux).

The probability that the object moves into the region $dV_p(v,t,\phi)$ is simply the probability that its speed is between v and $v+dv$, $P_{\rm v}(v)dv$, multiplied by $d\phi/2\pi$, the probability that it is moving in a direction[4] between ϕ and $\phi+d\phi$. If the object makes it into the region $V(p)$ the probability of it generating a second event is λdt. Therefore, the probability that there was an object at p which moved into $V(p)$ and generated another event is[5].

$$\mathrm{p}_1 \int\limits_{V(p)} P_{\rm v}(v)\, dv\, \lambda dt\, \frac{d\phi}{2\pi}. \tag{5.13}$$

The second term in $C(p;V)$ is simply $\rho V(p)$, where $\rho\, dx\, dy\, dt$ is the probability that any random spacetime volume $dx\, dy\, dt$ contains an event from either an object or the random component (note that $\rho = \rho_1 + \rho_0$).

Therefore, putting together these parts and plugging them into (5.2) we find

$$\begin{aligned} \xi(V) &= \left\langle \frac{C(p;V) - \rho V(p)}{\rho V(p)} \right\rangle \\ &= \frac{\mathrm{p}_1 \int_{V(p)} P_{\rm v}(v)\, dv\, \lambda dt\, d\phi/2\pi}{\rho V(p)} \\ &= \frac{\rho_1 \int_{V(p)} P_{\rm v}(v)\, dv\, \lambda dt\, d\phi/2\pi}{(\rho_1+\rho_0)^2\, V(p)}. \end{aligned} \tag{5.14}$$

As is usually done for galaxy-galaxy correlation functions let's see what happens

[4] If the objects do not have an isotropic velocity distribution then this probability is $\mathrm{P}_{\vec{v}}(v,\phi)dvd\phi$, where $\mathrm{P}_{\vec{v}}(v,\phi)$ is the probability density for the velocity *vector*.

[5] In full generality this equation would be $\mathrm{p}_1 \int_{V(p)} \mathrm{P}_{\vec{v}}(v,\phi)\lambda(t)\, dv\, dt\, d\phi$, where $\lambda(t)dt$ is the probability that an object which generated an event at $t=0$ generates another event in the time interval between t and $t+dt$.

when we take the limit $V(p) \to dV_p(v,t,\phi)$. Using (5.8) we see that

$$\xi(V) \to \xi[dV(v,t,\phi)] = \frac{\rho_1 \lambda}{2\pi(\rho_1+\rho_0)^2} \frac{P_{\rm v}(v)}{vt^2}. \tag{5.15}$$

This limit is finite and the function ξ traces the velocity distribution of the population of objects. Therefore, if ξ can be measured for multiple values of v then it is possible to directly reconstruct both the velocity distribution of the moving objects and information about their abundance and luminosity.

5.5 The error in ξ

Getting a handle on the error $\Delta\xi$ in a measurement of $\xi(V)$ is just as important as calculating $\xi(V)$ itself: any practical application of this method will reveal nothing if the uncertainty in $\xi(V)$ is comparable to $\xi(V)$. The zeroth order discovery that can be made using the 2-point function is the detection of the presence of moving objects. This is done by rejecting the hypothesis that $\xi(V) = 0$ for all choices of $V(p)$, which is possible only if $\Delta\xi/\xi(V) < 1$ for some choices of $V(p)$. An estimate of the error is also essential when fitting the theoretical value for ξ to the data; i.e. when performing a χ^2 fit to determine the physical parameters describing the density, luminosity, and velocity distribution of contributing sources.

Fortunately, the errors in correlation functions have been thoroughly studied in the case of galaxy-galaxy correlations [257–265]. We emphasize that all the technology that has been developed for calculating 2-point functions for galaxies and quantifying their errors can (and should) be straightforwardly applied to our 2-point function. As stated before, the only conceptual difference between the two tools is

the choice of $V(p)$.

In particular, we apply the results of Landy and Szalay [261] (hereafter LS93) to the present problem. In the examples below we measure $\xi(V)$ using an unbiased estimator which is identical to the DD/RR ratio in LS93. This is done for simplicity. The unbiased LS93 $(DD - 2DR + RR)/RR$ estimator was shown to have a smaller variance and should be used in practical applications. (In LS93, DR refers to the cross-correlation of the observed data with sets of completely random data, while DD and RR are the auto-correlation functions computed for the data and for a completely random set of data, respectively.)

To quantify the error in $\xi(V)$ we adapt the LS93 expression for the variance of the $(DD - 2DR + RR)/RR$ estimator for small correlations (i.e. small values of $\xi(V)$, likely in cases of physical interest). For a given shape $V(p)$ (with spacetime volume V) the variance of the estimator is given by

$$\Delta\xi^2(V) = \frac{[1 + \xi(V)]^2}{N\rho V}, \tag{5.16}$$

where N is the total number of events in the sky map. This can be seen to be the same as Eqs. 43 and 48 in LS93 by writing $\rho = N/\mathcal{V}$, where $\mathcal{V}$ is the total spacetime volume of the sky map and noting that $V(p)/\mathcal{V}$ is equal to LS93's $G_p(\theta)$. The signal to noise ratio is then

$$\frac{\xi(V)}{\Delta\xi(V)} = \frac{\xi(V)}{1 + \xi(V)}\sqrt{N\rho V}. \tag{5.17}$$

These expressions should be used to determine the optimal volumes $V(p)$ for any given application. Ideally, $V(p)$ should be chosen to make the signal to noise ratio large while keeping $V(p)$ small enough that many choices for $V(p)$ can be measured for the sky map. This dilemma occurs with galaxy-galaxy correlation studies as

well. An annulus of specific size (see Fig. 5.2) corresponds to one choice of $V(p)$. One would like to choose the width of the annulus as small as possible so that the correlation function can be measured at many different angular scales. However, the smaller the width of the annulus the larger the uncertainty in the measured value of the 2-point function.

As is well-known in galaxy-galaxy correlation studies, measurements of ξ at two different angular sizes can be highly correlated. This issue will also affect any measurement of the spacetime 2-point function: the measured $\xi(V)$ for different choices of $V(p)$ may be correlated. Therefore, a χ^2 fitting to extract physical parameters should include an estimate of the covariance of $\xi(V)$ between different $V(p)$'s. A variety of methods have been developed to estimate or predict this covariance matrix. Many of these are trivially adapted for use in this case. Bootstrapping (e.g. [266–268]) and jackknife resampling [269, 270] require measuring the correlation function on various subsets of the full data set and analyzing the variation among these estimates of ξ. If generating fake data sets is feasible then one can simply measure the correlation function on many fake maps to find the covariance of $\xi(V)$ between various $V(p)$'s.

5.6 Point spread function and computational considerations

In this section we discuss two ways to include information about the point spread function (PSF) into the derivation of the form of the 2-point function. This will serve as a guide for incorporating the PSF in realistic applications.

The PSF of a detector quantifies the uncertainty in its measurement of the locations of events in spacetime [271]. The PSF typically takes the form $\mathrm{PSF}(p_\mathrm{t} - p_\mathrm{o})$, where p_t is the true location of the event and p_o is the location that the detector reports, the "observed" location. The PSF is a probability density on spacetime: $\mathrm{PSF}(p_\mathrm{t} - p_\mathrm{o})dV$ is the probability that if the detector reports an event at p_o it actually arrived from the spacetime region dV centered at p_t[6]. As a result, $\int \mathrm{PSF}(p_\mathrm{t} - p_\mathrm{o})dV_\mathrm{t} = 1$. Additionally, there is the probability $\mathrm{p_d}$ that if a signal (e.g. a photon) arrives at the detector it will actually be detected as an event.

If we are given the PSF for a given event we can do a more precise job of computing $C(p; V)$. As above we want to answer the question: given that the detector reported an event at p_o what is the probability that the detector reports another event in the spacetime region $V(p)$?

If the detector reports an event at p there is a $\mathrm{p_1}$ chance that it received a signal from a moving object. But the true location of the object could be anywhere, with probability given by the PSF. The object can have any velocity and can emit a signal at any later time. This signal has a $\mathrm{p_d}$ chance of being detected. The location of the observed event is again determined by the PSF. Specifically, we have

$$\begin{aligned} C(p;V) &= \mathrm{p_1} \int\limits_{p_\mathrm{t}\in\mathcal{S}} \mathrm{PSF}(p_\mathrm{t} - p)\, dV_p(v_\mathrm{t}, t_\mathrm{t}, \phi_\mathrm{t}) \\ &\times \int\limits_{p'_\mathrm{t}\in\mathcal{S}} \frac{1}{2\pi} P_\mathrm{v}(v')\lambda \mathrm{p_d} dv'\, dt'\, d\phi' \\ &\times \int\limits_{p_\mathrm{o}\in V(p)} \mathrm{PSF}(p'_\mathrm{t} - p_\mathrm{o})\, dV_{p'_\mathrm{t}}(v_\mathrm{o}, t_\mathrm{o}, \phi_\mathrm{o}). \end{aligned} \tag{5.18}$$

[6]Because the time resolution of detectors is generally excellent compared with the spatial (or angular) resolution, the PSF is usually given as a function of spatial coordinates only. The PSF we have defined would then be equal to $\delta(t_\mathrm{t} - t_\mathrm{o})\,\mathrm{PSF}(\vec{r}_\mathrm{t} - \vec{r}_\mathrm{o})$.

In words, there is a $\mathrm{p_1}$ chance that the observed event at p came from a moving object. Given that it came from a moving object there is a $\mathrm{PSF}(p_\mathrm{t} - p)\, dV_p(v_\mathrm{t}, t_\mathrm{t}, \phi_\mathrm{t})$ chance the event actually occurred in the region $dV_p(v_\mathrm{t}, t_\mathrm{t}, \phi_\mathrm{t})$ around the point $p_\mathrm{t} = (v_\mathrm{t}, t_\mathrm{t}, \phi_\mathrm{t})_p$ (recall the definition of dV_p at the end of the section on the choice of $V(p)$). Then there is a $(1/2\pi)P_\mathrm{v}(v')\lambda \mathrm{p_d}\, dv'\, dt'\, d\phi'$ chance that the object moves into the region $dV_{p_\mathrm{t}}(v', t', \phi')$ around the point $p'_\mathrm{t} = (v', t', \phi')_{p_\mathrm{t}}$ and emits a signal which is reported by the detector. Finally there is a $\mathrm{PSF}(p'_\mathrm{t} - p_\mathrm{o})\, dV_{p'_\mathrm{t}}(v_\mathrm{o}, t_\mathrm{o}, \phi_\mathrm{o})$ chance that this event is reported as having occured in the region $dV_{p'_\mathrm{t}}(v_\mathrm{o}, t_\mathrm{o}, \phi_\mathrm{o})$ around the point $p_\mathrm{o} = (v_\mathrm{o}, t_\mathrm{o}, \phi_\mathrm{o})_{p'_\mathrm{t}}$.

All the possibilities are taken into account by integrating p_t and p'_t over all of spacetime (the object could actually have been located at any point and could have moved to any other point) and by integrating p_o over the region $V(p)$ (we are only interested in the possibilities where the detector reports the second event in the region $V(p)$). For clarity we have omitted the $\rho V(p)$ term in $C(p; V)$, which represents the probability of a reported event in $V(p)$ from any source besides an object moving from p into $V(p)$. One can show that (5.18) reduces to the numerator of (5.14) when $\mathrm{PSF}(p_\mathrm{t} - p_\mathrm{o}) = \delta(p_\mathrm{t} - p_\mathrm{o})$ and $\mathrm{p_d} = 1$.

The spacetime correlation function is an example of a 2-point correlation function and so any method that is used to compute 2-point functions may also be used here. In galaxy-galaxy studies, the galaxies are localized sources and the 2-point function is measured by counting pairs of galaxies which have a particular separation. When looking for moving objects using gamma-ray data, for instance, the events are also localized. Computational procedures then carry over directly. Typically, counting pairs of events is an N^2 process[7]. For example, in gamma-ray diffuse studies the

[7] We point out that efficient algorithms with better than N^2 scaling have recently been developed. See, for example, [272–274].

number of events is proportional to the observation time as well as to the effective area of the detector.

In other situations the data do not come as localized events but as a continuous amplitude across the sky. This case can be treated by first discretizing the survey area into small "cells" or pixels. Each pixel now has a continuous value. For a particular $V(p)$, the correlation function is found by multiplying the value of the pixel p by the sum of the values in the pixels in the volume $V(p)$. The expected value of this quantity (i.e. the denominator in (5.2)) is the average pixel amplitude squared multiplied by the volume of $V(p)$.

This method of computing the 2-point function can be used as an alternative way to account for the detector point spread function. Following Morales *et al.* [271], every discrete photon event in spacetime is replaced by its point spread function. The overlap of the point spread functions for all observed events forms a continuous density over the survey area and observation window. The 2-point correlation function for any choice of $V(p)$ can then be measured as described above. We note that this method suffers no performance penalty for increased numbers of observed events because the events are essentially binned into pixels in spacetime, with each pixel having a value given by the linear superposition of all contributing PSFs.

5.7 Examples of the 2-Dimensional formalism

In this section we will demonstrate the accuracy of the derivations by measuring ξ for three different simulations in which the objects move according to a specific speed distribution. A generic choice for $P_{\rm v}$ is the Rayleigh distribution: the speed

distribution for a 2-dimensional isotropic Gaussian velocity distribution. It has the form

$$P_{\rm v}(v) = \frac{v}{a^2}\, e^{-v^2/2a^2}, \tag{5.19}$$

with mean speed $\bar{v} = a\sqrt{\pi/2}$. We choose $V(p)$ to be the region described by (5.5) and shown in the lower panel of Fig. 5.3. We note that any choice of the shape of $V(p)$ is allowed. The shape $V(p)$ used here is adapted to the search for objects which move in straight lines at constant speed. For sources with different patterns of motion, other choices for $V(p)$ may be more appropriate. However, because the choice affects the counting of pairs of events when measuring ξ it must be taken into account in the theoretical derivation of ξ.

With these choices the integral in (5.14) becomes

$$\begin{aligned}\int_{V(p)} P_{\rm v}(v)\, dv\, dt\, \frac{d\phi}{2\pi} &= \int_{t_1}^{t_2}\int_{v_1}^{v_2}\int_{0}^{2\pi} \frac{v}{a^2} e^{-v^2/2a^2}\, dv\, dt\, \frac{d\phi}{2\pi} \\ &= (t_2 - t_1)\left[e^{-v_1^2/2a^2} - e^{-v_2^2/2a^2}\right].\end{aligned}$$

Inserting this expression into (5.14) and using (5.6) we find

$$\xi(v_1, v_2;\, t_1, t_2) = \frac{\rho_1 \lambda\, (t_2 - t_1)\left[e^{-v_1^2/2a^2} - e^{-v_2^2/2a^2}\right]}{(\pi/3)(\rho_1 + \rho_0)^2\, (v_2^2 - v_1^2)(t_2^3 - t_1^3)}. \tag{5.20}$$

Given an event map we can measure $\xi(v_1, v_2;\, t_1, t_2)$ for any choice of the 4 parameters (v_1, v_2, t_1, t_2). In practice, a fit can be attempted in order to discover the 4 physical parameters λ, ρ_1, ρ_0, and a. While $\rho = \rho_1 + \rho_0$ is measured directly the parameters ρ_1 and λ are combined as a single normalization factor and so the most a fitting analysis would reveal would be the combination $\rho_1\lambda$. In the 2-dimensional case this is true for any choice of $V(p)$, as can be seen from (5.14). Of course,

knowledge of any one of λ, ρ_1, or ρ_0 can be used to find the other two.

Our first simulation will only contain moving objects. In the second we will add a component of random noise and in the third simulation both random noise and a population of stationary objects will be considered in addition to the moving objects. One of the goals of these simulations is to demonstrate that the 2-point function can tell the difference between a background containing a population of sources and a completely random background. We do this by generating a second sky map for each example with the same number of events but distributed completely randomly throughout the spacetime volume. The 2-point function is measured for this randomly generated sky map and is plotted along with the 2-point function measured from the actual simulation. If the events are randomly generated there should be no correlations at all: $\xi(v_1, v_2; t_1, t_2)$ should be 0 for all values of v_1, v_2, t_1, and t_2.

5.7.1 Example 1: Moving sources only

In the first simulation there is no random noise: $\rho_0 = 0$. We simulate an area with dimensions 13,200 $\times$ 13,200 for time 10. The density of objects is $n = 0.2$ and each has an event rate $\lambda = 0.01$ yielding an estimated flux of $\rho_1 = n\lambda = 0.002$ events per unit area per unit time. Their speeds are distributed according to a Rayleigh distribution with a mean speed $\bar{v} = 5$. The objects then have the same density, event rate, and speeds as in the lower left image of Fig. 5.1. The expected number of events triggered by each object is 0.1 which means that although there are about 35 million objects present, less than 10% of them will trigger even a single event. Overall, there are roughly 3.5 million events in our sky map.

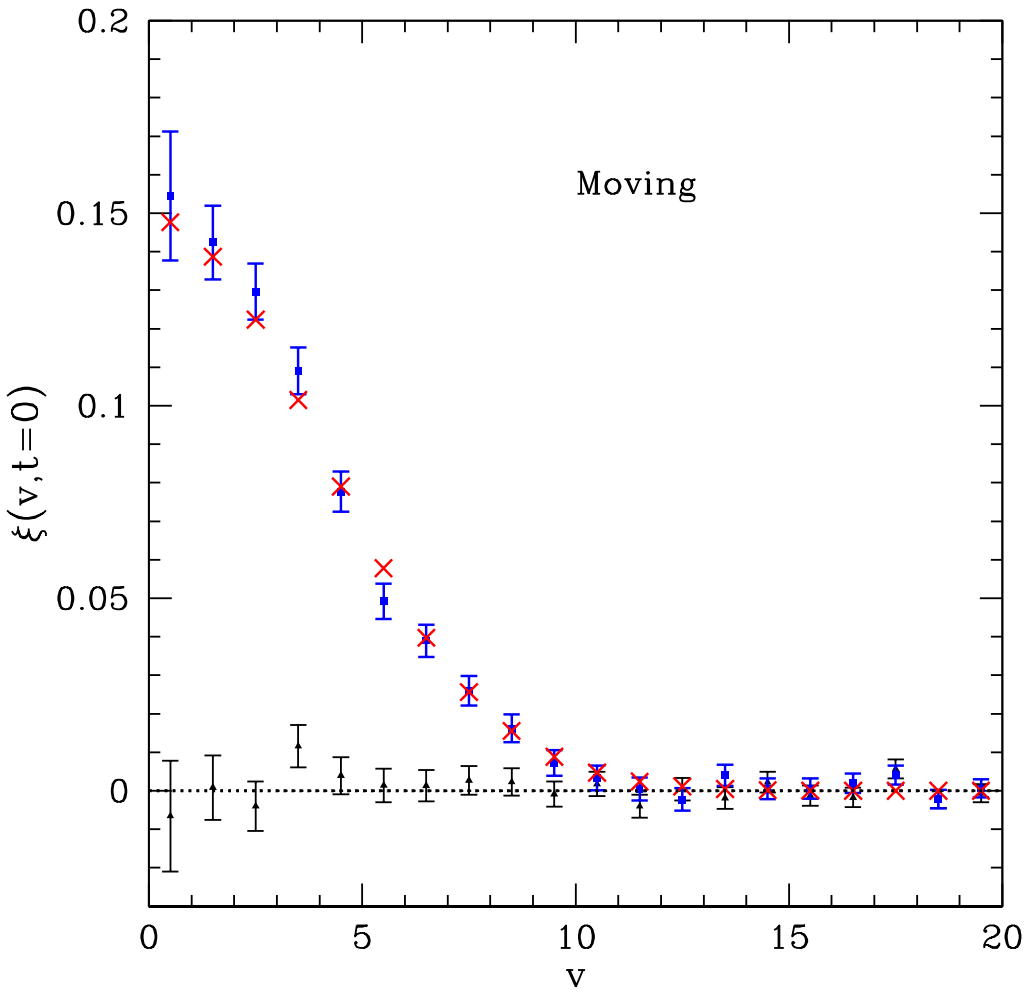

Figure 5.4: A toy example demonstrating the use of the spacetime correlation function to discover the presence of localized event sources with non-zero speeds. The $t = 0$ slice of $\xi(v, t)$ is plotted showing the theoretical prediction (red $\times$'s), the measured value (blue squares), and the measured value for the case of completely random events (black triangles). The hypothesis that the pattern of events in the sky map is Poisson ($\xi(v, t) = 0$) is clearly rejected at high significance. The error bars in the measured quantities are explained in the discussion surrounding (5.16). The sky map contained 3.5 million events, all from moving objects, though each object contributed only 0.1 events on average. The blue data points are measured from a larger version of the map shown in the lower left panel of Fig. 5.1 while the black points are measured from a larger version of the map shown in the right panel.

In the measurement of $\xi(v_1, v_2; t_1, t_2)$ we take $v_2 = v_1 + 1$ and $t_2 = t_1 + 1$, i.e. we choose non-overlapping bins of size 1 in both time and velocity separation. The subscripts on v_1 and t_1 are dropped and $\xi(v_1, v_2; t_1, t_2)$ is relabeled $\xi(v, t)$. The 2-point function is then measured for $v = 0, \ldots, 19$ and for $t = 0, 1, 2$. The $t = 0$ slice of the measured $\xi(v, t)$ is shown in blue in Fig. 5.4 along with the theoretical value (5.20), shown in red. The black curve is the 2-point function measured for a sky map containing the same number of events but placed randomly. The separation $v_2 - v_1 = 1$ was selected for illustrative purposes. The time separation $t_2 - t_1 = 1$ was then chosen to be close to the optimal separation found by maximizing the signal to noise ratio (5.17) for $t_1 = 0$. The error bars are computed according to (5.16). This is a slight abuse since the estimator plotted is DD/RR and not $(DD - 2DR + RR)/RR$. In practice it is recommended to use the latter estimator.

It is clear that moving objects are detected at a very high significance (i.e. the hypothesis $\xi(v, t) = 0$ is rejected). The measured value $\xi(0, 0) = 0.15$, for example, is about 15 standard deviations from $\xi = 0$. A fit to recover the parameters λ, ρ_1, and a can be attempted using $\xi(v, t)$, which is measured at the lattice of points $\{(v, t) : v = 0, 1, \ldots; t = 0, 1, \ldots\}$. In practice, the full covariance matrix of errors between different v-bins should be included in such a fit (see last paragraph in Sec. 5.5).

5.7.2 Example 2: Moving sources and a random component

Let us see if the spacetime 2-point function can tell the difference between a collection of moving objects plus random noise and a situation with just random noise, where both cases have the same total flux ρ. The sky map has the same dimensions as before and the moving objects have the same number density, luminosity, and speed distribution as before yielding $\rho_1 = 0.002$. We choose the random component to

have the same flux $\rho_0 = \rho_1$ so that $\rho = \rho_0 + \rho_1 = 0.004$. There are about 7 million events in this sky map, half coming from objects and the other half coming from the random component.

In the calculation of $\xi(v_1, v_2; t_1, t_2)$ we choose $v_2 = v_1 + 1$ and $t_2 = t_1 + 0.9$. The results are plotted in the top panel of Fig. 5.5. Again it is clear that the moving objects are detected even in the presence of random signal in the sky map.

How impressive is this result? Could we have just looked at the data by eye and spotted the presence of moving objects? If each object generates at most a single event then clearly it is impossible to determine anything about their motion or to distinguish this from the case of completely random events. The fraction of events which come from objects that trigger more than one event is

$$\begin{aligned} \mathrm{P}_{>1} &= \frac{nA \sum_{k=2}^{\infty} k\ \pi(k; \lambda T)}{(\rho_1 + \rho_0)AT} \\ &= \frac{nA\ \ \lambda T(1 - e^{-\lambda T})}{(\rho_1 + \rho_0)AT} \\ &= \frac{\rho_1}{\rho_1 + \rho_0}(1 - e^{-\lambda T}), \end{aligned} \tag{5.21}$$

where A total area of the sky map, T is the observation time, and $\pi(i; M) \equiv e^{-M} M^i / i!$ is the Poisson distribution with mean M. In our case, $\rho_1 = \rho_0 = 0.002$, $\lambda = 0.01$, and $T = 10$. Substituting these values into (5.21) gives $\mathrm{P}_{>1} = 0.048$. That is, less than 5% of the events in our simulated sky map come from objects which generate more than one event. Furthermore, 95% of these events come from objects which generate exactly two events during the time T. If one was to try to spot individual moving objects in the sky map one would need to be able to take 200 events and out of the nearly 20,000 possible pairs of these events spot the 5 pairs which correspond to an object triggering an event, moving, and triggering a second

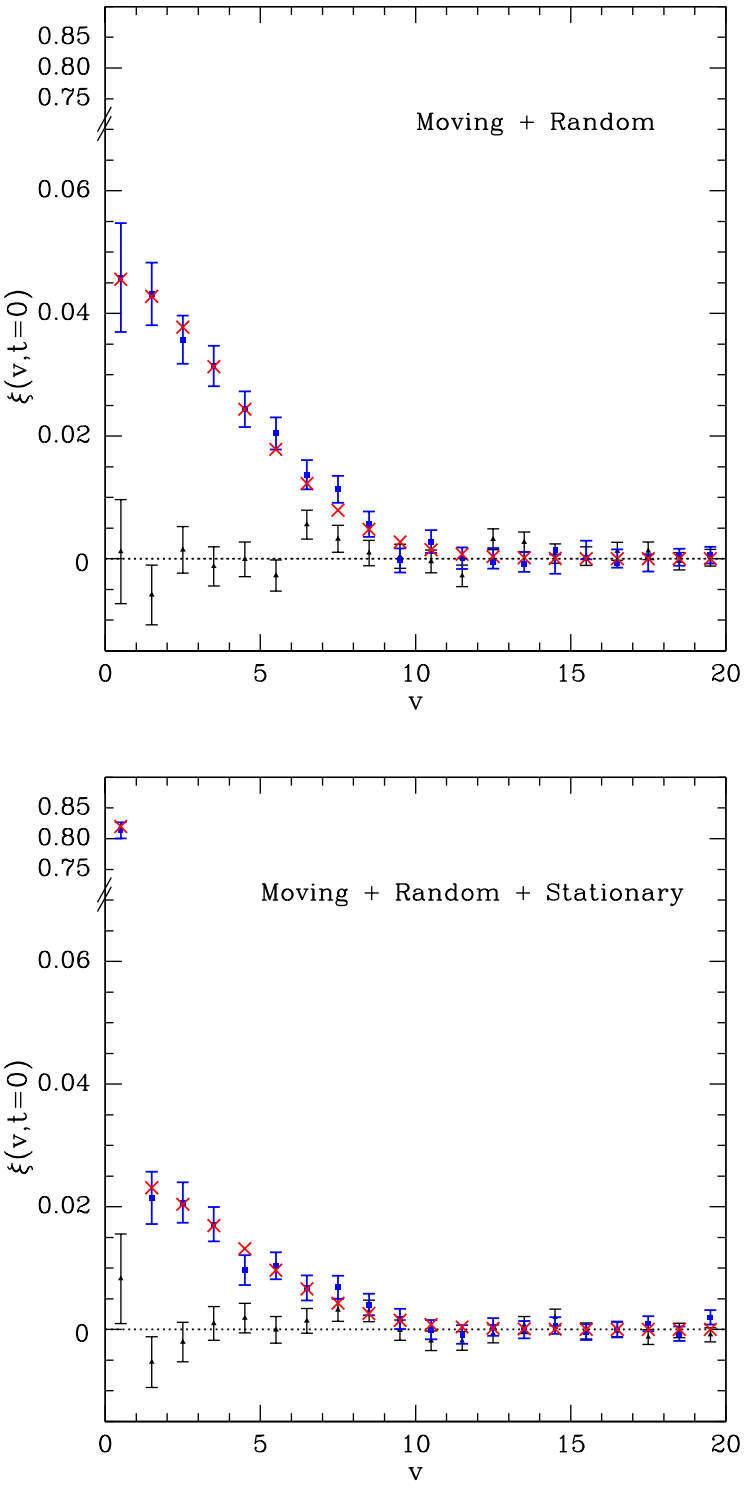

Figure 5.5: The 2-point function ξ measured for two simulations color-coded as in Fig. 5.4. Each contained 7 million events. Objects had the same event rate as the first simulation. *Top:* Moving sources and random noise. Half the events came from moving objects and half were generated completely randomly to represent noise. *Bottom:* Moving sources, stationary sources and random noise. A third of the events are from moving objects, a third from stationary objects, and the last third were generated randomly.

event.

We can illustrate this difficulty by examining a small area of the sky map from our simulation. The top panel of Fig. 5.6 shows all the events that occurred in a 150×150 area during the entire 10 units of time. On the bottom the same events are shown but are identified as having come from objects (blue) or as random events (orange). Events which came from the same object are connected with a line. The difficulty of discovering moving objects by eye is evident. The 2-point function is statistically able to pick up on the rare occurrences where an object generates more than one event.

5.7.3 Example 3: Moving sources, fixed sources, and a random component

As a final example, a third class of objects are added to the simulation. These are stationary objects which do not move during the course of the observation. The presence of such objects should manifest itself as a spike in the 2-point function at $v = 0$.

The dimensions of the sky map are the same as in the two previous examples. The moving and stationary objects have the same event rate, $\lambda = 0.01$, and spatial density, $n \approx 0.133$. The moving objects have the same velocity distribution as before. The random component has spacetime density $\rho_0 \approx 0.00133$. Therefore, the total density of events is $\rho = \rho_0 + \rho_1 + \rho_2 = 0.004$, which is the same as in the last example. The subscript 2 denotes the stationary objects. Each component contributes roughly the same number of events to the sky map.

Including the stationary objects into the 2-point function just requires replacing the Rayleigh distribution with the Dirac delta function centered at $v = 0$: $P_{\rm v}(v) = \delta(v)$. Eq. 5.20 becomes,

$$\xi_2(v_1, v_2;\, t_1, t_2) = \frac{3\,\rho_2 \lambda\,(t_2 - t_1)\delta_{v_1,0}}{\pi\,\rho^2\,(v_2^2 - v_1^2)(t_2^3 - t_1^3)}, \tag{5.22}$$

and $\xi_1(v_1, v_2;\, t_1, t_2)$ is given by (5.20) except that the total density in the denominator includes the stationary objects, $\rho = \rho_0 + \rho_1 + \rho_2$. The function $\delta_{v_1,0}$ is 0 if $v_1 > 0$ and is 1 if $v_1 = 0$. The measured 2-point function $\xi(v_1, v_2;\, t_1, t_2)$ is simply the sum of the 2-point functions for each class of objects: $\xi = \xi_1 + \xi_2$.

As before we choose $v_2 = v_1 + 1$ and $t_2 = t_1 + 1$. The results are plotted in the lower panel of Fig. 5.5. The spike at $v = 0$ due to the stationary objects is apparent. Its height is determined by both ξ_1 and ξ_2. Since the shape of ξ when $v > 0$ can be measured the contribution of the moving objects to the spike at $v = 0$ can be subtracted.

5.8 Objects in 3 dimensions

The 2-dimensional situations examined so far are, of course, only toy models for astrophysical applications. In this section we develop a more realistic theory of the use of the 2-point function. The derivation of the form of ξ is based on precisely the same arguments as in the 2-dimensional case. Simulations analogous to those in the previous section can also be performed in three dimensions and will agree with the theoretical form of ξ. In performing an actual measurement of ξ simulations should be tailored to the specific application. We defer such detailed modeling to future

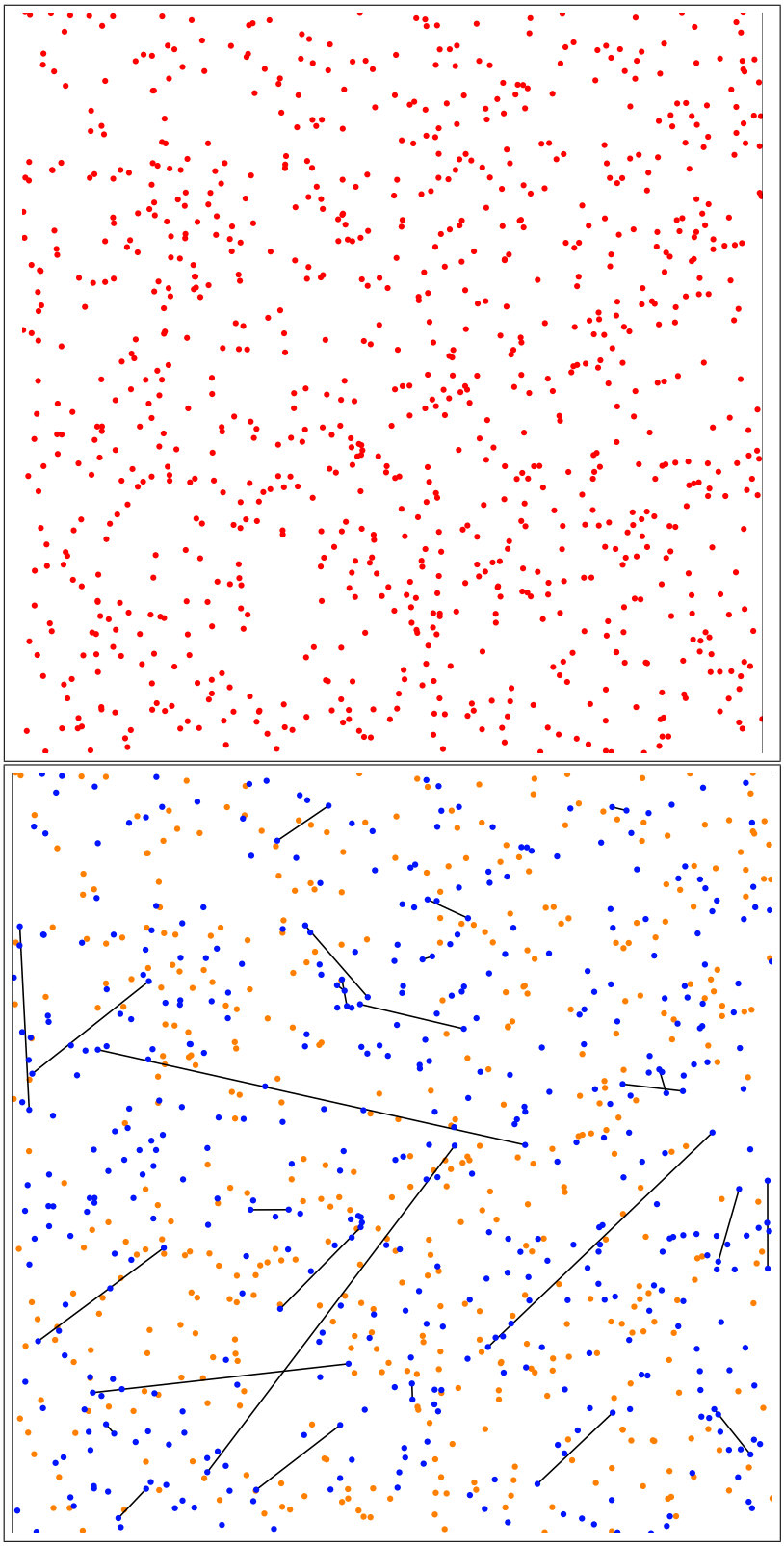

Figure 5.6: *Top*: All events which occured in an area of the sky map with dimensions 150 × 150 during the entire observation time. *Bottom*: The same events but identified as objects (blue) and random events (orange). Events which came from the same object are connected with a line. Less than 5% of events come from objects which caused more than one event.

work wherein we will apply the formalism to all-sky gamma-ray data [275].

A diffuse emission all-sky map (e.g. from Fermi-LAT) is a 3-dimensional representation of a 4-dimensional process since we cannot measure line-of-sight distances for individual events. The distance to a source determines both its flux on Earth and its angular speed across the sky. This coupling between distance, speed, and flux is what makes the analysis more complicated. Previously, the velocity distribution $P_{\mathrm{v}}(v)$ and the luminosity λ were independent quantities. Now we must consider probability distributions which depend on both v and λ: closer objects have higher angular speeds *and* look brighter than distant objects. While the spacetime 2-point function in this situation is still defined by (5.2) it is more difficult to derive the analogue of (5.14). The analysis of this section will develop the theory of the spacetime 2-point function in the case of a realistic sky survey.

5.8.1 Summary of the measurement of ξ

The computation of ξ proceeds exactly as in the 2-dimensional case. The sky map consists of events, each having a directional coordinate (the apparent direction of the photon's origin) and a time coordinate. The "distance" between events is the angle between them measured along a great circle. The velocity of interest is now an angular velocity: the "velocity separation" of two events is defined as the angle between the two events divided by their time separation. The sky map is again a spacetime diagram, though not with the usual rectangular coordinates for the spatial axes. It can be visualized as a series of concentric spheres, each representing the celestial sphere, with different spheres corresponding to different slices of time (with t increasing as the radius of the spheres increases). In this picture the worldlines of objects moving at constant angular speed are Archimedean spirals in spacetime.

The volume of a region in this spacetime has units of solid angle $\times$ time.

In the next sections we derive expressions for $V(p)$ and $C(p;V)$, the latter in terms of parameters describing the various populations of objects which contribute to the sky map.

5.8.2 The form of $V(p)$ in 3 dimensions

One defines $V(p)$ as some volume of spacetime $\mathcal{S}$. Convenient choices include

$$\begin{aligned} V(\theta_1,\theta_2;t_1,t_2)(p) &= \{p' \in \mathcal{S} : t_1 \leq p'(t) - p(t) < t_2 \\ &\quad \wedge\, \theta_1 \leq d(p',p) < \theta_2\}, \end{aligned} \tag{5.23}$$

where $p(t)$ is the time coordinate of the event p and $d(p',p)$ is the angle between spacetime points p and p', and

$$\begin{aligned} V(\omega_1,\omega_2;t_1,t_2)(p) &= \{p' \in \mathcal{S} : t_1 \leq p'(t) - p(t) < t_2 \\ &\quad \wedge\, \omega_1 \leq \frac{d(p',p)}{|p'(t) - p(t)|} < \omega_2\}, \end{aligned} \tag{5.24}$$

where ω_1 and ω_2 are angular speeds. These are the analogues of Eqs. 5.3 & 5.5. In (5.23), $V(p)$ contains the events which occur in an annulus around p with inner and outer radii θ_1 and θ_2 and which occur in the time interval $p(t)+t_1$ to $p(t)+t_2$. Note that when $t_1 = 0$ and $t_2 = \infty$ this region is *exactly* that used for galaxy-galaxy correlation studies. In (5.24), $V(p)$ represents all the events which could have been triggered by an object moving from p if it had an angular speed between ω_1 and ω_2

and with the same time separation constraint.

If we are looking at a small area of the celestial sphere that can be approximated as flat space then we can choose $V(p)$ to be "anisotropic". i.e. choose volumes such as

$$\begin{aligned} V(v_{x1}, v_{x2};\, v_{y1}, v_{y2};\, t_1, t_2) \;=\; & \{p' \in \mathcal{S} : \\ & t_1 \le p'(t) - p(t) < t_2, \\ & \wedge\, v_{x1} \le \frac{p'(x) - p(x)}{p'(t) - p(t)} < v_{x2}, \\ & \wedge\, v_{y1} \le \frac{p'(y) - p(y)}{p'(t) - p(t)} < v_{y2}\}. \end{aligned} \tag{5.25}$$

This choice of $V(p)$ is useful when a class of moving objects has an anisotropic velocity distribution, or when the proper motion of the earth or the detector is important.

The volume of the region $V(p)$ is calculated in a way similar to the 2-dimensional case. For instance, the volume of the region specified by (5.23) is found by first computing the solid angle of the annulus between θ_1 and θ_2, and multiplying this by the time interval:

$$V(\theta_1, \theta_2;\, t_1, t_2) = 2\pi\,(\cos\theta_1 - \cos\theta_2)\,(t_2 - t_1). \tag{5.26}$$

The volume specified in (5.24) is slightly more complicated:

$$
\begin{aligned}
V(\omega_1,\omega_2;t_1,t_2) &= \int_{t_1}^{t_2} dt \int_0^{2\pi} d\phi \int_{\omega_1 t}^{\omega_2 t} \sin\theta \, d\theta \\
&= 2\pi \left[\frac{\sin(\omega_1 t_2) - \sin(\omega_1 t_1)}{\omega_1} \right] \\
&- 2\pi \left[\frac{\sin(\omega_2 t_2) - \sin(\omega_2 t_1)}{\omega_2} \right]. \qquad (5.27)
\end{aligned}
$$

Equations 5.26 and 5.27 hold only when $\theta_2 < \pi$ and $\omega_2 t_2 < \pi$, respectively. Otherwise the annulus begins to overlap itself. This is only an issue if one is searching for objects which moved across the entire sky during the observation period.

In the limit where $t_2 \to t_1 + dt$ and $\omega_2 \to \omega_1 + d\omega$ (5.27) becomes (dropping subscripts)

$$V(\omega_1,\omega_2;\, t_1,t_2) \to dV(\omega,t) = 2\pi t \sin(\omega t)\, d\omega\, dt. \qquad (5.28)$$

This is the analogue of the 2-dimensional (5.8).

As in the 2-dimensional case we now define a convenient coordinate system for every point on the celestial sphere. The coordinates $(\omega,\phi,t)_p$ are related to the global celestial coordinates (plus time) as follows. First we consider a rotated set of spherical coordinates $(\Theta,\Phi)_p$ in which p is at the north pole and the line $\Phi = 0$ intersects the north celestial pole. That is, the new and old coordinates are related by a rotation in which p slides along a line of longitude to the north celestial pole. Then new coordinates $(\omega,\phi,t)_p$ are related to (Θ,Φ) by $\Theta = \omega t$ and $\Phi = \phi$. This is a mapping from $(\omega,\phi,t)_p$ to the global celestial coordinates (the time coordinate is unchanged). Using (5.28) we can write down the volume element in these coordinates. The spacetime volume (solid angle $\times$ time) between ω and $\omega + d\omega$, between ϕ and

$\phi + d\phi$, and between t and $t + dt$ is

$$dV_p(\omega, \phi, t) = t \sin(\omega t)\, d\omega\, d\phi\, dt, \tag{5.29}$$

and one can check that (5.27) is recovered as the integral

$$\int_{\omega_1}^{\omega_2} \int_{0}^{2\pi} \int_{t_1}^{t_2} dV_p(\omega, \phi, t).$$

5.8.3 Ingredients needed to derive $C(p; V)$ in 3-D

Besides the volume $V(p)$ we need to derive an expression for $C(p; V)$ in (5.2). This quantity depends on the properties of the sources which contribute events to the sky map. Generally, the sky is populated by different classes of objects, each with its own velocity distribution, luminosity function, and spatial distribution. Let's denote the different classes of objects by the subscript i. Then for each class we define the following functions.

- $P_{i,L}(L)\, dL$ is the probability that an object of class i has an intrinsic luminosity between L and $L + dL$. L is the number of photons per second emitted by the object. The distribution $P_{i,L}(L)$ is normalized to 1: $\int_0^\infty P_{i,L}(L) dL = 1$. The function $P_{i,L}$ is commonly called the luminosity function of the population.

- $n_i(R, \hat{\Omega})$ is the physical number density of i-type objects which lie a distance R away from the detector in the direction $\hat{\Omega}$ on the celestial sphere. This quantity has units [length]$^{-3}$.

- $f_i(\vec{v}; \hat{\Omega})$ specifies the tangential velocity distribution of i-type objects. The quantity $f_i(\vec{v}; \hat{\Omega}) d^2\vec{v}$ is the probability than an object of class i located in the

direction $\hat{\Omega}$ on the celestial sphere has its tangential velocity vector in the range $d^2\vec{v}$ around $\vec{v}$. These velocities are proper velocities, measured relative to the earth (or the detector). "Tangential" means that the velocity is perpendicular to the line of sight[8]. This distribution is also normalized to 1.

- ρ, defined above, is the average number of events detected per solid angle per time. It can be estimated from the sky map by dividing the total number of events by the time over which the sky map was measured and by the total solid angle of the map. For maps with large numbers of counts this estimator will be adequate. In practice, one may need to modify the procedure for surveys with unequal exposures across the sky: the quantity ρ may be position and time-dependent. If we divide ρ by the detector area A we get $\tilde{\rho}$, the total flux per solid angle.

5.8.4 Derivation of $C(p;V)$ in 3 dimensions

The quantity $C(p;V)$ is the probability of finding an event in the region $V(p)$ given that the detector reported the event p. It can also be thought of as the expected number of events in $V(p)$, given an event p. First we break $C(p;V)$ into the sum of 2 terms: $C(p;V)$ = [the probability that the event p was caused by an object which moved into the region $V(p)$ and triggered another event] + [the probability of finding an event in $V(p)$ for any other reason]. As in the 2-dimensional case the second term is simply $\rho V(p)$.

The first term can be broken up into the product of 3 probabilities: [C_1: the

[8]We have implicitly assumed that the line of sight velocity of any object is small enough that the change in its distance does not affect its flux. That is, the objects are all far enough away so that $\bar{v}_{\rm los}\bar{t}/R \ll 1$, where $\bar{t}$ is a measure of the time separation between the region $V(p)$ and the event p.

probability that the event p came from an object of class i with luminosity L located a distance R from the detector] $\times$ [C_2: the probability that this object has a velocity that takes it into the region $V(p)$] $\times$ [C_3: the probability it triggers an event while in $V(p)$]. The product then needs to be integrated over R and L and summed over i.

The first factor, C_1, is the ratio of photons received from i-type objects with luminosity L and distance R in the direction $\hat{\Omega}_p$ to the total number of photons received from the same direction:

$$C_1 = \frac{1}{\rho}\left[n_i(R,\hat{\Omega}_p)R^2\,dR\right]\left[P_{i,L}(L)\,dL\right]\left[\frac{L\,A}{4\pi R^2}\right], \tag{5.30}$$

where A is the effective area of the detector. It is worth noting that C_1 does not actually depend on A since ρ will also be proportional to A.

The second factor, C_2, is the probability that an i-type object will have a velocity which takes it into the region $V(p)$. We will have to integrate over a range of velocities which correspond to the object moving into $V(p)$. It will, therefore, be useful to use the coordinate system defined in the discussion leading to (5.29). We can adapt the velocity distribution $f_i(\vec{v};\,\hat{\Omega})$ to the new coordinates by introducing the function $f_i(v,\phi;\,\hat{\Omega})$ defined so that

$$f_i(v,\phi;\,\hat{\Omega})\,dv\,d\phi = f_i(\vec{v};\,\hat{\Omega})d^2\vec{v}. \tag{5.31}$$

The quantity $f_i(v,\phi;\,\hat{\Omega})\,dv\,d\phi$ is to be interpreted as the probability that an object of type i has tangential speed between v and $v+dv$ and is moving in a direction between ϕ and $\phi+d\phi$, where ϕ refers to the coordinate label in our new coordinate system whose north pole coincides with the direction $\hat{\Omega}$ as described previously. Next

we relate the distance to the object to its angular velocity using the relation $v = R\omega$. Therefore, the quantity

$$f_i(R\omega, \phi;\, \hat{\Omega})\, R\, d\omega\, d\phi \tag{5.32}$$

gives the probability that the object, which is at a distance R, has angular speed between ω and $\omega + d\omega$ and is moving in a direction between ϕ and $\phi + d\phi$. This expression is adapted for use with our new coordinate system.

The third factor, C_3, is the probability that the object triggers another event. This is simply given by

$$C_3 = \frac{L\, A\, dt}{4\pi R^2}. \tag{5.33}$$

Combining this with (5.32) and integrating over $V(p)$ yields the quantity $C_2 \times C_3$:

$$C_2 \times C_3 = \int\limits_{V(p)} f_i(R\omega, \phi;\, \hat{\Omega}_p)\, R \frac{L\, A}{4\pi R^2} d\omega\, d\phi\, dt, \tag{5.34}$$

which illustrates the benefits of our choice of coordinates $(\omega, \phi, t)_p$. In words, $C_2 \times C_3$ is the probability that an i-type object with luminosity L, distance R, and starting at the location $\hat{\Omega}_p$, moves into the region $V(p)$ and triggers an event.

Now we can put together all the factors which make up $C(p;V)$ to find

$$\begin{aligned} C(p;V) &= \rho V(p) + \sum_i \int_{L=0}^{\infty} \int_{R=0}^{\infty} C_1 \times C_2 \times C_3 \\ &= \rho V(p) + \left(\frac{A}{4\pi}\right)^2 \frac{1}{\rho} \\ &\times \sum_i \int_{L=0}^{\infty} \int_{R=0}^{\infty} \int_{V(p)} \frac{n_i(R,\hat{\Omega}_p)}{R} \\ &\times P_{i,L}(L)\, L^2\, f_i(R\omega,\phi;\,\hat{\Omega}_p)\, d\omega\, d\phi\, dt dL\, dR. \end{aligned} \tag{5.35}$$

In practice, since resolved objects will be removed from the sky map, the lower limit of the R integral should be cut off so that these objects are not counted. If the detector can resolve any source with flux greater than $F_{\rm res}$ then the lower limit on the R integral should be $\sqrt{L/4\pi F_{\rm res}}$.

Of course, if $n_i(R,\hat{\Omega})$ is cut off at a lower limit $R_{\rm min}$ and $P_{i,L}(L)$ is cut off at an upper limit $L_{\rm max}$ such that $(L_{\rm max}/4\pi R_{\rm min}^2) < F_{\rm res}$ no changes need to be made to the limits of integration in (5.35) since all i-type objects will be unresolved.

5.8.5 The form of ξ in 3 dimensions

Finally, we can substitute (5.35) into the definition of the 2-point function ξ (5.2) and arrive at an expression for the 2-point spacetime correlation function in 3 dimensions,

$$\begin{aligned}\xi &= \left(\frac{1}{4\pi\tilde{\rho}}\right)^2 \sum_p \sum_i \int_{L=0}^{\infty} \int_{R=\sqrt{L/4\pi F_{\rm res}}}^{\infty} \int_{V(p)} \frac{n_i(R,\hat{\Omega}_p)}{R} \\ &\times P_{i,L}(L)\; L^2 f_i(R\omega,\phi;\,\hat{\Omega}_p)\, d\omega\, d\phi\, dt \\ &\times \left[\sum_p V(p)\right]^{-1}. \end{aligned} \tag{5.36}$$

Notice that the detector area A has cancelled when using $\tilde{\rho}$, the average flux per solid angle, instead of ρ. It is also apparent that the contribution to the ξ from different classes of objects as well as from objects of different distances and luminosities is additive. The observed 2-point function is simply the sum of contributions from different types of objects. As expected, the correlation is increased for brighter-appearing objects as is seen by the presence of L^2 and R^{-1}. The interplay between distance and angular speed appears in the argument of the velocity distribution f_i.

The expression for ξ given by (5.36) is a main result of this paper. In its general form, however, it is fairly opaque. We can get a qualitative feel for the 2-point function by calculating ξ for a very simple model where we have only one class of objects. These objects have a constant number density n and are found only at distances between R_1 and R_2. The intrinsic luminosity of all the objects will be fixed at λ so that $P_{i,L}(L) = \delta(L-\lambda)$. We choose an isotropic Maxwell-Boltzmann velocity distribution. Projected into 2 dimensions it becomes the Rayleigh distribution:

$$f(v,\phi;\hat{\Omega})\, dv\, d\phi = \frac{v}{a^2} e^{-v^2/2a^2} dv \frac{d\phi}{2\pi}, \tag{5.37}$$

independent of $\hat{\Omega}$. Finally we choose $V(p)$ to be given by (5.24) in which ϕ runs from 0 to 2π. With these choices no quantity in (5.36) depends on p so both sums over p disappear.

Let's look at the limiting form for ξ by choosing an infinitesimal volume for $V(p)$ where $\omega_2 = \omega_1 + d\omega$ and $t_2 = t_1 + dt$. Dropping the subscripts on ω_1 and t_1 we have the following expression for the 2-point function,

$$\begin{aligned}
\xi(\omega,t) &= \frac{1}{2\pi t\sin(\omega t)}\left(\frac{1}{4\pi\tilde{\rho}}\right)^2 n\lambda^2 \int_{R_1}^{R_2} \frac{dR}{R}\frac{R\omega}{a^2} e^{-(R\omega)^2/2a^2} \\
&= \frac{1}{2\pi t\sin(\omega t)}\sqrt{\frac{\pi}{2}}\left(\frac{1}{4\pi\tilde{\rho}}\right)^2 \frac{n\lambda^2}{a} \\
&\times \left[\mathrm{Erf}\left(\frac{R_2\omega}{\sqrt{2}a}\right) - \mathrm{Erf}\left(\frac{R_1\omega}{\sqrt{2}a}\right)\right].
\end{aligned} \tag{5.38}$$

Note that the contribution to $\xi(\omega,t)$ from objects at different distances serves to smear the influence of $f(v)$ so that ξ is not simply proportional to the velocity distribution as it was in the 2-dimensional model. There is, however, a functional similarity to the 2-dimensinal case:

$$\begin{aligned}
\xi_{3\mathrm{D}} &\sim \frac{1}{V(p)}\frac{n\lambda^2}{\tilde{\rho}^2} f(R\omega) \\
\xi_{2\mathrm{D}} &\sim \frac{1}{V(p)}\frac{n\lambda^2}{\rho^2} P_{\mathrm{v}}, \ (\text{using } \rho_1 = n\lambda \text{ in Eq. 5.15})
\end{aligned} \tag{5.39}$$

where $f(R\omega)$ represents the smeared velocity distribution.

5.8.6 Mock Fermi search for solar system bodies

In order to verify the formulation of ξ in (5.36) we simulate a mock 5-year Fermi observation of nearby moving gamma-ray sources. These objects might correspond to a population of bodies in the asteroid belt (see Sec. 5.10 for motivation).

For simplicity, the detector is a stationary observer at the center of the solar system and the moving objects are placed on circular orbits with Keplerian velocities determined by their distance from the Sun ($v \propto R^{-1/2}$). The objects are distributed uniformly in a disk with uniform surface density between distances of 0.95 AU and 1.5 AU. For geometric simplicity, the inclination angles of the orbits are random so that the flux is statistically isotropic. Each object has the same luminosity and the closest object (at 0.95 AU) has a photon flux of $1.8 \times 10^{-10}\text{cm}^{-2}\text{s}^{-1}$. Note that this flux is below the point source detection limit of Fermi so that none of these moving objects would be individually identified as localized sources[9]. The sky contains 7371 objects so that, for a 5 year Fermi observation (effective area $\sim 2000\,\text{cm}^2$), the population of moving objects contributes roughly 2.5×10^5 events to the sky map. In addition, as in the 2-dimensional simulation, we include a population of stationary objects as well as completely random events. The stationary sources generate detected events at an average rate of 0.2 events per year and are distributed isotropically. The stationary and random components each comprise about 1.25×10^5 events so that the sky map contains about 5×10^5 events, 50% from moving objects, 25% from stationary sources, and 25% random events.

In computing the correlation function we use spacetime volumes $V(p)$ given by (5.24) with $t_1 = 0$ and $\Delta T = t_2 - t_1 = 0.015$ yr (~ 5.5 days). The angular velocity

[9] In fact, moving sources will be more difficult to detect than stationary ones because of their apparent motion, i.e. standard point source analysis may be inefficient at detecting moving sources.

bins run from 0 to 500°/yr in steps of 20°/yr. Results of the measurement of ξ for the different angular velocities are shown with blue squares in Fig. 5.7. As with the 2-dimensional simulations, the error bars are found using (5.16). The presence of both the stationary and moving sources can be easily seen in the shape of the correlation function.

The theoretical value of ξ based on the properties of the sources is a straightforward application of (5.36). The number density of moving objects is

$$n(R) = \begin{cases} N_{\rm objs}/[2\pi R(R_2^2 - R_1^2)] & R_1 < R < R_2 \\ 0 & \text{otherwise.} \end{cases} \tag{5.40}$$

Here, $R_1 = 0.95$ AU, $R_2 = 1.5$ AU, and $N_{\rm objs} = 7371$. The luminosity function and the velocity distribution are delta functions:

$$P_L(L) = \delta\left(L - 4.45 \times 10^{17}\,\mathrm{sec}^{-1}\right) \tag{5.41}$$

$$f(v,\phi) = \frac{1}{2\pi}\,\delta\left(v - v_0(R/R_0)^{-1/2}\right). \tag{5.42}$$

In the above, $R_0 = 1$ AU and $v_0 = 2\pi R_0/\mathrm{yr} \equiv \omega_0 R_0$. The average event rate ρ is estimated by dividing the total number of events by the solid angle of the sky map and by the observation time: $\rho = 5 \times 10^5/(4\pi \times 5\mathrm{yr})$. Carrying through the calculation of (5.36) yields ξ for the particular choice of $V(p)$:

$$\begin{aligned} \xi(\omega_1,\omega_2;\Delta T) &= \frac{\Delta T}{4\pi\rho^2 V(\omega_1,\omega_2;\Delta T)}\left(\frac{LA}{4\pi R_0^2}\right)^2 \\ &\times \frac{N_{\rm objs}}{R_2^2 - R_1^2}\left(\frac{1}{R_a^2} - \frac{1}{R_b^2}\right). \end{aligned} \tag{5.43}$$

The quantity $V(\omega_1,\omega_2;\Delta T)$ is the volume of the spacetime region given in (5.27), $R_a = \mathrm{Max}(R_1, R_0(\omega_0/\omega_2)^{2/3})$, $R_b = \mathrm{Min}(R_2, R_0(\omega_0/\omega_1)^{2/3})$, and $\xi = 0$ if $R_a > R_b$.

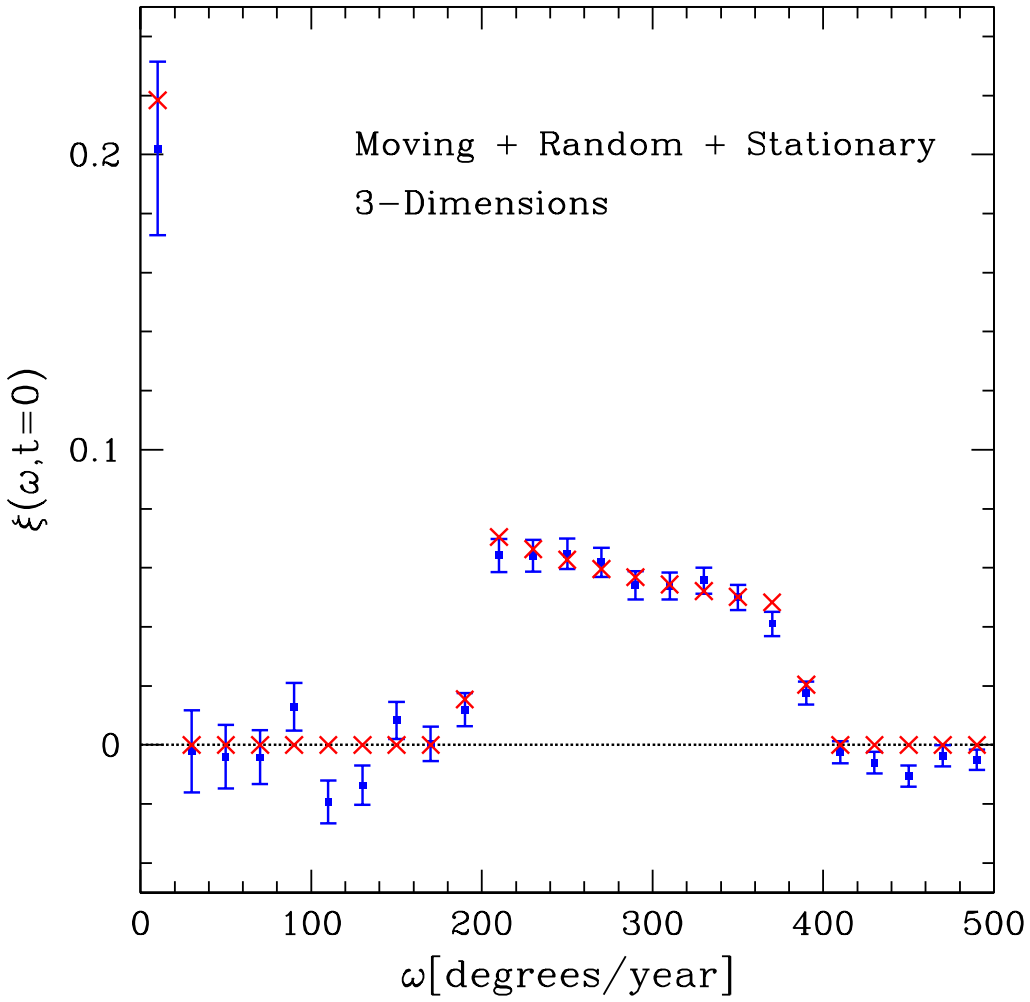

Figure 5.7: Results from a simulation of moving objects in the solar system, along with stationary sources and random noise. The correlation function is plotted for angular velocities between 0 and 500°/yr. Red ×'s represent the theoretical value of ξ calculated from (5.36) while the blue squares show the measured value of ξ from the sky map. The width of each angular velocity bin is 20°/yr. Error bars are derived using (5.16). The spike at zero angular velocity is due to the presence stationary background sources. The correlation function is also non-zero between $\omega = 196°$/yr and 389°/yr, corresponding to moving sources orbiting between 0.95 and 1.5 AU.

In (5.43) the quantities R_1, R_2, R_a, and R_b are in units of $R_0 = 1$ AU.

The correlation for the stationary objects is much simpler. It is equal to zero unless $\omega_1 = 0$, in which case it is given by

$$\xi(\omega_1 = 0, \omega_2; \Delta T) = \frac{\Delta T \, N_{\rm stat} \, \lambda^2}{4\pi\rho^2 V(0, \omega_2; \Delta T)}, \tag{5.44}$$

where $N_{\rm stat} = 1.25 \times 10^5$, the number of stationary objects and $\lambda = 0.2$/yr, the detected event rate for each stationary object.

The total correlation function will be the sum of the correlation functions for each component. This sum is plotted in Figure 5.7 as red $\times$'s, demonstrating that the formalism predicts the correct value for the correlation function.

Although intended as a toy model, this simulation captures the essential components of a large area analysis of Fermi data. In reality, Fermi has detected far more than 5×10^5 events. If all the components in our toy model were scaled up appropriately the detection of $\xi \neq 0$ would be even more significant.

5.8.7 Errors and flux-limited vs. counts-limited surveys

In three dimensions the errors on ξ given by Eqs. 5.16 & 5.17 also apply. As above, choosing the regions $V(p)$ requires balancing a large signal to noise ratio against having many independent choices of $V(p)$. In order to make more independent measurements of ξ the size of $V(p)$ must decrease.

A larger $V(p)$ has its advantages and disadvantages. A large volume V will decrease the fluctuations in ξ because more events are collected in each such volume

(the signal-to-noise contains a $V^{1/2}$ factor). On the other hand, having a lot of events in $V(p)$ which are uncorrelated to the event at p will dilute the amplitude of ξ because of the $\rho V(p)$ term in the denominator (c.f. the definition of ξ (5.2)). There is then a tradeoff between the fluctuations in ξ and the amplitude of ξ.

If the sky map has a large number of events then it is permissible to choose $V(p)$ to be small and still have small fluctuations in ξ. In the opposite limit, if the sky map is "counts-limited" then it will be necessary to choose $V(p)$ to have a large volume. The safest method for deciding is to run realistic simulations for various combinations of physical parameters and experiment with different choices for $V(p)$.

There is an additional requirement on $V(p)$ which depends on the detector's resolution. If one chooses $V(p)$ to be very small (in the angular sense) then one is essentially asking the detector to distinguish events at this angular scale. The detector has a smallest "pixel size" and $V(p)$ cannot be smaller than that.

The most convenient choice for $V(p)$ when calculating ξ according to (5.36) is given by (5.24). Unfortunately, this choice is inconvenient when dealing with a detector with a finite angular resolution (a real detector). The projection of the spacetime region $V(\omega_1, \omega_2; t_1, t_2)$ onto the celestial sphere must have an angular size no smaller than the detector's angular resolution. However, for fixed $\Delta\omega = \omega_2 - \omega_1$ and $\Delta t = t_2 - t_1$, changing ω_1 and t_1 will change the projected angular size of $V(p)$. The bin sizes $\Delta\omega$ and Δt must be varied with ω_1 and t_1. An estimate of this constraint is that the angular resolution of the detector be no worse than $\theta \approx \Delta(\omega t) \approx \bar{\omega}\Delta t + \Delta\omega\bar{t}$, where $\Delta\omega = \omega_2 - \omega_1$ and $\Delta t = t_2 - t_2$.

All of these choices are part of the analysis, not the collection, of the data. If the diffuse background events are already in hand one can experiment with different

choices for the $V(p)$'s to find the right balance between signal-to-noise and number of independent measurements of ξ while maintaining the detector resolution constraint.

Of course, it is best to use PSF information instead of an assumption of "pixel size". We have discussed this option for the 2-dimensional case (see (5.18)). The generalization to 3 dimensions is straightforward.

5.9 Generalizations

There are several ways to make this technique more powerful. Here we mention two: the inclusion of spectral data and the use of n-point functions.

5.9.1 Including spectral information

Not only do sky surveys keep track the direction and time of each photon they receive, they can also measure wavelength (or energy of the photon). The easiest way to make use of this information is to note that the above analysis holds for every wavelength separately. One can bin the events by energy, make separate sky maps for each energy bin, and then compute the 2-point function for each of the maps. Typically, this procedure will add more data points than free parameters: the same distributions n_i and f_i are used for different energy bins. Only the luminosity functions will vary, though the physical parameters in $P_{i,L}$ are likely to be universal over all energy bins. Thus, ξ measured at one energy will be related to ξ measured at another. As a result, an analysis which includes event energies can help in untangling the different components of the background.

5.9.2 n-point functions

Another generalization of the 2-point function is, naturally, the n-point function. One asks, "Given an event at p what is the probability of finding events in $V_1(p)$ *and* in $V_2(p)$?" If the objects move in straight lines then this probability will spike when p, $V_1(p)$, and $V_2(p)$ lie along a straight line. The jump from $n = 2$ to $n = 3$ is significant for this reason — every pair of points is collinear but not every trio. The downside of measuring n-point functions (besides the computational cost) is that they require a much larger number of events to overcome statistical fluctuations. Recall that in our 2-dimensional toy model only 5% of events came from objects which generated more than one event and that of these events, 95% came from objects which generated exactly two events. Therefore, only 0.25% of the events in the map came from objects which generated three or more events. Although they will be slightly more cumbersome, analytic forms for these higher correlation functions can be found by applying the same reasoning we used for the 2-point function.

5.10 Discussion and Conclusions

We present a new tool, based on the familiar 2-point correlation function, which can be applied to astrophysical maps of diffuse emission. The measured quantity ξ is designed to detect the presence of moving objects, each of which is too dim to be resolved individually. We derived the form of ξ based on the physical parameters which describe the classes of objects which might be present in the sky (5.36). A measurement of ξ along with the theoretical prediction for ξ can be used to find best-fit quantities for the physical parameters describing the populations of objects. We emphasize that all the technology invented to study the angular 2-point correla-

tion function can be directly applied to the generalization to the spacetime 2-point correlation function.

There are numerous applications of the derived formalism. An obvious place to start is the diffuse gamma-ray background measured by the Fermi-LAT instrument. The all-sky capabilities of LAT, coupled with its high angular resolution provide a convenient testbed where this technique can be applied. The interesting question is what kind of sources contribute to the gamma-ray background and also exhibit proper motion over the duration of observation.

One potential source is the generation of gamma-rays from cosmic-ray interactions in rocky debris present in the solar system. Cosmic ray interactions with nuclei on a solar system body lead to hadronization, and the subsequent decay of neutral pions to a photon final state [276, 277, 236, 278]. A detection of a large population of these sources is important as it provides information about the origin of the solar system and its evolution with time, as well as the energy spectrum and composition of the incident cosmic ray flux.

The detection of gamma-rays from cosmic ray interactions with solar system bodies has been discussed in the context of past measurements by the Energetic Gamma Ray Experiment Telescope (EGRET) on board the Compton Gamma-ray Observatory, and measurements with Fermi-LAT [249, 250, 279]. Sources include small objects in the main asteroid belt, Trans-Neptunian objects in the Kuiper belt, as well as objects in the Oort cloud, including icy bodies such as comets. It was shown that for objects where the cosmic ray cascade fully develops (objects with size greater than $\sim$ 1 m) it may be possible for Fermi to detect the cumulative gamma-ray emission from a collection of such bodies. These estimates are based on the distribution and composition of objects. Even though both of these quantities

are partially constrained for objects in the main asteroid belt, large uncertainties are present for the populations in the Kuiper belt and the even more speculative Oort cloud. It is conceivable that a very large number of bodies may be present in the outskirts of the solar system.

The proximity of these populations makes them ideal for an application of the spacetime correlation function, as each source will traverse an angular distance which is larger than the angular resolution limit of Fermi. Typical angular displacement (assuming Keplerian orbits) of an object at distance d from the Sun is $\theta = 2\pi\,\mathrm{rad}(\Delta T/\mathrm{yr})(d/\mathrm{AU})^{-3/2}$ during the course of an integration for time ΔT. The composition of these objects can be assumed to be similar to the composition of the Moon, though their mass density varies considerably. This similarity in composition is convenient as the gamma-ray flux due to cosmic interactions with the lunar rock is well understood [280, 248] (see also [281, 282]). If we assume that the spectral shape of the gamma-ray emission from solar system bodies is similar to that of the rim of the Moon (emission above 600 MeV is dominated by the rim of the Moon rather than the lunar disc) and we scale the flux from the object to the flux from the Moon ($\Phi_M = 1.1 \times 10^{-6}\mathrm{cm}^{-2}\mathrm{s}^{-1}$, [281]), the flux from an object of radius r at distance d would then be $\Phi = \Phi_M(r/r_M)(d_M/d)^2$. For a distance to the Moon of $d_M = 0.0024$ AU and a lunar radius of $r_M = 1740$ km, the total number of photons per year detected by the Fermi-LAT instrument (with an orbit-averaged effective area of 2000 cm^2) is $\Phi \approx 2 \times 10^{-4}\mathrm{yr}^{-1}(r/\mathrm{km})(d/1\mathrm{AU})^{-2}$. Therefore, given this information, one can apply the spacetime correlation function to determine the abundance and radial distribution of solar system objects that contribute to the gamma-ray background [275]. It is important to note that even though a theoretical estimate of ξ requires knowledge of the objects one is searching for, the measurement of ξ requires no such knowledge.

Similar arguments can be used in search of the energetic neutrino signal from cosmic ray interactions with solar system bodies. The decay of kaons to charged pions leads to an energetic signal with a spectral signature that is different from the cosmic ray neutrino flux expected from spallation of nuclei. Therefore, energetic neutrinos from cosmic ray interactions with solar system bodies should be present in the signal measured by IceCube [283]. The sources of these neutrinos will traverse an angular distance based on the distance of the source from the Sun, and therefore the spacetime correlation function derived here can be used in search of these sources. However, as in the case of gamma-rays, the uncertainties in the distribution and composition of small solar system bodies make predictions for such signal difficult. Nevertheless, a blind analysis of neutrino events from IceCube could place constraints on the parameters that describe the different populations of small bodies in the solar system.

Another application is in the search for primordial black holes in the solar neighborhood. Primordial black holes may form in the early Universe through the collapse of large primordial fluctuations [284]. Current bounds on the abundance of such black holes are of order $\Omega_{\rm PBH} \sim 10^{-9}$ for most of the range of black hole masses [252]. If primordial black holes exist in an otherwise dark matter dominated Universe, they will acquire a dark matter halo [251, 285]. Dark matter annihilation around primordial black holes and/or high density ultracompact halos will result in gamma-ray emission [286, 287]. Such objects with very small mass will in fact be very dense and survive in the Milky Way halo. If we assume that primordial black holes trace the distribution of dark matter in the Milky Way we can use their abundance to determine the angular distance that a black hole may traverse in a given time interval. For simplicity, let's assume that primordial black holes have mass $M_{\rm PBH} = 10^{-15} M_\odot$, $\Omega_{\rm PBH} = 10^{-9}$, and that the local dark matter density is 0.01 $M_\odot {\rm pc}^{-3}$. Then the mean

distance between primordial black holes in the solar neighborhood is $\sim 10^{-2}$pc. Assuming that this is the maximum distance to a primordial black hole, and that the mean velocity of primordial black holes is similar to the mean velocity of dark matter, i.e., 220 km/s, then the angular displacement of these gamma ray sources can be as large as 4.5 degrees in 10 years. As the angular resolution of Fermi is significantly less for energies greater than 1 GeV, constraints on the abundance and size of these black holes can be placed by applying the spacetime correlation function to the LAT all-sky map.

A more speculative contribution to the gamma-ray background is from dark matter halos formed on scales close to the cutoff scale of the dark matter power spectrum. These objects typically have sub-solar masses [288–294]. Even though their survival and abundance in the present-day Milky Way halo is unknown, it is possible that dark matter annihilation in these high-density objects may contribute to the gamma-ray background [254, 255]. The probability that such sources will exhibit spatial motion in the duration of the Fermi-LAT mission is directly linked to their abundance, and thus the use of the correlation function can provide information on the survival rate of these extremely early-forming objects.

The spacetime correlation function can be applied to lensing surveys to search for compact objects in the Milky Way. Past studies suggest that up to 20% of unseen matter is in the form of Massive Compact Halo Objects (MACHOs) [295, 296]. With the advent of dedicated surveys e.g., LSST, [297], as well as astrometric missions such as SIM [298] and Gaia [299], it will be possible to generate time-domain maps of lensing events in dense stellar fields. Such information can be used to probe correlated events originating from the spatial translation of compact objects, thus probing the projected velocity distribution of the compact population in the Milky Way. In addition, it may also be possible to place constraints on the density, abundance and

distribution of dark matter substructure [300].

Throughout the development of the analysis we assumed that the event rate due to any source was constant in time. There are many classes of astrophysical objects with time-dependent emission. Most notably, unresolved pulsars are thought to contribute to the diffuse gamma-ray background (e.g. [301, 302]). While these sources will not exhibit proper motion over the course of observations the temporal correlations of their emitted photons may be discovered through techniques based on the ones presented here [4]. Essentially, one chooses the volumes $V(p)$ according to (5.3) (illustrated in the upper panel of Fig. 5.3), but with a non-trivial slicing along the time axis. Such a $V(p)$ picks up on stationary objects which exhibit correlations within their photon time series.

The power of this analysis for untangling the contribution of different classes of sources requires that each class have "different enough" velocity, luminosity, and spatial distributions. For example, if two classes have similar velocity and spatial distributions then one may as well just treat them as a single class with a modified luminosity function. This points to a problem that is likely to be encountered in many realistic astrophysical applications: the angular velocities of almost all objects will be much too small to be resolved by a detector. That is, when one combines the velocity distribution f_i with the spatial distribution n_i in (5.36) it may be that $\xi = 0$ at all angular velocities except in a tiny range near $\omega = 0$. This is because virtually all of the objects have distances and speeds such that their apparent proper motion is below the angular resolution of the detector. A large degeneracy is created and it will be impossible to pull out information about any specific class of objects. The fact that ξ is not zero at $\omega = 0$ indicates the *existence* of objects. However, without being able to measure the shape of ξ for different angular speeds ω the 2-point function loses its value as a tool to untangle the contributions from different

classes of objects.

Of course, as the resolutions of detectors improve, the 2-point function becomes more useful. It is a straightforward task to calculate $\xi(\omega_1, \omega_2; t_1, t_2)$ for specific classes of objects and find out over what ranges of ω and t the correlation drops to zero. For example, if ξ goes to zero around $(\omega_1 = \omega', t_1 = t')$ then a detector which has resolution better than $\theta \approx \omega' t'$ can measure the shape of $\xi(\omega, t)$ as it goes from a maximum at $(\omega_1 = 0, t_1 = 0)$ to zero at $(\omega_1 = \omega', t_1 = t')$.

In summary, we introduced the spacetime correlation function, a statistical tool that can be used to search for the presence of moving, flux-unresolved sources in a diffuse background. This formalism has numerous applications. With large area sky surveys and long duration baselines the spacetime correlation function can be used to disentangle the contributions from spatially moving sources, and may aid in the discovery of new sources.

Chapter Six

Extracting the unresolved pulsar contribution to the gamma-ray background

6.1 Introduction

The Large Area Telescope (LAT) onboard the Fermi Gamma-ray Space Telescope (Fermi) is a powerful instrument that collects energetic photons from the whole sky, at an energy and spatial resolution as well as in an energy range that offers a new window on high energy astrophysics. In over four years since the launch of Fermi, the sensitivity of the instrument has facilitated the discovery of new classes of objects, including gamma-ray pulsars. Over 80 gamma-ray pulsars have been discovered in the Fermi−LAT all-sky data (see [303], and also [304–313, 307, 314]).

While it is expected that more pulsars will be discovered as the baseline of the experiment is extended, most will remain undetected because their fluxes are below the sensitivity level of current detection techniques. These pulsars, as a population, contribute to the diffuse gamma-ray background. Untangling the contributions to this background has been a subject of great interest, not only in the context of pulsar physics [301], but also in studies aimed at understanding the gamma-ray background near the Galactic center [315, 112, 116, 316, 117, 317]. Additionally, understanding the gamma-ray background is necessary to extract faint signals due exotic sources such as dark matter [318] and antimatter [319].

In this paper we propose a new statistical search strategy that can be used to learn about the *cumulative* contribution of pulsars to the gamma-ray background. This technique is an example of a general philosophy/strategy that we advocate, which is based on the concept that even though individual data samples may not contain a detectable source, the statistics of a large number of samples contains information about the sources (see also [3] described in Chapter 5). For the particular case we are studying here, even when a pulsar is not detected within a region of the sky, the

data from that region will still contain information. When a large amount of such data is aggregated one can identify a statistical signature of the presence of pulsars even though the individual objects may not pass sensitivity thresholds.

Such a statistical analysis can reveal the properties of the unresolved pulsar population. Application of this technique to Fermi-LAT data can place bounds on the cumulative contribution of pulsars to the gamma-ray background which are independent of known sources. It is therefore a complimentary approach to the individual studies of bright pulsars with Fermi [320, 321].

We begin in Sec. 6.2 by describing the general strategy that can be used to learn about populations of objects when each individual one is undetectable on its own. We discuss this in the context of the unresolved pulsar contribution to the gamma-ray background. In Sec. 6.3 we propose a specific implementation involving the statistics of the maximum peaks in a collection of power spectra. It is developed in the framework of classical hypothesis testing, where the goal is to reject the null hypothesis that no pulsars are present in the gamma-ray sky. This includes the development of the statistical tests used to reject this null hypothesis. In Sec. 6.4 we make predictions for this method as applied to data from Fermi-LAT and show that under a wide range of circumstances Fermi should be able to discover the presence of unresolved pulsars. Additionally, we show that individual, flux-unresolved, pulsars may be discovered based only on analysis of their time series. We discuss ways to extract the cumulative pulsar contribution to the background, which requires making assumptions about parameters of describing the pulsar population. Finally, in Sec. 6.5 we outline how this technique can be generalized to use more powerful tests for periodicity and discuss caveats which can affect the sensitivity of the method.

6.2 General Methodology

The detection of a pulsar at high significance relies on statistical tests performed on a collection of photon arrival times. (At radio frequencies, where the vast majority of pulsars have been discovered, the time series is in the radio intensity, not photon counts.)

For the sake of simplicity assume that a certain statistical test boils down the entire time series into a single number, a "score"[1], which is supposed to represent the "level of periodicity present". The higher the number the stronger the periodic signal. "Detecting" a pulsar is an exercise in classical hypothesis testing and one needs to take into account the fact that even if there is no pulsar present the score may be high because of random chance. Specifically, one needs the probability distribution for the score conditioned on the null hypothesis that there is no pulsar present. The question is asked, "What are the chances that the score would have been as high as measured if there was no underlying periodicity in the time series?" If the answer is, for example 0.3%, then a pulsar is said to be detected at 99.7% (or "3σ") significance. In this example, the value of 0.3% is called the false alarm probability and in practice a 3σ detection is hardly convincing. Usually, discoveries are claimed when the false alarm probability is less than 6×10^{-7}, a "5σ" detection threshold.

The dominant factor in the detectability of a gamma-ray pulsar is the number of its photons which are collected by the LAT (i.e. the pulsar's photon flux). So far, Fermi has detected pulsars with fluxes as low as 10^{-8} cm^{-2} s^{-1} [303]. These are pulsars whose time series are extremely unlikely to have been generated by a

[1]Throughout this article "score" is used in this sense and has nothing to do with the statistical concept of score defined as the derivative of the log-likelihood.

non-periodic process — unlikely in the sense just discussed. However, it is quite likely that for every pulsar with such a flux the Galaxy contains a great many more with much smaller fluxes. If we assigned a periodicity score to the time series of these faint pulsars the false alarm probabilities would be considerably greater. Most of them would be of order 1. Individually, these pulsations are undetectable with current data and periodicity tests.

However, what if one computes the periodicity score for 40,000 time series, i.e. for every 1 square degree pixel on the sky? A few of these pixels will contain bright pulsars that will be unambiguously detected (these are the pulsars that are discovered using current pulsar search techniques). It is possible that many more pixels contain pulsars which are not obvious in the data (i.e. their periodicity scores are not improbably high), while most of the pixels will likely contain no pulsars at all. The goal then is to infer the presence of the undetected population of pulsars.

The method we propose in this manuscript is based on a very simple observation: The periodicity scores from many separate time series, taken as collection, will be skewed toward larger values due to the presence of pulsars. By analyzing the distribution of scores we can learn about a population of objects whose individual members remain undetected.

This general idea is not limited to the study of the galactic pulsar population. In fact, the concept of analyzing a collection of individually ambiguous signals to learn about a population underlies many studies of diffuse backgrounds. As an example, measuring the empirical counts PDF in sky pixels has been exploited in the study of blazars [322, 323], dark matter annihilation in substructure [324, 201, 323, 200, 325], as well as pulsars [302, 326]. In these cases, the fact that the PDF differs from Poisson indicates that localized sources contribute to the background (even though

any single "hot pixel" does not constitute a detection of an individual source.)

A very simple example can illustrate the idea. Imagine we have a collection of 40,000 coins of which 98% are fair while the other 2% are rigged to land on heads 90% of the time. We get to flip each of the coins once and then try to answer the question, "Are there any unfair coins in this sample?" On the basis of one flip we have no way of saying whether any individual coin is fair or not. But perhaps the overall distribution of flip results can reveal information about the population of unfair coins. For example, suppose this experiment results in getting the expected number of heads: $40000 \times (0.98 \times 0.5 + 0.02 \times 0.90) = 20320$ heads. We pose the hypothesis test: if the coins were all fair what is the probability of getting 20320 or more heads? The answer is

$$\mathrm{P}(\geq 20320) = \sum_{i=20320}^{40000} \binom{40000}{i} (0.5)^{40000} \simeq 0.0007. \tag{6.1}$$

That is, there is a 0.07% chance of getting the results we did if every coin were fair. The hypothesis that all the coins are fair has been rejected with greater than 99.9% significance.

Translating this scenario into pulsar language, each coin represents a one square degree patch of the sky. Flipping a coin corresponds to computing the periodicity score from that pixel's photon time series. Heads is a "high" score and tails a "low" one. If a pixel contains a pulsar the periodicity statistic gives a high score 90% of the time. The periodicity score for a pixel with no pulsar present has equal chances of being high or low and one can not make any definitive claims based on the results of an individual measurement. However, the cumulative number of "high periodicity scores" from all 40,000 square degrees is strongly inconsistent with "no pulsars".

6.2.1 Cookbook

The strategy discussed so far is general but can be decomposed into several specific tasks. Here, we will outline the necessary steps, and in Sec. 6.4 we will develop a specific realization of this procedure which has been designed for application to Fermi-LAT data.

The first step is to take the gamma-ray events in a region of the sky and divide them into spatially separated time series. This can be done based on a simple pixelization of the sky or by collecting the photon time series from many promising locations (we will address these choices in Sec. 6.5). Some preprocessing of the data should also be performed (e.g. applying a barycenter correction to each time series which corrects for the detector's motion with respect to the "fixed" solar system barycenter), as well as detector-specific corrections (e.g., see the Fermi Science Support Center[2]).

Next, a periodicity test statistic is chosen and applied to each time series. The choices for the test are numerous. We will detail a straightforward choice in Sec. 6.4. In general, the requirement is that one must assign a "score" to each time series which in some sense reflects the level of periodicity present. The test should be tailored to the type of objects one is searching for. For millisecond pulsars (MSPs), for example, it may not be necessary to take into account the effects of spin-down (see Sec. 6.5).

It is essential to quantify the response of the test statistic to a white noise time series, i.e. an uncorrelated sequence of photons which was not generated by a pulsar. Specifically, one needs the probability distribution for the score un-

[2] `http://fermi.gsfc.nasa.gov/ssc/`

der the null hypothesis that no pulsar is present. This is called the null distribution. In the coin flipping example we used above, this probability distribution was $P_0(\text{heads}) = P_0(\text{tails}) = 0.5$. In some cases the null distribution can be derived analytically. For more complicated periodicity tests the distribution can be found by simply running the periodicity test many times on randomly generated white noise time series.

Finally, given the collection of scores from the various time series, one tests the collection as a whole for deviation from the null distribution. There are a number of statistical tests that can be used for this purpose. Choices include the Kolmogorov-Smirnov and Anderson-Darling tests as well as the traditional χ^2 test of the binned histogram of scores. For the present application, we introduce an additional test, the A-test. It is designed to be sensitive to a very small tail of high periodicity scores (see next section and Appendix for more details).

6.3 Specific implementation

In this section we present a methodology based on the above strategy. The goal is to detect the presence of unresolved pulsars by jointly examining the photon time series from numerous pixels in some area of the sky. For the sake of simplicity, we will assume that the pulsar period derivatives are very small. This particular implementation is appropriate for a search for the cumulative contribution of MSPs [327, 328] but can easily be generalized to the case where period derivatives are significant.

6.3.1 Choice of periodicity test

We need a numerical quantity, calculated from the measured photon data from each pixel on the sky, that describes the level of periodicity present in the time series. For this exercise the periodicity score of a time series is chosen to be *the normalized peak magnitude of the power spectrum*. We now explain what this quantity represents and how to compute it from a list of discrete photon arrival times.

The Fourier transform is an alternate representation of the time series which highlights the various sinusoidal components that make up the signal. If a pulsar light curve is a pure sine wave its Fourier transform is a delta function spike at the pulse frequency. A well-used technique in pulsar searches is to take the squared magnitude of the complex Fourier transform, called the power spectrum, and search for peaks in this function. The statistics of the power spectrum for both random data [e.g. 329] and for data which contains a signal [330, 331] have been well studied in general and in the context of pulsar searches.

If photons arrive at times $t_1, t_2, \ldots, t_N$ we treat the signal as a train of delta pulses at these times:

$$s(t) = \sum_{j=1}^{N} \delta(t - t_j).$$

Plugging this into the definition of the continuous-time Fourier transform yields

$$\tilde{s}(f) \equiv \int_{-\infty}^{\infty} e^{-2\pi i f t} s(t) dt = \sum_{j=1}^{N} e^{-2\pi i f t_j}. \tag{6.2}$$

The unnormalized power spectrum is the absolute square magnitude of the Fourier transform. It is normalized by dividing by the mean power at each value of f. For

data which contains systematic noise, calculating a running mean is required and may not be trivial. Ransom *et al.* [329] present several techniques, including using a running mean or a running median (divided by ln(2)) to normalize the power spectrum. For gamma-ray data at the high frequencies associated with MSPs there is likely no systematic non-white noise spectrum contaminating the time series. In this case (pure white noise) the mean is simply equal to the number of discrete photon events in the time series. Therefore we search for peaks in the normalized power spectrum $P(f)$ defined as

$$\begin{aligned} P(f) &\equiv \frac{1}{N}\left|\tilde{s}(f)\right|^2 \\ &= \frac{1}{N}\left\{\left[\sum_{j=1}^{N}\cos(2\pi i f t_j)\right]^2 + \left[\sum_{j=1}^{N}\sin(2\pi i f t_j)\right]^2\right\}. \end{aligned} \tag{6.3}$$

We are only interested in the maximum of this quantity, and so computationally it is not necessary to store the entire Fourier transform in memory at any one time. This obviates the need for the 10 billion point Fast Fourier Transforms (FFTs) that would be required for time series that are years long. Instead, one can calculate the power spectrum by making incremental steps in the frequency, only saving the maximum power seen so far. This procedure is trivially parallelized by dividing the frequency interval to be searched into subintervals and searching each of these for its highest peak. [329] provide trigonometric recurrences which can keep track of the the two sums in Eq. 6.4 as f is incremented in small steps without having to compute sines and cosines.

The power spectrum is not an independent quantity for all values of f. It is a standard result from the study of discrete Fourier transforms that independent frequency "bins" have width $1/T$, where T is the elapsed time over which the data was taken. For example, a three year LAT observation results in a width of 10^{-8} Hz

for each independent frequency bin. In searching for MSPs we would like to search over a frequency range corresponding to pulsar periods between, say, 1 ms and 100 ms. In order to perform the search for peaks in the power spectrum we would first compute $P(f)$ starting at $f_{\rm min} = (100\ {\rm ms})^{-1} = 10$ Hz and then take steps of size[3] $\delta f = 1/T \simeq 10^{-8}$ Hz until reaching $f_{\rm max} = (1\ {\rm ms})^{-1} = 1000$ Hz. Therefore, the exploration of the normalized power spectrum for each time series requires searching $\mathcal{N}_{\rm bins}$ frequency bins, where

$$\mathcal{N}_{\rm bins} = (f_{\rm max} - f_{\rm min})T \approx 9 \times 10^{10}. \tag{6.4}$$

In general, pulsar light curves are more complicated than sine waves which results in the Fourier transform having a series of spikes at integer multiples of the pulsar frequency. This fact motivates many pulsar searches to look for spikes in the sum of the first k harmonics of the power spectrum. Here we perform a more simple analysis that does not include the statistical details of searching the harmonic sum. However in practice, the pulsar search may be more sensitive if the highest harmonic-summed peak is used as the test statistic. We defer the discussion of various choices for the test statistic to a later section.

In summary, we compute the normalized power spectrum for the photon arrival time series for each pixel on the sky. The peak power in the power spectrum (in the frequency range of interest) is assigned to that pixel as its "periodicity score". We will now explore the probability distributions describing the scores.

[3] In practice, one usually searches using a smaller step size in order to accurately explore each potential peak in the power spectrum. However, this does not change the number of *independent* frequency bins searched.

6.3.2 Statistics of the power spectrum peak for random data

For each pixel the maximum of the power spectrum is a random variable. Following standard notation we call the random variable X. A specific realization (or measurement) of X is denoted by a lowercase x. If a pixel does not contain a pulsar, we assume that its power spectrum is just white noise, i.e. there are no periodic signals present in the frequency range of interest. In this case, the normalized power in each independent frequency bin is distributed according to an exponential distribution with a mean of 1 (e.g. [329]).

Under the null hypothesis of no pulsars the score X is the maximum of $\mathcal{N}_{\rm bins}$ independent exponentially distributed random variables. The cumulative distribution function (CDF) $F(x)$ is the probability that all of the $\mathcal{N}_{\rm bins}$ random variables are less than x. This is simply equal to $[F_1(x)]^{\mathcal{N}_{\rm bins}}$, where $F_1(x) = 1 - \exp(-x)$ is the CDF for a single exponentially distributed variable. The value of $\mathcal{N}_{\rm bins}$ is large (Eq. 6.4) and we can therefore make the following approximation,

$$\begin{aligned} F(x) &= [1 - \exp(-x)]^{\mathcal{N}_{\rm bins}} \\ &= \left[1 - \frac{e^{-(x - \log \mathcal{N}_{\rm bins})}}{\mathcal{N}_{\rm bins}}\right]^{\mathcal{N}_{\rm bins}} \\ &\simeq e^{-e^{-(x - \log \mathcal{N}_{\rm bins})}}. \end{aligned} \tag{6.5}$$

This result holds to high precision when $\mathcal{N}_{\rm bins} \sim 10^{10}$.

The above expression shows that X is distributed according to what is known as a Gumbel distribution, sometimes called an "extreme value distribution". The probability distribution falls off extremely rapidly to the left of the mode at $x = \log \mathcal{N}_{\rm bins}$ and has a less steep tail to the right. Because $\log \mathcal{N}_{\rm bins}$ is a location parameter of the distribution the width of the Gumbel distribution does not change as $\mathcal{N}_{\rm bins}$ increases.

Also note that as the observation time increases the distribution shifts to the right at a logarithmic rate. This has important consequences that we discuss later. Looking ahead, as the observation time T increases, a pulsar's power will grow in proportion to T while the random power it competes with grows only as $\log T$.

It is easy to invert $F(x)$ to find

$$x = \log \mathcal{N}_{\text{bins}} - \log(-\log F). \tag{6.6}$$

Therefore, given a uniform deviate F between 0 and 1, Eq. 6.6 can be used to transform it into a Gumbel distributed random variable.

6.3.3 Statistics of the power spectrum peak when a pulsar is present

The only distribution needed in order to perform an experiment that tests whether pulsars are present in the gamma-ray background is the null distribution given by Eq. 6.5. The test is simply whether the collection of time series is consistent with none of them containing any pulsar signal. In that case the score X for each time series is distributed as Eq. 6.5.

However, in order to test the sensitivity of this method we need to be able to simulate situations where pulsars are present in the sky. In fact, to learn anything about the details of the pulsar population one needs some sort of model for the way pulsars contribute to the background. Here we discuss how the presence of a pulsar affects the chosen periodicity statistic. We will return later to the question of extracting population parameters from the time series data.

When a pulsar contributes photons to the time series, the peak of the power spectrum is distributed differently. In this case X is distributed as the maximum of two variables. The first is a random variable representing the power in the bin at the pulsar's frequency. The second is a Gumbel distributed variable corresponding to the maximum power in the other $(\mathcal{N}_{\text{bins}} - 1)$ frequency bins. For frequency bins which are not at the pulsar's frequency, the pulsar photons contribute to the Fourier transform as if they were randomly distributed along with all the other photons. That is, the normalized power spectrum for the $(\mathcal{N}_{\text{bins}} - 1)$ other frequency bins is a white noise spectrum. We have already shown that the maximum power that will be found in these $(\mathcal{N}_{\text{bins}} - 1)$ bins is distributed according to $F(x)$ (Eq. 6.5).

In order to determine the height of the normalized power spectrum for the bin at the pulsar's frequency we have to go back to the definition of the Fourier transform[4]. The Fourier transform (Eq. 6.2) is seen to be the sum of unit vectors in the complex plane, one vector for each photon in the time series. In the case of white noise, each of these N vectors has a random direction and the sum can be thought of as the endpoint of a random walk. This gives rise to the power in one frequency bin being distributed according to the exponential distribution with scale parameter N. More precisely, let $\mathbf{y}$ be the sum of N randomly directed 2-dimensional unit vectors. The direction of $\mathbf{y}$ will be uniformly distributed between 0 and 2π. The squared length of $\mathbf{y}$ will be distributed according to

$$\text{Prob}(\zeta < |\mathbf{y}|^2 < \zeta + d\zeta) = \frac{e^{-\zeta/N}}{N} d\zeta \tag{6.7}$$

It is easy to see that the normalized power in such a frequency bin, given by $|\mathbf{y}|^2/N$, is exponentially distributed with scale parameter equal to 1, as stated above.

[4]This paragraph is based on the geometric interpretation given in [331].

Consider now a time series where $N_{\rm s}$ photons come from a pulsar and $N_{\rm bg}$ are uncorrelated background photons, such that the total number of photons is $N = N_{\rm s} + N_{\rm bg}$. We examine the Fourier bin at the pulsar's frequency and consider the idealized case where all the pulsar power lies in this single frequency bin with no power in harmonics. In this case each vector in the sum in Eq. 6.2 over the $N_{\rm s}$ pulsar photons points in the same direction. It therefore has a length equal to $N_{\rm s}$. The other $N_{\rm bg}$ background photons point in random directions and their sum in the Fourier transform is given by a randomly directed vector whose squared length l is distributed according to Eq. 6.7 with N replaced by $N_{\rm bg}$. To get the value of the normalized power spectrum for this frequency bin we take the squared length of the sum of the "signal vector" and the "background photon vector" and divide by the total number of photons in the time series. Defining P_p to be the normalized power in the frequency bin at the pulsar's frequency we have

$$P_p = \frac{1}{N}\left[{N_{\rm s}}^2 + l + 2N_{\rm s}\sqrt{l}\cos(\theta)\right].$$

The power spectrum height is seen to be a random variable: the quantity l is distributed as $l \sim (1/N_{\rm bg})\exp(-l/N_{\rm bg})$ and θ is a uniform random variable between 0 and 2π.

We introduce the following new variables:

$$\mathcal{S} \equiv \frac{N_{\rm s}}{\sqrt{N}} = \frac{N_{\rm s}}{\sqrt{N_{\rm s} + N_{\rm bg}}} \tag{6.8}$$

$$f_{\rm b} \equiv \frac{N_{\rm bg}}{N} = \frac{N_{\rm bg}}{N_{\rm s} + N_{\rm bg}} \tag{6.9}$$

The first can be thought of as a signal to noise term representing how many photons in a pixel are due to a pulsar vs. background. The second measures the fraction of

photons in a pixel which are not due to the pulsar. In terms of these the normalized power spectrum becomes

$$P_p = \alpha\,\mathcal{S}^2 + l' + 2\sqrt{\alpha}\,\mathcal{S}\,\sqrt{l'}\cos\theta, \tag{6.10}$$

where the variables θ and l' are distributed according to

$$l' \sim \frac{1}{f_{\rm b}} e^{-l'/f_{\rm b}}$$

$$\theta \sim \text{Uniform}[0, 2\pi].$$

In Eq. 6.10, α is introduced to take into account the fraction of the pulsar's total power that lies in this single frequency bin. If the light curve of the pulsar were a perfect sine wave all of the signal power would lie in the bin at the fundamental frequency and $\alpha = 1$. In more realistic situations the power will be divided up into higher harmonics and α may be less than 1.

For reference, we note that the probability distribution of P_p has been worked out analytically in [330], which also contains general results that may be of use when considering more complicated tests for periodicity. In particular, the probability distribution for the sum of an arbitrary number of harmonics in the power spectrum is also derived.

6.3.4 Rejecting the null hypothesis of "No pulsars"

As described above, each sky pixel is assigned a periodicity score X which is defined to be the peak height of its normalized power spectrum. The goal is to take this

collection of X values and perform a statistical test of the following null hypothesis: The time series for every pixel is nothing but white noise, i.e. no pulsars are present in any of the pixels. More precisely, we ask if the collection of measured X values is consistent with each score being drawn from the distribution in Eq. 6.5 (i.e. generated by a random white noise time series).

This task can be accomplished by a number of statistical methods. Here, we use a new test developed specifically for this application. In this section we outline how the test works and refer the reader to the Appendix for details.

It is desirable (and possible) to use a classical hypothesis test to learn about the sensitivity of this method. The idea is to boil the collection of measured X values into a single test statistic we call A. The quantity A should, in some sense, indicate the overall level of periodicity present in the gamma-ray sky, just as X did for a single pixel. Small values of A should indicate "less evidence for periodicity" than do large values of A.

The "A test" is based on the quantity (see Appendix),

$$A = \frac{1}{\sqrt{N}} \left\{ \left[\sum_{i=1}^{N} -\log\left[1 - F(x_i)\right] \right] - N \log N + \log N! \right\}, \tag{6.11}$$

where the x_i are the measured scores (normalized power spectrum peaks) for each of the N time series and $F(x)$ is the CDF of the null distribution given by Eq. 6.5. The test is designed to give more weight to time series with large scores.

The test statistic is treated as a random variable and its probability distribution under the null hypothesis (that every sky pixel contained only non-periodic, random photons) is quantified. A significance threshold is chosen and the critical value A^* is

defined so that if the null hypothesis holds, then the probability that $A < A^*$ equals the chosen significance. For example, if we want to perform a "3σ" search one finds A^* such that $\mathrm{P}(A < A^*) = 0.997$. If we find that the observed value of A is in fact greater than A^* the null hypothesis is to be rejected at "3σ" significance. In other words, it would be extremely unlikely to measure such a high value of A if there were no pulsars. This indicates that pulsars contribute to the gamma-ray background.

6.4 Application to Fermi-LAT

We now turn to the question of detecting the presence of pulsars in the gamma-ray sky using current data. We assess the conditions where the proposed formalism is successful in rejecting the null hypothesis of "no pulsars" in the diffuse background as measured by the LAT instrument on board Fermi. In this section, we will demonstrate the robustness of this method by generating simulations which contain a controlled population of pulsars with known properties. We utilize the maximum normalized power periodicity test along with the A test as described above.

Assume that a region of the sky is isotropically populated with pulsars that all have the same flux, Φ_p, defined as photons per area per time in some energy range. These pulsars contribute a fraction γ of all the photons received by the LAT in this energy range. That is, of all the photons that LAT detects over the entire sky a fraction γ of these originated from pulsars each having a flux Φ_p. The projected number density of pulsars is given by σ_p (number of pulsars per solid angle).

The average flux the LAT measures is given by F_{tot} in units of photons per area per time per solid angle (in the relevant energy range). In addition to pulsars we

assume a uniform, isotropic background flux $F_{\rm bg}$ (same units as $F_{\rm tot}$). The independent parameters of this model are Φ_p and γ. The background flux is chosen to make up the difference between the pulsar contribution and the observed total flux. Specifically,

$$F_{\rm tot} = F_{\rm bg} + \sigma_p \Phi_p, \tag{6.12}$$

and

$$\gamma F_{\rm tot} = \sigma_p \Phi_p. \tag{6.13}$$

These two equations determine $F_{\rm bg}$ and σ_p in terms of Φ_p, γ, and the observed $F_{\rm tot}$. These equations are more easily interpreted by multiplying through by the solid angle of the survey and by the observation time and effective area of the detector. Then $F_{\rm tot}$ becomes the total number of photons received by the LAT over the entire survey area, σ_p becomes the total number of pulsars in the survey area, Φ_p the number of photons received from each pulsar, and $F_{\rm bg}$ the total number of background (non-pulsar) photons received over the survey area. Solving the above equations we find

$$F_{\rm bg} = (1-\gamma) F_{\rm tot}, \tag{6.14}$$

and

$$\sigma_p = \frac{\gamma F_{\rm tot}}{\Phi_p}. \tag{6.15}$$

We assume a value of $F_{\rm tot} = 8.72 \times 10^{-10} {\rm cm}^{-2} {\rm s}^{-1} {\rm deg}^{-2}$, in the energy range $[0.8 - 6.4]$ GeV [127]. This includes the energy range in which pulsars are most important relative to the total flux [303].

In order to generate simulated data, we need a survey area and pixel size. We choose the pixel size, Ω, to be 1 square degree, and we will use two choices for the survey area: 40,000 square degrees which represents the all-sky survey, and 1,000

square degrees, which roughly represents the inner $\sim 32 \times 32$ degrees around a region such as the Galactic center.

We must evaluate Eqs. 6.8 and 6.9 to generate a normalized power for each pixel that contains a pulsar. The number of background photons in a pixel is

$$N_{\rm bg} = F_{\rm bg}\,\Omega\,A_{\rm eff}\,T, \tag{6.16}$$

where $A_{\rm eff}$ is the (orbit-averaged) effective area of LAT (2000 cm^2) and T is the observation time (3 years). The number of pulsar (signal) photons in a pixel which contains a pulsar is

$$N_{\rm s} = \Phi_p\,A_{\rm eff}\,T. \tag{6.17}$$

Inserting these quantities in Eqs. 6.8 & 6.9, we have

$$\begin{aligned} \mathcal{S} &= \sqrt{\frac{\Phi_p}{F_{\rm bg}\Omega + \Phi_p}\Phi_p A_{\rm eff} T} \\ &= \left(1 - \gamma + \frac{\Phi_p}{F_{\rm tot}\Omega}\right)^{-1/2} \left(\frac{\Phi_p}{F_{\rm tot}\Omega}\right) \sqrt{F_{\rm tot}\,\Omega\,A_{\rm eff}\,T}, \end{aligned} \tag{6.18}$$

and

$$f_{\rm b} = \frac{1-\gamma}{1-\gamma+(\Phi_p/F_{\rm tot}\Omega)}. \tag{6.19}$$

For a given choice of Φ_p and γ we can use these last two equations along with Eq. 6.10 to generate a normalized power in a pixel that contains a pulsar [5]. For simplicity the simulations were performed using $\alpha = 1$. Consequences of relaxing

[5]There are many choices for Φ_p and γ that give a number of pulsars which is larger than the number of pixels, i.e. $\sigma_p\Omega > 1$. When this is the case we need to generate a normalized power for each pulsar in the pixel, a peak power from the other $\sim \mathcal{N}_{\rm bins}$ frequency bins and then take the maximum of all these to be the periodicity score X for the pixel. We have found that for the range of parameter space we discuss the extra pulsars in each pixel do not change the results. Therefore, we run the simulations with at most one pulsar per pixel (though σ_p is allowed to be greater than 1).

this assumption will be discussed later.

We explore the parameter space to see when pulsars will be detected by this method using the A statistic defined above. We choose a value of A^* corresponding to a 99.7% ("3σ") detection. For each pair of values Φ_p and γ we create 1,000 realizations. For each realization we simulate 40,000 (all-sky) and 1,000 (Galactic center) values of X (one for each pixel) and compute the A statistic. Out of the 1,000 trials we count the number in which the null hypothesis is rejected. The fraction of trials in which the null hypothesis is rejected is the sensitivity (or power) of the proposed test. For example, if for a particular choice of Φ_p and γ we find that in 900 out of 1,000 simulations the null hypothesis is rejected (i.e. $A > A^*$ in 900 of the simulations), then there is an 90% chance of making a "3σ" detection of the presence of pulsars.

6.4.1 Results

Figure 6.1 shows the results of the parameter space scan over values of Φ_p below 10^{-9} cm^2 s^{-1} and over the full range of γ from 10^{-5} to 1 for a simulated all-sky survey of 40,000 square degrees. The color-coding corresponds to the power of this method to reject the null hypothesis that there are no pulsars at 99.7% ("3σ") significance. In the dark red region the null hypothesis is practically guaranteed to be rejected. In the blue region the null hypothesis will be rejected only 0.3% of the time (as expected for a 99.7% significance threshold). The solid contours correspond to the number density of pulsars (in units of pulsars per square degree) as computed using Eq. 6.15.

There are two competing factors which shape the transition between the sensi-

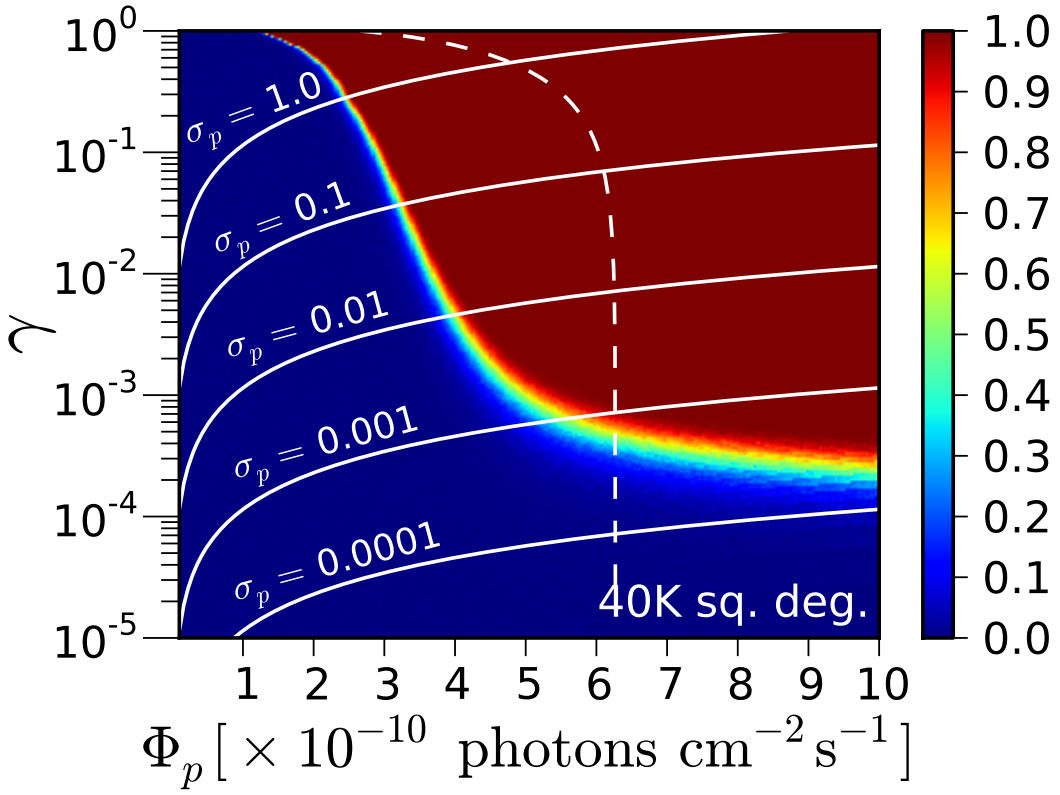

Figure 6.1: A demonstration of the statistical power of the method to detect the presence of pulsars over the entire sky. The color coding represents the probability of rejecting the null hypothesis of "no pulsars" at 99.7% significance. Φ_p is the photon flux of each individual pulsar in the energy range $[0.8 - 6.4]$GeV. The quantity γ represents the fraction of the total gamma-ray background due to pulsars. Solid contours give the number density of pulsars (in units of pulsars per square degree). The proposed method can reveal the presence of a pulsar population contributing as little as 10^{-3} of the diffuse gamma-ray background. Note that, within the range of pulsar fluxes shown, every individual pulsar is *flux*-unresolved because Φ_p is less than LAT's point source sensitivity threshold. Many of these flux-unresolved sources may be individually discovered based solely on an analysis of their time series: the dashed line represents the 5σ detection threshold for individual pulsars based on the height of their power spectrum peak (see text for details).

tive and insensitive regions of parameter space. The plateau at small values of γ represents the limit of low numbers of pulsars. Obviously, if there are no pulsars in the sky there is no signal to be detected. Within the flux range explored here the A test is not sensitive if there are fewer than ~ 10 pulsars in the 40,000 pixels.

The vertical transition is explained by the fact that pulsars must contribute the *highest* peak in the power spectrum in order to be detected by the periodicity test. As the flux of each pulsar is increased (moving to the right in Fig. 6.1) the power spectrum peak at the pulsar's frequency will eventually become the highest peak in the power spectrum. This then causes the non-Gumbel-ness of the pixel scores which is detected by the A test.

We can view this as a requirement that the quantity P_p (Eq. 6.10) be comparable to $\log \mathcal{N}_{\rm bins}$, the mode of the distribution for the maximum normalized power in the case of no pulsars. The $\alpha \mathcal{S}^2$ term in Eq. 6.10 is most important in governing the transition. Because the Gumbel distribtion only contains a location parameter we can write an approximate equation describing the vertical part of the sensitivity transition:

$$\alpha \mathcal{S}^2 \simeq \log \mathcal{N}_{\rm bins}. \tag{6.20}$$

The left hand side is an estimate of the height of the peak corresponding to the actual pulsar signal. The right hand side is the maximum power in the other $\mathcal{N}_{\rm bins} - 1$ frequency bins. Only when the left hand side is greater than the right hand side will the method be able to reject the null hypothesis of no pulsars. This is because the periodicity statistic we have chosen is not sensitive to pulsar peaks which are subdominant in the power spectrum.

The photon fluxes of individual pulsars in the simulated parameter space are all

below the point source sensitivity of the LAT [101]. The pulsars in the simulation would be undetected by Fermi as bright sources. Therefore, "blind searches" would not consider these pulsars as candidates for periodicity searches. Such objects truly contribute to the diffuse background.

Nevertheless, if we measure the power spectrum for a pixel which contains an unresolved pulsar the spike at the pulsar's frequency might be large enough to constitute a detection of a periodic source. To estimate when this occurs we consider the following hypothesis test. We measure a power spectrum peak height of x, and ask "What is the probability that at least one peak in any of the observed time series has a value of x or higher *if* there were no periodic sources present in the data?" The answer again follows from the Gumbel distribution (Eq. 6.5) but with $\mathcal{N}_{\rm bins}$ replaced with $\mathcal{N}_{\rm bins} \times \mathcal{N}_{\rm pix}$, i.e. the number of independent frequency bins for each time series multiplied by $\mathcal{N}_{\rm pix}$, the number of time series considered (in this case 40,000). The quantity $F(x)$ is the significance of this peak.

In the region to the right of the dashed line in Fig. 6.1 individual pulsars would be detected at 5σ based on the height of the power spectrum peak derived from their pixel's time series. The region's shape is governed by an equation similar to Eq. 6.20 except that the right-hand side is replaced by a peak height $x_{5\sigma}$ such that $1 - F(x_{5\sigma}) \simeq 5.7 \times 10^{-7}$, corresponding to a 5σ detection. This suggests that *simply computing the power spectra for the entire sky may turn up detections of pulsars which are too faint to be flux-resolved.*

In Fig. 6.2 we show the results of a similar simulation but for an observation of only 1,000 square degrees of sky. This situation represents a study of the galactic center, a region whose source population is of great interest [315, 112, 116, 316, 117, 317]. The shape of the sensitivity region is similar to the all-sky survey. The stripe

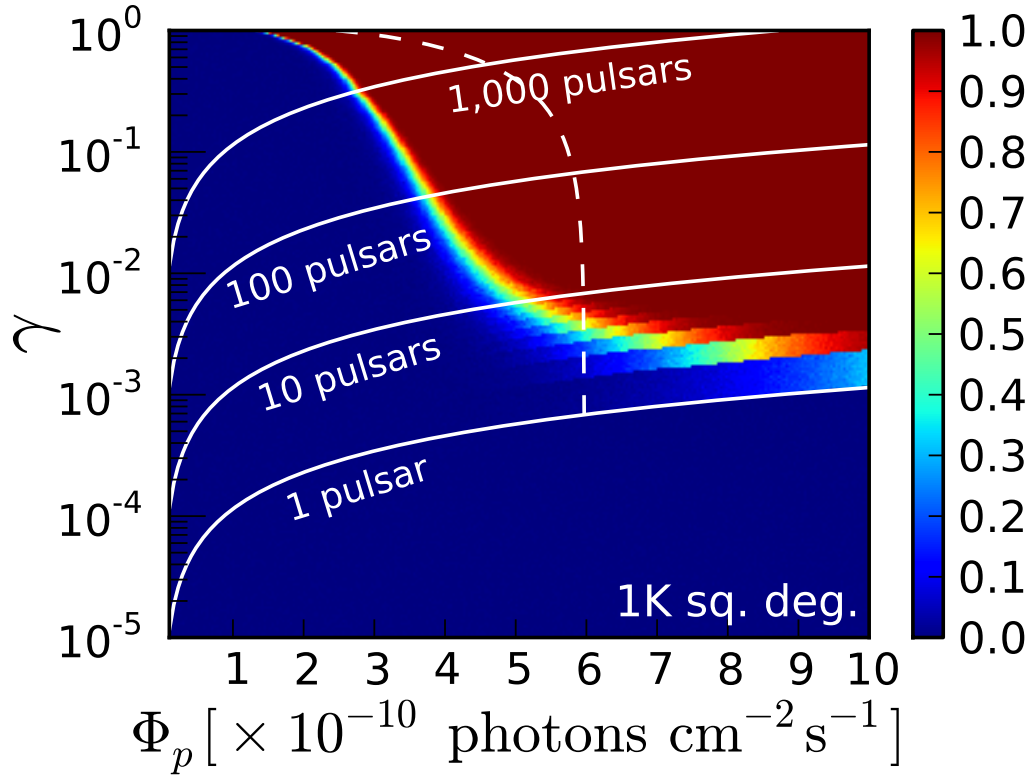

Figure 6.2: Same as Fig. 6.1 but for an observation area of 1,000 square degrees corresponding to a study of the Galactic center. Here, solid contours depict the total number of pulsars present in the observed region. The dashed line denotes the 5σ detection threshold of individual pulsars based on power spectrum peak height as in Fig. 6.1.

pattern is caused by the discrete addition of pulsars to the survey area. *The method is sensitive to the presence of pulsars even when individual pulsars are unresolved in both flux and Fourier power.* The sensitive (dark red) region is larger in the all-sky survey than in the galactic center study. This demonstrates that the statistical test benefits from larger numbers of measured time series (assuming equal fluxes and number densities of pulsars).

6.5 Discussion

Using the approximation to the sensitivity transition given by Eq. 6.20 we can estimate how the result of the simulations discussed in the previous section will scale with changing parameters. The Gumbel distribution we have been exploring has the beneficial property that the location parameter goes as the logarithm of the number of independent trials. We expect this to be a general feature of any periodicity test. Thus, as observation time T increases the right hand side of Eq. 6.20 increases as $\log T$. The left-hand side increases in proportion to ${\Phi_p}^2 A_{\rm eff} T/\Omega$. Thus, this technique benefits from longer observation times, larger effective areas, and smaller pixel sizes (i.e. future gamma-ray observatories) in the same "root N" way that conventional searches do.

The main difficulty in the outlined strategy lies in choosing a good test of periodicity and in the computational challenge of computing it many times for the different time series. Traditionally, pulsars are searched for either by taking a Fourier transform of the time series or by folding the time series in the time domain at many different trial periods.

Regular pulsars do not have constant periodicity but experience spin-down (magnetic braking) and glitches. These complicating factors force statistical tests for periodicity to be performed on a large grid of trial frequency derivatives or on short stretches of the time series [321, 320]. In Fourier space the changing period of the pulsar acts to spread its signal power over many frequency bins, diluting the peak amplitude. Millisecond pulsars, on the other hand, have extremely stable rotations, with period derivatives on the order of 10^{-19} s/s [327]. Even over observation periods of years the frequency of many MSPs will not drift into neighboring Fourier bins [328]. Thus, the number of trials performed when computing the test statistic can be significantly lower than for regular pulsars.

Additionally, MSPs are thought to form in binary star systems. Because binary systems are more common than single stars most galactic pulsars are likely members of a binary pair that have been spun up into MSPs [332–335] In addition, it has recently been suggested that MSPs might dominate normal pulsars in their contribution to the gamma-ray background [302]. Millisecond pulsars are also older, have had more orbital trips around the galaxy, and therefore are more likely to be found at higher galactic latitudes than normal pulsars. Therefore, these pulsars may be important contributors to the so-called "extra-galactic" or isotropic gamma-ray background [326].

6.5.1 Caveats and Improvements

We have been optimistic in some areas and overly simplistic in others. Here we review some of the practical difficulties in performing this test on LAT data and point out the simplifications we have made and how they affect the results.

The most obvious difficulty we have glossed over is the fact that pulsar light curves are not simple sine waves. This has the effect of dispersing the power in the frequency bin centered at the pulsar's frequency into higher harmonics. The simple periodicity test we proposed (maximum normalized power) is almost certainly not optimal for the case when power is found at higher harmonic frequencies (see below for ways to try to recover this power). We have left room in the analysis (see Eq. 6.10) for a reduction of α, designed to account for the effect of power being dispersed into other frequency bins. Equation 6.20 suggests that the pulsar flux one is sensitive to goes as $1/\sqrt{\alpha}$ (since $\mathcal{S}$ scales proportionally to Φ_p).

While millisecond pulsars are extremely stable and do not experience glitches or suffer from rapid spin-down, their rotation is not completely constant. It is therefore probable that some power is dispersed into neighboring frequency bins by non-negligible period derivatives. The techniques used to try to recover this power involve performing many analyses with different trial period derivatives. Specifically, the arrival times of the photons are corrected to account for a spin-down effect and then the periodicity search is performed on this modified time series. The decrease in sensitivity due to spin-down increases as the observation time increases.

As millisecond pulsars are found in binary systems, the orbital motion of the binary can cause distortions in the Fourier spectrum of the time series. Essentially, the orbit of the pulsar causes a doppler shift in its period which disperses Fourier power into different frequency bins. Methods have been proposed that can sweep up this power [336]. Such methods can be incorporated into a more advanced periodicity test.

Errors in source position are known to affect the detectability of individual pulsars. The first step in analyzing a time series is to correct for motion of the detector

with respect to the pulsar. This correction depends on an accurate "barycentering" procedure, which in turn relies on precise knowledge of the pulsar's position. In searching the background for unresolved pulsars we have no information as to where the pulsars are located within the pixels, and this affects the quality of the barycentering.

The most important consideration that goes into a realistic application of the proposed method is the choice of periodicity statistic. In practice, one is bound by finite computational resources — ideally, one would perform a detailed time series analysis on every pixel in the sky, including searching over trial periods, period derivatives, and other ephemera. We have been simplistic in the choice of the maximum normalized power as a test statistic. A first generalization is to search harmonic sums of the normalized power spectrum. This would take into account that pulsar light curves are not sine waves. Considering the harmonic sum of the power spectrum is an attempt to recover the as much signal power as possible. The statistics of such a test are relatively straightforward to compute.

In addition, there are several choices of tests for periodicity currently in use to search for pulsars in radio data and in gamma-rays. The H test [337] and the Z_2^2 test [338] are based on binning the photon arrival times by phase for a given trial pulsar period and then checking whether the distribution of phases is consistent with random. These tests require a guess for the pulsar period. However, it is computationally intensive to calculate the statistic for every possible value of the pulsar period for a large sample of pixels. More recently, a time-differencing technique [321] has been proposed to overcome some of these computational challenges and has been very successful in discovering new pulsars with Fermi-LAT [339, 303].

To adapt these tests to the present task, we propose to first find the power

spectrum of the time series (or its harmonic sum) and take the n highest peaks to be trial periods for the more advanced algorithms. The number of trials n would need to be adjusted based on computational resources and the choice could be calibrated by examining the power spectra from time series which are known to contain gamma-ray pulsars. An automated analysis pipeline can be conceived in which one would perform a cursory scan of the time series looking for semi-significant peaks and then perform additional, computationally intensive scans of these peaks, assigning a periodicity score at the end.

Besides computational cost one has to balance two factors when deciding on a periodicity test. The test should be as sensitive as possible to the presence of periodic signals but should also minimize the number of "trials". A large number of trials raises the possibility that a random signal, by chance, could appear periodic. In our case the number of trials was the number of independent Fourier bins that were scanned when looking for peaks. As the number of "trials" grows it is more likely to find a random outlier that mimics periodicity.

Any periodicity test or analysis procedure can be adapted to the search for unresolved pulsars. The key ingredient is the null distribution of the periodicity scores. For example, an arbitrarily complex analysis pipeline can be established which takes a time series and outputs a periodicity score. The inner-workings of the pipeline can involve scanning over trial periods and period derivatives. It can include identifying promising peaks for more careful scanning. Once the procedure is set, one simply runs it many times on uncorrelated photon time series (i.e. white noise). The resulting set of periodicity scores constitutes the null distribution. The pipeline is then applied to actual measured time series and the resulting scores are collectively checked for inconsistency with the null distribution.

We can illustrate the effect of different tests using the sensitivity plot in Fig. 6.1. Different periodicity tests would shift both the sensitive (red) region and dashed line together. However, the scaling is not necessarily fixed. The dark red region of parameter space to the left of the dashed line remains the most interesting. It is here where searches for individual pulsars would fail but where the collective statistics would succeed in revealing their presence. The size and shape of this region likely depends on which periodicity test is chosen. We plan to explore other tests in future work.

Furthermore, the division of a region of the sky into spatially separated time series (step one in Section 2.1) can also be optimized. Instead of breaking the sky into pixels and taking the time series of each one, an alternate technique is to only search promising sky locations for evidence of periodicity. One could consider only "bright spots" or "hot pixels", regions of the sky with a signal to noise ratio greater than 1, say. Alternatively, the candidate locations can be chosen from lists of known sources (see Fermi bright source list, [340], [341]), or from pulsar candidate locations in blind searches. The later have been previously analyzed for pulsations but have not been *jointly* searched for unresolved pulsars. These strategies have several advantages. The computational burden would be reduced because of the fewer number of time series to scan. The barycenter correction would be improved by the better localization of the sources' positions. A priori, *hot pixels have a higher chance of containing pulsars than randomly selected pixels, leading to a larger fraction of the searched pixels that contain pulsars* (effectively increasing σ_p in Fig. 6.1).

Because the analysis is sensitive only to the highest power spectrum peak it is almost completely insensitive to the possibility that there may be multiple pulsars contributing to a single time series. However, this situation likely occurs in globular clusters and in the galactic center region, both places conceivably containing impor-

tant populations of pulsars. A periodicity statistic should be tailored specifically to studies of these regions. A simple generalization of the periodicity test would be to take the top n highest peaks in each time series instead of just the highest. Then we would have n periodicity scores from each pixel instead of one. Alternatively, one could count the number of peaks with height greater than some threshold. The score from each pixel would be this integer number. (In both cases the search could take place using the harmonically summed power spectra.)

6.5.2 Pulsar population parameter estimation

This analysis begs the followup question of how we can learn the details of the pulsar population from studies like this, where individual pulsars remain undiscovered. In particular, it is of great interest to determine what fraction of the gamma-ray background is due to unresolved pulsars (the value of the quantity γ in the simulations of Sec. 6.4). The detailed extraction of population parameters from the collection of periodicity scores requires some kind of modeling of the population. However, we can use the simplified model presented here to place interesting constraints on the number of pulsars with certain fluxes without any detailed modeling.

In the simulations of Sec. 6.4 we assumed that every pulsar had the same flux. This is obviously false if we claim that the simulated pulsars make up all the pulsars in the sky. However, the simulated pulsars can instead be interpreted as a "slice" of the number function of pulsars.

An important description of the pulsar population is the number density of pulsars $\sigma_p(\Phi_p)$ with flux greater than Φ_p. This function can be used to define the total

contribution from pulsars:

$$\gamma = \frac{1}{F_{\rm tot}} \int \Phi_p \left| \frac{d\sigma_p}{d\Phi_p} \right| d\Phi_p. \tag{6.21}$$

The simple simulations of Sec. 6.4 can be used to constrain $\sigma_p(\Phi_p)$ as follows. Imagine that we have performed a test over the whole sky (Fig. 6.1) but failed to reject the null hypothesis. At each flux Φ_p we can draw a line straight upwards in Fig. 6.1 until we reach the transition to the dark red region. Let the number density of pulsars simulated at this transition point be given by $\tilde{\sigma}_p(\Phi_p)$. Then we can claim that the true number density function at this flux $\sigma_p(\Phi_p)$ must be less than $\tilde{\sigma}_p(\Phi_p)$. If this were not the case then there is a 99.7% (in this example) chance that the statistical test would have detected the presence of these pulsars. This constraint relies on the choice of α and in practice the choice should be calibrated using known pulsar light curves.

If we are willing to make some assumptions about the shape of $\sigma_p(\Phi_p)$ and only allow its overall normalization to vary we can make stronger statements. In this case we could actually simulate a population of pulsars for different choices of normalization and find the sensitivity of the method to each choice. The test will become sensitive above some critical value of the normalization. Depending on whether the test rejects or does not reject the null hypothesis we could then place a lower or upper bound on the normalization of the number density function. This bound would then immediately translate into a bound on the total contribution of pulsars to the background (Eq. 6.21). There are several motivated choices for the shape of $\sigma_p(\Phi_p)$ which depend on the spatial distribution of pulsars [302]. In reality, however, the population of gamma-ray pulsars is completely unconstrained at fluxes below about 10^{-8} photons cm^{-2}s^{-1} [303].

In addition, one can analyze the measured distribution of periodicity scores using conventional χ^2 minimization. In this case it is necessary to know what the distribution of scores will be as a function of the pulsar population parameters. One then can bin the measured scores and find the best fitting population parameters. The pulsar population models can be made as complicated as one likes — the analysis requires a scan over this parameter space looking for regions whose score distribution matches the observed one. We defer applications of these techniques to the LAT data in future work.

6.6 Conclusions

In this manuscript we propose a new technique whose application to Fermi-LAT data can reveal the extent to which pulsars contribute to the gamma-ray background. The method is based on the cumulative statistics of photon time series that are binned spatially. The motivation behind this approach lies in the general idea that even though individual pulsar searches may be unsuccessful, information from undetected pulsars is still measurably encoded in the gamma-ray background.

In general, current pulsar searches are based on the evidence of a source at a particular location. These sources are subjected to a battery of periodicity tests, and careful analysis of LAT data has already revealed the presence of gamma-ray pulsars. However, it is likely that large numbers of pulsars are beyond the current reach of LAT to even identify their associated events. These pulsars (with very weak signals) will contribute to the diffuse gamma-ray background.

Our main results are:

- The proposed technique has the ability to discover a pulsar contribution to the gamma-ray background if the fraction due to pulsars is greater than 10^{-3}.

- It is sensitive to a population of pulsars whose individual photon fluxes are as low as 10^{-10} cm^{-2} s^{-1}.

- Using the photon time series derived from a specific location on the sky, one can discover *individual* pulsars with photon fluxes down to about 6×10^{-10} cm^{-2} s^{-1}, which is below the current point source sensitivity threshold.

- By considering only "hot pixels" or current blind search candidates the sensitivity of the method is increased markedly.

- Any periodicity test or analysis pipeline can be applied to the search for the unresolved population. The only requirement is the response of the test to uncorrelated photon time series. This allows the technique to be optimized for any given application (e.g. all-sky surveys, galactic center, globular clusters, etc.).

The method proposed in this work takes advantage of all events in the diffuse gamma-ray background and gives information about the population of unresolved pulsars. The importance of this task goes beyond pulsar astrophysics. It is manifestly apparent that a detailed understanding of astrophysical backgrounds is vital in any gamma-ray observation, including surveys of astrophysical sources (e.g., blazars), as well as studies of more exotic and hypothetical contributions (e.g., annihilating dark matter). It is therefore of extreme interest to apply this technique to current and future gamma-ray data.

Appendix A

The A test

In this appendix I provide details about the statistical test used in Chapter 6. The test is designed to determine if a collection of observations is inconsistent with having been drawn from a given null distribution. It is meant to be sensitive to a small upper tail in excess of what is predicted by the null distribution. Although motivated by the application to pulsars the A test has nothing to do with astrophysics and may be used in any statistical study.

A.1 Motivation

Recall the situation presented in the text. We have a collection of periodicity scores (denoted x_i) and want to test whether the collection is consistent with having been drawn from the null distribution (in this case a Gumbel distribution). The goal is to boil the collection of scores down into a single number A and then study the distribution of A under the null hypothesis. The quantity A is meant to reflect the overall level of periodicity in the sample.

The critical value A^* is defined by the property that, if the null hypothesis is true, the probability that A is less than A^* is e.g., 99.7%. To be precise, A is a function of the collection x_i. If the x's are each drawn from the null distribution then the probability that A is less than A^* is 0.997, or whatever the desired significance is.

Different choices of A may be more or less powerful. In general, the power of a test is defined as the probability that the null hypothesis is rejected when the null hypothesis is, in fact, false. If it is unlikely that A is above some critical value A^* even when there are many pulsars present in the sky a poor definition for A has been chosen. Unfortunately, only in special, simple cases is there a "uniformly most

powerful" test. In the particular case we are studying here there are many degrees of freedom associated with the alternative hypothesis. For example, the light curves of pulsars and their number density are functions which must be specified by many parameters. As a result there is no uniformly most powerful test in this case. (See e.g. [167] for an more detailed discussion.)

In order to choose a powerful statistical test we must examine the behavior of the collection of x's in the case where pulsars are present. Consider a pixel which contains a pulsar. The only way the x-value of this pixel will contain any information about the pulsar is if the peak in the normalized power spectrum is actually due to the pulsar. Under the null hypothesis, each x is drawn from the Gumbel distribution in Eq. 6.5. The effect of pulsars is to skew the distribution towards higher values of x: the pixels with a pulsar have a chance of replacing the peak power in a random frequency bin with the power at the pulsar's frequency. Based on these considerations we would like to choose a statistical test that puts more weight on higher x values.

There are a wide variety of statistical tests that are in common use. The Kolmogorov-Smirnov (KS) statistic is commonly used in astronomy. Kuiper's extension of the KS statistic gives more weight to the tails of the distribution. This would be beneficial for looking an excess of large x-values. The Anderson-Darling statistic is used more rarely but also gives extra weight to the tails. Likelihood ratio statistics are another option, though these require some knowledge of the alternative hypothesis that one is testing for. It is known that likelihood ratio tests are the most powerful tests for "point" hypotheses [167]. They are based on the likelihood function for the data under various hypotheses, and should therefore exploit all the information available in the data.

The proposed A test statistic is designed to be sensitive to the upper tail of a

distribution. It shares properties with the Anderson-Darling and KS tests and can also be interpreted as a likelihood-ratio test. Unlike these other tests, however, the distribution of the A test statistic under the null hypothesis is very simple (a gamma distribution). It is expected to be powerful (like a likelihood test) but also very easy to use (no sorting of the data and no lookup tables).

A.2 Details

In this subsection I present the details of the A test. The task is to take a collection of numerical values and determine if this collection is consistent with being drawn from a given probability distribution (the null distribution). Below, this collection of numbers will also be referred to as the "data" or the "samples".

When looking for an extended tail in a collection of measured quantities we noticed that it is often useful to look at the logarithm of the empirical survival function (SF) of the data. The empirical SF is defined as $1 - F_N(x)$, where $F_N(x)$ is the empirical cumulative distribution function (CDF). Simply put, the SF at some value x is the fraction of the sample values which are greater than x. Thus, at $x = -\infty$ the empirical SF equals 1 and decreases by $1/N$ every time x crosses one of the measured values, where N is the sample size. This empirical SF can be compared to the theoretical SF for the case where the data come from the null distribution. For the null distribution, the survival function is simply $1 - F(x)$, where $F(x)$ is the usual cumulative distribution function for the null distribution.

When comparing the logarithm of the empirical and theoretical SFs any excess at large values of x becomes more pronounced, even if only a small fraction of the

samples are at such large values. Therefore, we order the data by increasing x-value and define the A statistic as

$$A \equiv \frac{1}{\sqrt{N}} \sum_{i=1}^{N} \left\{ \log\left[1 - F_N(x_i)\right] - \log\left[1 - F(x_i)\right] \right\}, \tag{A.1}$$

where $x_1 < x_2 < \cdots < x_N$ and $F_N(x_i) = (i-1)/N$ is the empirical CDF. We can make some simplifications to the first term in the sum:

$$\begin{aligned} \sum_{i=1}^{N} \log\left[1 - F_N(x_i)\right] &= \sum_{i=1}^{N} \log\left[1 - \frac{(i-1)}{N}\right] \\ &= \log\left[1\left(1 - \frac{1}{N}\right)\left(1 - \frac{2}{N}\right)\cdots\left(1 - \frac{N-1}{N}\right)\right] \\ &= \log\left[N\left(N-1\right)\left(N-2\right)\cdots 1\right] - \log\left[N^N\right] \\ &= \log N! - N\log N. \end{aligned} \tag{A.2}$$

Inserting this back into the definition of A we have

$$A = \frac{1}{\sqrt{N}} \left\{ \left[\sum_{i=1}^{N} -\log\left[1 - F(x_i)\right] \right] - N\log N + \log N! \right\}, \tag{A.3}$$

The statistics of A is governed by the term in curly brackets. In this sum the numerical ordering of the x's does not matter since the sum is over all of them. The distribution of A under the null hypothesis is now straightforward to find. For any random variable X with CDF F the quantity $F(X)$ is distributed uniformly in the interval between 0 and 1. This implies that $1-F(X)$ is also uniformly distributed on this interval. Now, the negative logarithm of such a uniformly distributed variable is distributed according to the exponential distribution with scale factor 1. Therefore, under the null hypothesis the quantity

$$G \equiv \sum_{i=1}^{N} -\log[1 - F(x_i)] \tag{A.4}$$

is the sum of N exponentially distributed random variates. This sum is described by the well-known gamma distribution (also called the Erlang distribution in this case) with shape parameter N. The inverse CDF of the gamma function then provides the critical value A^*. For instance, to find the value of A^* under which there is a 99.7% chance of measuring A (under the null hypothesis) one determines the value of G^* that satisfies

$$0.997 = \int_0^{G^*} \frac{x^{N-1}e^{-x}}{(N-1)!}\,dx. \tag{A.5}$$

The quantity G^* is then inserted into Eq. A.3, replacing the term in large square brackets. The resulting value of A is A^*. If for a given sample of N x-values the quantity A (Eq. A.3) is greater than A^* then one can reject that the sample came from the distribution with CDF $F(x)$ at 99.7% significance.

A.3 Properties of A

Of course, there is no reason to include the constant terms in Eq. A.3. One can just take the test statistic to be G (Eq. A.4), the only quantity that depends on the data. Then G^*, discussed above, is the critical value for the test statistic. (In fact, this is how we actually performed the simulations.) However, the definition we have given for A (Eq. A.3) has a nice asymptotic property for large sample sizes (i.e. as $N \to \infty$). The central limit theorem says that the gamma distribution converges to a normal distribution with mean N and standard deviation $\sqrt{N}$. In the same limit the constant term Eq. A.2 converges to $-N$ as can be seen using the approximation for $\log(N!)$ found in every statistical mechanics textbook (e.g. [342], section A.6). Therefore as $N \to \infty$ the distribution for A converges to a standard normal distribution (i.e. normal with mean 0 and variance 1).

The A test statistic is similar to the KS and Anderson-Darling statistics in that is based on the CDF of the null distribution. The CDF has the nice property that it is distributed uniformly (if the null hypothesis is true). This allows the null distributions for the KS, Anderson-Darling, and A test statistics to be found analytically.

The specific application of the A test statistic shown in this paper can also be interpreted as a likelihood-ratio test. The null distribution is given by the Gumbel distribution with a peak at $\log \mathcal{N}_{\text{bins}}$. Imagine that the alternative distribution for the x's follows the null distribution for values of x less than $\log \mathcal{N}_{\text{bins}}$ but does not fall off for higher values. This is supposed to represent the situation when pulsars are present: there are more large values of x. The likelihood ratio is the ratio of the alternative PDF to the null PDF (as functions of x). When this quantity is large it indicates that the alternative describes the sample better than the null does. The likelihood ratio is the product of these ratios for each x_i. It is usually easier to work with the logarithm of this quantity which is the sum of the logarithms of the individual likelihood ratio terms.

Let us see how each term in the log-likelihood ratio compares to each term in the G statistic (i.e. each term in the curly bracketed sum in Eq. A.3). If x is less than $\log \mathcal{N}_{\text{bins}}$ both statistics contribute approximately 0. In the case of the likelihood ratio this is because the null and alternative PDFs are defined to be the same there (so the log of their ratio is 0). It is also easy to see from Eq. 6.5 that when x is less than $\log \mathcal{N}_{\text{bins}}$, $F(x)$ is close to 0. If x is greater than $\log \mathcal{N}_{\text{bins}}$ the quantity $1 - F(x)$ becomes approximately $\exp(-(x - \log \mathcal{N}_{\text{bins}}))$ and so $-\log(1 - F(x)) \simeq x - \log \mathcal{N}_{\text{bins}}$. For the likelihood ratio when $x > \log \mathcal{N}_{\text{bins}}$ the alternative hypothesis PDF is 1 and the null PDF is approximately $\exp(-(x - \log \mathcal{N}_{\text{bins}}))$. Thus the logarithm of this ratio is also approximately $x - \log \mathcal{N}_{\text{bins}}$.

For all values of x, therefore, the A statistic (based on the quantity G) behaves just like a likelihood ratio test that is designed to pick up an extended upper tail in the sample. This implies that the A test should be a powerful test in looking for such a tail. Moreover, the null distribution of A has a particularly simple form (a shifted and scaled gamma distribution) and converges to the standard normal distribution when the sample size is large, making A an attractive addition to the current library of statistical tests.

Bibliography

[1] Geringer-Sameth, A. and Koushiappas, S. M., 2011, "Exclusion of Canonical Weakly Interacting Massive Particles by Joint Analysis of Milky Way Dwarf Galaxies with Data from the Fermi Gamma-Ray Space Telescope", *Physical Review Letters*, **107**(24), 241 303. [DOI], [ADS], [arXiv:1108.2914 [astro-ph.CO]]

[2] Geringer-Sameth, A. and Koushiappas, S. M., 2012, "Dark matter line search using a joint analysis of dwarf galaxies with the Fermi Gamma-ray Space Telescope", Phys. Rev. D, **86**(2), 021 302. [DOI], [ADS], [arXiv:1206.0796 [astro-ph.HE]]

[3] Geringer-Sameth, A. and Koushiappas, S. M., 2012, "Detecting unresolved moving sources in a diffuse background", MNRAS, **425**, 862–877. [DOI], [ADS], [arXiv:1012.1873 [astro-ph.HE]]

[4] Geringer-Sameth, A. and Koushiappas, S. M., 2012, "Extracting the unresolved pulsar contribution to the gamma-ray background", MNRAS, **421**, 1813–1824. [DOI], [ADS], [arXiv:1106.4813 [astro-ph.HE]]

[5] Milne, E. A., 1935, *Relativity, gravitation and world-structure*. [ADS]

[6] Peebles, P. J. E., 1993, *Principles of Physical Cosmology*. [ADS]

[7] Friedmann, A., 1922, "Über die Krümmung des Raumes", *Zeitschrift fur Physik*, **10**, 377–386. [DOI], [ADS]

[8] Friedman, A., 1999, "On the Curvature of Space", *General Relativity and Gravitation*, **31**, 1991. [DOI], [ADS]

[9] Kolb, E. W. and Turner, M. S., 1990, *The Early Universe*, Addison-Wesley, Reading, Mass. [ADS]

[10] Lemaître, G., 1927, "Un Univers homogène de masse constante et de rayon croissant rendant compte de la vitesse radiale des nébuleuses extra-galactiques", *Annales de la Societe Scietifique de Bruxelles*, **47**, 49–59. [ADS]

[11] Hubble, E., 1929, "A Relation between Distance and Radial Velocity among Extra-Galactic Nebulae", *Proceedings of the National Academy of Science*, **15**, 168–173. [DOI], [ADS]

[12] Ade, P. A. R. *et al.*, 2013, "Planck 2013 results. XVI. Cosmological parameters", *ArXiv e-prints*. [ADS], [arXiv:1303.5076 [astro-ph.CO]]

[13] Gamow, G., 1946, "Expanding Universe and the Origin of Elements", *Physical Review*, **70**, 572–573. [DOI], [ADS]

[14] Alpher, R. A., Bethe, H. and Gamow, G., 1948, "The Origin of Chemical Elements", *Physical Review*, **73**, 803–804. [DOI], [ADS]

[15] Alpher, R. A. and Herman, R. C., 1950, "Theory of the Origin and Relative Abundance Distribution of the Elements", *Reviews of Modern Physics*, **22**, 153–212. [DOI], [ADS]

[16] Alpher, R. A., Follin, J. W. and Herman, R. C., 1953, "Physical Conditions in the Initial Stages of the Expanding Universe", *Physical Review*, **92**, 1347–1361. [DOI], [ADS]

[17] Peebles, P. J., 1966, "Primeval Helium Abundance and the Primeval Fireball", *Physical Review Letters*, **16**, 410–413. [DOI], [ADS]

[18] Peebles, P. J. E., 1966, "Primordial Helium Abundance and the Primordial Fireball. II", ApJ, **146**, 542. [DOI], [ADS]

[19] Sarkar, S., 1996, "Big bang nucleosynthesis and physics beyond the standard model", *Reports on Progress in Physics*, **59**, 1493–1609. [DOI], [ADS], [arXiv:hep-ph/9602260]

[20] Fields, B. and Sarkar, S., 2006, "Big-Bang nucleosynthesis (Particle Data Group mini-review)", *ArXiv Astrophysics e-prints*. [ADS], [arXiv:astro-ph/0601514]

[21] Gondolo, P. and Gelmini, G., 1991, "Cosmic abundances of stable particles: improved analysis.", *Nuclear Physics B*, **360**, 145–179. [DOI], [ADS]

[22] Olive, K. A. and Skillman, E. D., 2004, "A Realistic Determination of the Error on the Primordial Helium Abundance: Steps toward Nonparametric Nebular Helium Abundances", ApJ, **617**, 29–49. [DOI], [ADS], [arXiv:astro-ph/0405588]

[23] Steigman, G., 2007, "Primordial Nucleosynthesis in the Precision Cosmology Era", *Annual Review of Nuclear and Particle Science*, **57**, 463–491. [DOI], [ADS], [arXiv:0712.1100]

[24] Izotov, Y. I., Chaffee, F. H., Foltz, C. B., Green, R. F., Guseva, N. G. and Thuan, T. X., 1999, "Helium Abundance in the Most Metal-deficient Blue Compact Galaxies: I ZW 18 and SBS 0335-052", ApJ, **527**, 757–777. [DOI], [ADS], [arXiv:astro-ph/9907228]

[25] Peimbert, M., Luridiana, V. and Peimbert, A., 2007, "Revised Primordial Helium Abundance Based on New Atomic Data", ApJ, **666**, 636–646. [DOI], [ADS], [arXiv:astro-ph/0701580]

[26] Epstein, R. I., Lattimer, J. M. and Schramm, D. N., 1976, "The origin of deuterium", Nature, **263**, 198–202. [DOI], [ADS]

[27] Tytler, D., Fan, X.-M. and Burles, S., 1996, "Cosmological baryon density derived from the deuterium abundance at redshift z = 3.57", Nature, **381**, 207–209. [DOI], [ADS], [arXiv:astro-ph/9603069]

[28] Kirkman, D., Tytler, D., Suzuki, N., O'Meara, J. M. and Lubin, D., 2003, "The Cosmological Baryon Density from the Deuterium-to-Hydrogen Ratio in QSO Absorption Systems: D/H toward Q1243+3047", ApJS, **149**, 1–28. [DOI], [ADS], [arXiv:astro-ph/0302006]

[29] Padmanabhan, T., 1993, *Structure Formation in the Universe*. [ADS]

[30] Peebles, P. J. E., 1968, "Recombination of the Primeval Plasma", ApJ, **153**, 1. [DOI], [ADS]

[31] Zel'dovich, Y. B., Kurt, V. G. and Syunyaev, R. A., 1969, "Recombination of Hydrogen in the Hot Model of the Universe", *Soviet Journal of Experimental and Theoretical Physics*, **28**, 146. [ADS]

[32] Penzias, A. A. and Wilson, R. W., 1965, "A Measurement of Excess Antenna Temperature at 4080 Mc/s.", ApJ, **142**, 419–421. [DOI], [ADS]

[33] Dicke, R. H., Peebles, P. J. E., Roll, P. G. and Wilkinson, D. T., 1965, "Cosmic Black-Body Radiation.", ApJ, **142**, 414–419. [DOI], [ADS]

[34] Hu, W. and Dodelson, S., 2002, "Cosmic Microwave Background Anisotropies", ARA&A, **40**, 171–216. [DOI], [ADS], [arXiv:astro-ph/0110414]

[35] Sachs, R. K. and Wolfe, A. M., 1967, "Perturbations of a Cosmological Model and Angular Variations of the Microwave Background", ApJ, **147**, 73. [DOI], [ADS]

[36] Peebles, P. J. E. and Yu, J. T., 1970, "Primeval Adiabatic Perturbation in an Expanding Universe", ApJ, **162**, 815. [DOI], [ADS]

[37] Smoot, G. F. *et al.*, 1992, "Structure in the COBE differential microwave radiometer first-year maps", ApJ, **396**, L1–L5. [DOI], [ADS]

[38] Komatsu, E. *et al.*, 2011, "Seven-year Wilkinson Microwave Anisotropy Probe (WMAP) Observations: Cosmological Interpretation", ApJS, **192**, 18. [DOI], [ADS], [arXiv:1001.4538 [astro-ph.CO]]

[39] Story, K. T. *et al.*, 2012, "A Measurement of the Cosmic Microwave Background Damping Tail from the 2500-square-degree SPT-SZ survey", *ArXiv e-prints*. [ADS], [arXiv:1210.7231 [astro-ph.CO]]

[40] Sievers, J. L. *et al.*, 2013, "The Atacama Cosmology Telescope: Cosmological parameters from three seasons of data", *ArXiv e-prints*. [ADS], [arXiv:1301.0824 [astro-ph.CO]]

[41] Dodelson, S., 2003, *Modern cosmology*. [ADS]

[42] Zwicky, F., 1933, "Die Rotverschiebung von extragalaktischen Nebeln", *Helvetica Physica Acta*, **6**, 110–127. [ADS]

[43] Zwicky, F., 1937, "On the Masses of Nebulae and of Clusters of Nebulae", ApJ, **86**, 217. [DOI], [ADS]

[44] Oort, J. H., 1932, "The force exerted by the stellar system in the direction perpendicular to the galactic plane and some related problems", Bull. Astron. Inst. Netherlands, **6**, 249. [ADS]

[45] Kahn, F. D. and Woltjer, L., 1959, "Intergalactic Matter and the Galaxy.", ApJ, **130**, 705. [DOI], [ADS]

[46] Sofue, Y. and Rubin, V., 2001, "Rotation Curves of Spiral Galaxies", ARA&A, **39**, 137–174. [DOI], [ADS], [arXiv:astro-ph/0010594]

[47] Clowe, D., Gonzalez, A. and Markevitch, M., 2004, "Weak-Lensing Mass Reconstruction of the Interacting Cluster 1E 0657-558: Direct Evidence for the Existence of Dark Matter", ApJ, **604**, 596–603. [DOI], [ADS], [arXiv:astro-ph/0312273]

[48] Clowe, D., Bradač, M., Gonzalez, A. H., Markevitch, M., Randall, S. W., Jones, C. and Zaritsky, D., 2006, "A Direct Empirical Proof of the Existence of Dark Matter", ApJ, **648**, L109–L113. [DOI], [ADS], [arXiv:astro-ph/0608407]

[49] Bradač, M., Allen, S. W., Treu, T., Ebeling, H., Massey, R., Morris, R. G., von der Linden, A. and Applegate, D., 2008, "Revealing the Properties of Dark Matter in the Merging Cluster MACS J0025.4-1222", ApJ, **687**, 959–967. [DOI], [ADS], [arXiv:0806.2320]

[50] Bahcall, N. A. and Fan, X., 1998, "The Most Massive Distant Clusters: Determining Omega and delta 8", ApJ, **504**, 1. [DOI], [ADS], [arXiv:astro-ph/9803277]

[51] Carlberg, R. G., Yee, H. K. C., Morris, S. L., Lin, H., Ellingson, E., Patton, D., Sawicki, M. and Shepherd, C. W., 1999, "The Omega_M-Omega_Lambda Dependence of the Apparent Cluster Omega", ApJ, **516**, 552–558. [DOI], [ADS]

[52] Kashlinsky, A., 1998, "Determining Omega from the cluster correlation function", Phys. Rep., **307**, 67. [DOI], [ADS], [arXiv:astro-ph/9806236]

[53] Tyson, J. A., Kochanski, G. P. and dell'Antonio, I. P., 1998, "Detailed Mass Map of CL 0024+1654 from Strong Lensing", ApJ, **498**, L107. [DOI], [ADS], [arXiv:astro-ph/9801193]

[54] Cen, R., Miralda-Escudé, J., Ostriker, J. P. and Rauch, M., 1994, "Gravitational collapse of small-scale structure as the origin of the Lyman-alpha forest", ApJ, **437**, L9–L12. [DOI], [ADS], [arXiv:astro-ph/9409017]

[55] Hernquist, L., Katz, N., Weinberg, D. H. and Miralda-Escudé, J., 1996, "The Lyman-Alpha Forest in the Cold Dark Matter Model", ApJ, **457**, L51. [DOI], [ADS], [arXiv:astro-ph/9509105]

[56] Dalcanton, J. J. and Hogan, C. J., 2001, "Halo Cores and Phase-Space Densities: Observational Constraints on Dark Matter Physics and Structure Formation", ApJ, **561**, 35–45. [DOI], [ADS], [arXiv:astro-ph/0004381]

[57] Viel, M., Becker, G. D., Bolton, J. S., Haehnelt, M. G., Rauch, M. and Sargent, W. L. W., 2008, "How Cold Is Cold Dark Matter? Small-Scales Constraints from the Flux Power Spectrum of the High-Redshift Lyman-α Forest", *Physical Review Letters*, **100**(4), 041 304. [DOI], [ADS], [arXiv:0709.0131]

[58] Navarro, J. F., Frenk, C. S. and White, S. D. M., 1997, "A Universal Density Profile from Hierarchical Clustering", ApJ, **490**, 493. [DOI], [ADS], [arXiv:astro-ph/9611107]

[59] Colín, P., Avila-Reese, V. and Valenzuela, O., 2000, "Substructure and Halo Density Profiles in a Warm Dark Matter Cosmology", ApJ, **542**, 622–630. [DOI], [ADS], [arXiv:astro-ph/0004115]

[60] Bode, P., Ostriker, J. P. and Turok, N., 2001, "Halo Formation in Warm Dark Matter Models", ApJ, **556**, 93–107. [DOI], [ADS], [arXiv:astro-ph/0010389]

[61] Viel, M., Lesgourgues, J., Haehnelt, M. G., Matarrese, S. and Riotto, A., 2005, "Constraining warm dark matter candidates including sterile neutrinos and light gravitinos with WMAP and the Lyman-α forest", Phys. Rev. D, **71** (6), 063 534. [DOI], [ADS], [arXiv:astro-ph/0501562]

[62] Abazajian, K., 2006, "Linear cosmological structure limits on warm dark matter", Phys. Rev. D, **73**(6), 063 513. [DOI], [ADS], [arXiv:astro-ph/0512631]

[63] Boyarsky, A., Lesgourgues, J., Ruchayskiy, O. and Viel, M., 2009, "Lyman-α constraints on warm and on warm-plus-cold dark matter models", J. Cosmology Astropart. Phys., **5**, 12. [DOI], [ADS], [arXiv:0812.0010]

[64] Narayanan, V. K., Spergel, D. N., Davé, R. and Ma, C.-P., 2000, "Lyman-alpha Forest Constraints on the Mass of Warm Dark Matter and the Shape of the Linear Power Spectrum", *ArXiv Astrophysics e-prints*. [ADS], [arXiv:astro-ph/0005095]

[65] Barkana, R., Haiman, Z. and Ostriker, J. P., 2001, "Constraints on Warm Dark Matter from Cosmological Reionization", ApJ, **558**, 482–496. [DOI], [ADS], [arXiv:astro-ph/0102304]

[66] Martin, S. P., 1998, "A Supersymmetry Primer", in *Perspectives on Supersymmetry*, (Ed.) Kane, G. L., [ADS], [arXiv:hep-ph/9709356]

[67] CMS Collaboration Chatrchyan, S. *et al.*, 2012, "Observation of a new boson at a mass of 125 GeV with the CMS experiment at the LHC", *Physics Letters B*, **716**, 30–61. [DOI], [ADS], [arXiv:1207.7235 [hep-ex]]

[68] ATLAS Collaboration Aad, G. *et al.*, 2012, "Observation of a new particle in the search for the Standard Model Higgs boson with the ATLAS detector at the LHC", *Physics Letters B*, **716**, 1–29. [DOI], [ADS], [arXiv:1207.7214 [hep-ex]]

[69] Jungman, G., Kamionkowski, M. and Griest, K., 1996, "Supersymmetric dark matter", Phys. Rep., **267**, 195–373. [DOI], [ADS], [arXiv:hep-ph/9506380]

[70] Farrar, G. R. and Fayet, P., 1978, "Phenomenology of the production, decay, and detection of new hadronic states associated with supersymmetry", *Physics Letters B*, **76**, 575–579. [DOI], [ADS]

[71] Weinberg, S., 1982, "Supersymmetry at ordinary energies. Masses and conservation laws", Phys. Rev. D, **26**, 287–302. [DOI], [ADS]

[72] Bertone, G., Hooper, D. and Silk, J., 2005, "Particle dark matter: evidence, candidates and constraints", Phys. Rep., **405**, 279–390. [DOI], [ADS], [arXiv:hep-ph/0404175]

[73] Zel'dovich, Ya B, 1965, "Advances in Astronomy and Astrophysics", vol. 3, p. 242. Academic Press

[74] Zeldovic, Y. B., Okun, L. B. and Pikelner, S. B., 1965, "Quarks, astrophysical and physico-chemical aspects", *Physics Letters*, **17**, 164–166. [DOI], [ADS]

[75] Chiu, H.-Y., 1966, "Symmetry Between Particle and Antiparticle Populations in the Universe", *Physical Review Letters*, **17**, 712–714. [DOI], [ADS]

[76] Lee, B. W. and Weinberg, S., 1977, "Cosmological lower bound on heavy-neutrino masses", *Phys. Rev. Lett.*, **39**, 165–168. [DOI], [ADS]

[77] Hut, P., 1977, "Limits on masses and number of neutral weakly interacting particles", *Physics Letters A*, **69**, 85–88. [ADS]

[78] Wolfram, S., 1979, "Abundances of new stable particles produced in the early universe", *Physics Letters B*, **82**, 65–68. [DOI], [ADS]

[79] Steigman, G., 1979, "Cosmology confronts particle physics.", *Annual Review of Nuclear and Particle Science*, **29**, 313–338. [DOI], [ADS]

[80] Bernstein, J., Brown, L. S. and Feinberg, G., 1985, "Cosmological heavy-neutrino problem", Phys. Rev. D, **32**, 3261–3267. [DOI], [ADS]

[81] Scherrer, R. J. and Turner, M. S., 1986, "On the relic, cosmic abundance of stable, weakly interacting massive particles", Phys. Rev. D, **33**, 1585–1589. [DOI], [ADS]

[82] Scherrer, R. J. and Turner, M. S., 1986, "Erratum: On the relic, cosmic abundance of stable, weakly interacting massive particles [Phys. Rev. D 33, 1585 (1986)]", Phys. Rev. D, **34**, 3263. [DOI], [ADS]

[83] Srednicki, M., Watkins, R. and Olive, K. A., 1988, "Calculations of relic densities in the early universe", *Nuclear Physics B*, **310**, 693–713. [DOI], [ADS]

[84] Steigman, G., Dasgupta, B. and Beacom, J. F., 2012, "Precise relic WIMP abundance and its impact on searches for dark matter annihilation", Phys. Rev. D, **86**(2), 023 506. [DOI], [ADS], [arXiv:1204.3622 [hep-ph]]

[85] Laine, M. and Schröder, Y., 2006, "Quark mass thresholds in QCD thermodynamics", Phys. Rev. D, **73**(8), 085 009. [DOI], [ADS], [arXiv:hep-ph/0603048]

[86] Bergström, L. and Goobar, A., 1999, *Cosmology and particle astrophysics.*. [ADS]

[87] Fixsen, D. J., 2009, "The Temperature of the Cosmic Microwave Background", ApJ, **707**, 916–920. [DOI], [ADS], [arXiv:0911.1955 [astro-ph.CO]]

[88] Bonometto, S. A. and Pantano, O., 1993, "Physics of the cosmological quark-hadron transition.", Phys. Rep., **228**, 175–252. [DOI], [ADS]

[89] Peebles, P. J. E., 1980, *The large-scale structure of the universe*. [ADS]

[90] Cirelli, M. *et al.*, 2011, "PPPC 4 DM ID: a poor particle physicist cookbook for dark matter indirect detection", J. Cosmology Astropart. Phys., **3**, 51. [DOI], [ADS], [arXiv:1012.4515 [hep-ph]]

[91] Adriani, O. *et al.*, 2010, "PAMELA Results on the Cosmic-Ray Antiproton Flux from 60 MeV to 180 GeV in Kinetic Energy", *Physical Review Letters*, **105**(12), 121 101. [DOI], [ADS], [arXiv:1007.0821 [astro-ph.HE]]

[92] Donato, F., Maurin, D., Salati, P., Barrau, A., Boudoul, G. and Taillet, R., 2001, "Antiprotons from Spallations of Cosmic Rays on Interstellar Matter", ApJ, **563**, 172–184. [DOI], [ADS], [arXiv:astro-ph/0103150]

[93] Gaisser, T. K. and Levy, E. H., 1974, "Astrophysical implications of cosmic-ray antiprotons", Phys. Rev. D, **10**, 1731–1735. [DOI], [ADS]

[94] Adriani, O. *et al.*, 2009, "New Measurement of the Antiproton-to-Proton Flux Ratio up to 100 GeV in the Cosmic Radiation", *Physical Review Letters*, **102** (5), 051 101. [DOI], [ADS], [arXiv:0810.4994]

[95] Donato, F., Maurin, D., Brun, P., Delahaye, T. and Salati, P., 2009, "Constraints on WIMP Dark Matter from the High Energy PAMELA $\bar{p}/p$ Data", *Physical Review Letters*, **102**(7), 071 301. [DOI], [ADS], [arXiv:0810.5292]

[96] Scholberg, K., 2005, "Indirect dark matter searches with AMS-02", *Nuclear Physics B Proceedings Supplements*, **138**, 35–37. [DOI], [ADS]

[97] Hooper, D. and Baltz, E. A., 2008, "Strategies for Determining the Nature of Dark Matter", *Annual Review of Nuclear and Particle Science*, **58**, 293–314. [DOI], [ADS], [arXiv:0802.0702 [hep-ph]]

[98] Porter, T. A., Johnson, R. P. and Graham, P. W., 2011, "Dark Matter Searches with Astroparticle Data", ARA&A, **49**, 155–194. [DOI], [ADS], [arXiv:1104.2836 [astro-ph.HE]]

[99] Moskalenko, I. V. and Strong, A. W., 1998, "Production and Propagation of Cosmic-Ray Positrons and Electrons", ApJ, **493**, 694. [DOI], [ADS], [arXiv:astro-ph/9710124]

[100] Adriani, O. *et al.*, 2009, "An anomalous positron abundance in cosmic rays with energies 1.5-100GeV", Nature, **458**, 607–609. [DOI], [ADS], [arXiv:0810.4995]

[101] Atwood, W. B., Abdo, A. A., Ackermann, M., Althouse, W., Anderson, B., Axelsson, M., Baldini, L., Ballet, J., Band, D. L. and et al., 2009, "The Large Area Telescope on the Fermi Gamma-Ray Space Telescope Mission", ApJ, **697**, 1071–1102. [DOI], [ADS], [arXiv:0902.1089 [astro-ph.IM]]

[102] Ackermann, M. *et al.*, 2012, "Measurement of Separate Cosmic-Ray Electron and Positron Spectra with the Fermi Large Area Telescope", *Physical Review Letters*, **108**(1), 011 103. [DOI], [ADS], [arXiv:1109.0521 [astro-ph.HE]]

[103] Aguilar, M. *et al.*, 2013, "First Result from the Alpha Magnetic Spectrometer on the International Space Station: Precision Measurement of the Positron Fraction in Primary Cosmic Rays of 0.5–350 GeV", *Physical Review Letters*, **110**(14), 141 102. [DOI], [ADS]

[104] Arkani-Hamed, N., Finkbeiner, D. P., Slatyer, T. R. and Weiner, N., 2009, "A theory of dark matter", Phys. Rev. D, **79**(1), 015 014. [DOI], [ADS], [arXiv:0810.0713 [hep-ph]]

[105] Chang, J. *et al.*, 2008, "An excess of cosmic ray electrons at energies of 300-800GeV", Nature, **456**, 362–365. [DOI], [ADS]

[106] Torii, S. *et al.*, 2008, "High-energy electron observations by PPB-BETS flight in Antarctica", *ArXiv e-prints*. [ADS], [arXiv:0809.0760]

[107] Abdo, A. A. *et al.*, 2009, "Measurement of the Cosmic Ray e^++e^- Spectrum from 20GeV to 1TeV with the Fermi Large Area Telescope", *Physical Review Letters*, **102**(18), 181 101. [DOI], [ADS], [arXiv:0905.0025 [astro-ph.HE]]

[108] Malyshev, D., Cholis, I. and Gelfand, J., 2009, "Pulsars versus dark matter interpretation of ATIC/PAMELA", Phys. Rev. D, **80**(6), 063 005. [DOI], [ADS], [arXiv:0903.1310 [astro-ph.HE]]

[109] Linden, T. and Profumo, S., 2013, "Probing the Pulsar Origin of the Anomalous Positron Fraction with AMS-02 and Atmospheric Cherenkov Telescopes", *ArXiv e-prints*. [ADS], [arXiv:1304.1791 [astro-ph.HE]]

[110] Beacom, J. F., Bell, N. F. and Mack, G. D., 2007, "Upper Bound on the Dark Matter Total Annihilation Cross Section", *Physical Review Letters*, **99**(23), 231 301–+. [DOI], [ADS], [arXiv:astro-ph/0608090]

[111] Abbasi, R. *et al.*, 2011, "Search for dark matter from the Galactic halo with the IceCube Neutrino Telescope", Phys. Rev. D, **84**(2), 022 004. [DOI], [ADS], [arXiv:1101.3349 [astro-ph.HE]]

[112] Hooper, D. and Goodenough, L., 2011, "Dark matter annihilation in the Galactic Center as seen by the Fermi Gamma Ray Space Telescope", *Physics Letters B*, **697**, 412–428. [DOI], [ADS], [arXiv:1010.2752 [hep-ph]]

[113] Hooper, D. and Linden, T., 2011, "Origin of the gamma rays from the Galactic Center", Phys. Rev. D, **84**(12), 123 005. [DOI], [ADS], [arXiv:1110.0006 [astro-ph.HE]]

[114] Abazajian, K. N. and Kaplinghat, M., 2012, "Detection of a gamma-ray source in the Galactic Center consistent with extended emission from dark matter annihilation and concentrated astrophysical emission", Phys. Rev. D, **86**(8), 083 511. [DOI], [ADS], [arXiv:1207.6047 [astro-ph.HE]]

[115] Cesarini, A., Fucito, F., Lionetto, A., Morselli, A. and Ullio, P., 2004, "The Galactic center as a dark matter gamma-ray source", *Astroparticle Physics*, **21**, 267–285. [DOI], [ADS], [arXiv:astro-ph/0305075]

[116] Abazajian, K. N., 2011, "The consistency of Fermi-LAT observations of the galactic center with a millisecond pulsar population in the central stellar cluster", J. Cosmology Astropart. Phys., **3**, 10–+. [DOI], [ADS], [arXiv:1011.4275 [astro-ph.HE]]

[117] Boyarsky, A., Malyshev, D. and Ruchayskiy, O., 2011, "A comment on the emission from the Galactic Center as seen by the Fermi telescope", *Physics Letters B*, **705**, 165–169. [DOI], [ADS], [arXiv:1012.5839 [hep-ph]]

[118] Ackermann, M. *et al.*, 2011, "Constraining Dark Matter Models from a Combined Analysis of Milky Way Satellites with the Fermi Large Area Telescope", *Physical Review Letters*, **107**(24), 241 302. [DOI], [ADS], [arXiv:1108.3546 [astro-ph.HE]]

[119] Ackermann, M. *et al.*, 2012, "Constraints on the Galactic Halo Dark Matter from Fermi-LAT Diffuse Measurements", ApJ, **761**, 91. [DOI], [ADS], [arXiv:1205.6474 [astro-ph.CO]]

[120] Ackermann, M. *et al.*, 2010, "Constraints on dark matter annihilation in clusters of galaxies with the Fermi large area telescope", J. Cosmology Astropart. Phys., **5**, 25. [DOI], [ADS], [arXiv:1002.2239 [astro-ph.CO]]

[121] Ando, S. and Nagai, D., 2012, "Fermi-LAT constraints on dark matter annihilation cross section from observations of the Fornax cluster", J. Cosmology Astropart. Phys., **7**, 17. [DOI], [ADS], [arXiv:1201.0753 [astro-ph.HE]]

[122] Arlen, T. *et al.*, 2012, "Constraints on Cosmic Rays, Magnetic Fields, and Dark Matter from Gamma-Ray Observations of the Coma Cluster of Galaxies with VERITAS and Fermi", ApJ, **757**, 123. [DOI], [ADS], [arXiv:1208.0676 [astro-ph.HE]]

[123] Han, J., Frenk, C. S., Eke, V. R., Gao, L., White, S. D. M., Boyarsky, A., Malyshev, D. and Ruchayskiy, O., 2012, "Constraining extended gamma-ray emission from galaxy clusters", MNRAS, **427**, 1651–1665. [DOI], [ADS], [arXiv:1207.6749 [astro-ph.CO]]

[124] Nezri, E., White, R., Combet, C., Hinton, J. A., Maurin, D. and Pointecouteau, E., 2012, "γ -rays from annihilating dark matter in galaxy clusters: stacking versus single source analysis", MNRAS, **425**, 477–489. [DOI], [ADS], [arXiv:1203.1165 [astro-ph.HE]]

[125] Abramowski, A. *et al.*, 2012, "Search for Dark Matter Annihilation Signals from the Fornax Galaxy Cluster with H.E.S.S.", ApJ, **750**, 123. [DOI], [ADS], [arXiv:1202.5494 [astro-ph.HE]]

[126] Huang, X., Vertongen, G. and Weniger, C., 2012, "Probing dark matter decay and annihilation with Fermi LAT observations of nearby galaxy clusters", J. Cosmology Astropart. Phys., **1**, 42. [DOI], [ADS], [arXiv:1110.1529 [hep-ph]]

[127] Abdo, A. A. *et al.*, 2010, "Spectrum of the Isotropic Diffuse Gamma-Ray Emission Derived from First-Year Fermi Large Area Telescope Data", *Physical Review Letters*, **104**(10), 101 101–+. [DOI], [ADS], [arXiv:1002.3603 [astro-ph.HE]]

[128] Abdo, A. A. *et al.*, 2010, "Constraints on cosmological dark matter annihilation from the Fermi-LAT isotropic diffuse gamma-ray measurement", J. Cosmology Astropart. Phys., **4**, 14. [DOI], [ADS], [arXiv:1002.4415 [astro-ph.CO]]

[129] Abazajian, K. N., Blanchet, S. and Harding, J. P., 2012, "Current and future constraints on dark matter from prompt and inverse-Compton photon emission in the isotropic diffuse gamma-ray background", Phys. Rev. D, **85**(4), 043 509. [DOI], [ADS], [arXiv:1011.5090 [hep-ph]]

[130] Abazajian, K. N., Agrawal, P., Chacko, Z. and Kilic, C., 2010, "Conservative constraints on dark matter from the Fermi-LAT isotropic diffuse gamma-ray background spectrum", J. Cosmology Astropart. Phys., **11**, 41–+. [DOI], [ADS], [arXiv:1002.3820 [astro-ph.HE]]

[131] Rieger, F. M., de Ona-Wilhelmi, E. and Aharonian, F. A., 2013, "TeV Astronomy", *ArXiv e-prints*. [ADS], [arXiv:1302.5603 [astro-ph.HE]]

[132] Weekes, T. C. *et al.*, 2002, "VERITAS: the Very Energetic Radiation Imaging Telescope Array System", *Astroparticle Physics*, **17**, 221–243. [DOI], [ADS], [arXiv:astro-ph/0108478]

[133] Baixeras, C., 2003, "The MAGIC telescope", *Nuclear Physics B Proceedings Supplements*, **114**, 247–252. [DOI], [ADS]

[134] Aharonian, F. *et al.*, 2006, "Observations of the Crab nebula with HESS", A&A, **457**, 899–915. [DOI], [ADS], [arXiv:astro-ph/0607333]

[135] Actis, M. *et al.*, 2011, "Design concepts for the Cherenkov Telescope Array CTA: an advanced facility for ground-based high-energy gamma-ray astronomy", *Experimental Astronomy*, **32**, 193–316. [DOI], [ADS], [arXiv:1008.3703 [astro-ph.IM]]

[136] Goodman, M. W. and Witten, E., 1985, "Detectability of certain dark-matter candidates", Phys. Rev. D, **31**, 3059–3063. [DOI], [ADS]

[137] Kamionkowski, M. and Koushiappas, S. M., 2008, "Galactic substructure and direct detection of dark matter", Phys. Rev. D, **77**(10), 103 509. [DOI], [ADS], [arXiv:0801.3269]

[138] Kamionkowski, M., Koushiappas, S. M. and Kuhlen, M., 2010, "Galactic substructure and dark-matter annihilation in the Milky Way halo", Phys. Rev. D, **81**(4), 043 532–+. [DOI], [ADS], [arXiv:1001.3144 [astro-ph.GA]]

[139] Freese, K., Lisanti, M. and Savage, C., 2012, "Annual Modulation of Dark Matter: A Review", *ArXiv e-prints*. [ADS], [arXiv:1209.3339 [astro-ph.CO]]

[140] Bernabei, R. *et al.*, 2010, "New results from DAMA/LIBRA", *European Physical Journal C*, **67**, 39–49. [DOI], [ADS], [arXiv:1002.1028 [astro-ph.GA]]

[141] Aprile, E. *et al.*, 2012, "Dark Matter Results from 225 Live Days of XENON100 Data", *Physical Review Letters*, **109**(18), 181 301. [DOI], [ADS], [arXiv:1207.5988 [astro-ph.CO]]

[142] Angloher, G. *et al.*, 2012, "Results from 730 kg days of the CRESST-II Dark Matter search", *European Physical Journal C*, **72**, 1971. [DOI], [ADS], [arXiv:1109.0702 [astro-ph.CO]]

[143] Aalseth, C. E. *et al.*, 2011, "Results from a Search for Light-Mass Dark Matter with a p-Type Point Contact Germanium Detector", *Physical Review Letters*, **106**(13), 131 301. [DOI], [ADS], [arXiv:1002.4703 [astro-ph.CO]]

[144] Feng, J. L., Kumar, J., Marfatia, D. and Sanford, D., 2011, "Isospin-violating dark matter", *Physics Letters B*, **703**, 124–127. [DOI], [ADS], [arXiv:1102.4331 [hep-ph]]

[145] CDMS Collaboration *et al.*, 2013, "Dark Matter Search Results Using the Silicon Detectors of CDMS II", *ArXiv e-prints*. [ADS], [arXiv:1304.4279 [hep-ex]]

[146] McKinsey, D. N. *et al.*, 2010, "The LUX dark matter search", *Journal of Physics Conference Series*, **203**(1), 012 026. [DOI], [ADS]

[147] Malling, D. C. *et al.*, 2011, "After LUX: The LZ Program", *ArXiv e-prints*. [ADS], [arXiv:1110.0103 [astro-ph.IM]]

[148] Akerib, D. S. *et al.*, 2008, "Present Status of the SuperCDMS program", *Journal of Low Temperature Physics*, **151**, 818–823. [DOI], [ADS]

[149] Aprile, E. and XENON1T collaboration, 2012, "The XENON1T Dark Matter Search Experiment", *ArXiv e-prints*. [ADS], [arXiv:1206.6288 [astro-ph.IM]]

[150] Marchionni, A. *et al.*, 2011, "ArDM: a ton-scale LAr detector for direct Dark Matter searches", *Journal of Physics Conference Series*, **308**(1), 012 006. [DOI], [ADS], [arXiv:1012.5967 [physics.ins-det]]

[151] Boulay, M. G. and DEAP Collaboration, 2012, "DEAP-3600 Dark Matter Search at SNOLAB", *Journal of Physics Conference Series*, **375**(1), 012 027. [DOI], [ADS], [arXiv:1203.0604 [astro-ph.IM]]

[152] Abbasi, R. *et al.*, 2012, "Multiyear search for dark matter annihilations in the Sun with the AMANDA-II and IceCube detectors", Phys. Rev. D, **85**(4), 042 002. [DOI], [ADS], [arXiv:1112.1840 [astro-ph.HE]]

[153] Chatrchyan, S. *et al.*, 2012, "Search for Dark Matter and Large Extra Dimensions in pp Collisions Yielding a Photon and Missing Transverse Energy", *Physical Review Letters*, **108**(26), 261 803. [DOI], [ADS], [arXiv:1204.0821 [hep-ex]]

[154] Aad, G. *et al.*, 2013, "Search for Dark Matter Candidates and Large Extra Dimensions in Events with a Photon and Missing Transverse Momentum in pp Collision Data at s=7TeV with the ATLAS Detector", *Physical Review Letters*, **110**(1), 011 802. [DOI], [ADS], [arXiv:1209.4625 [hep-ex]]

[155] Walker, M. G., 2012, "Dark Matter in the Milky Way's Dwarf Spheroidal Satellites", *ArXiv e-prints*. [ADS], [arXiv:1205.0311 [astro-ph.CO]]

[156] Strigari, L. E., 2012, "Galactic Searches for Dark Matter", *ArXiv e-prints*. [ADS], [arXiv:1211.7090 [astro-ph.CO]]

[157] Strigari, L. E., Koushiappas, S. M., Bullock, J. S. and Kaplinghat, M., 2007, "Precise constraints on the dark matter content of MilkyWay dwarf galaxies for gamma-ray experiments", Phys. Rev. D, **75**(8), 083 526–+. [DOI], [ADS], [arXiv:astro-ph/0611925]

[158] Strigari, L. E., Koushiappas, S. M., Bullock, J. S., Kaplinghat, M., Simon, J. D., Geha, M. and Willman, B., 2008, "The Most Dark-Matter-dominated Galaxies: Predicted Gamma-Ray Signals from the Faintest Milky Way Dwarfs", ApJ, **678**, 614–620. [DOI], [ADS], [arXiv:0709.1510]

[159] Martinez, G. D., Bullock, J. S., Kaplinghat, M., Strigari, L. E. and Trotta, R., 2009, "Indirect Dark Matter detection from Dwarf satellites: joint expectations from astrophysics and supersymmetry", J. Cosmology Astropart. Phys., **6**, 14. [DOI], [ADS], [arXiv:0902.4715 [astro-ph.HE]]

[160] Abdo, A. A. *et al.*, 2010, "The Fermi-LAT High-Latitude Survey: Source Count Distributions and the Origin of the Extragalactic Diffuse Background", ApJ, **720**, 435–453. [DOI], [ADS], [arXiv:1003.0895 [astro-ph.CO]]

[161] Abdo, A. A. *et al.*, 2010, "Observations of Milky Way Dwarf Spheroidal Galaxies with the Fermi-Large Area Telescope Detector and Constraints on Dark Matter Models", ApJ, **712**, 147–158. [DOI], [ADS], [arXiv:1001.4531 [astro-ph.CO]]

[162] Llena Garde, M., 2011, "Constraining dark matter signal from a combined analysis of Milky Way satellites using the Fermi-LAT", *ArXiv e-prints*. [ADS], [arXiv:1102.5701 [astro-ph.HE]]

[163] Garde, M. L. and Fermi-LAT Collaboration, 2011. URL: http://fermi.gsfc.nasa.gov/science/symposium/2011/program/session9/LlenaGarde_FermiSymp.pdf

[164] Charbonnier, A. *et al.*, 2011, "Dark matter profiles and annihilation in dwarf spheroidal galaxies: prospectives for present and future γ-ray observatories - I. The classical dwarf spheroidal galaxies", MNRAS, **418**, 1526–1556. [DOI], [ADS], [arXiv:1104.0412 [astro-ph.HE]]

[165] Fermi-LAT Collaboration, 2011. URL: http://fermi.gsfc.nasa.gov/ssc/data/

[166] Fermi Science Support Center, 2011. URL: http://fermi.gsfc.nasa.gov/ssc/data/access/lat/2yr_catalog/2FGL_catalog_draft_v4.2nl.pdf

[167] Stuart, Alan and Ord, Keith J., 1987, *Kendall's advanced theory of statistics*, Oxford University Press, New York, 5th edn.

[168] Feldman, G. J. and Cousins, R. D., 1998, "Unified approach to the classical statistical analysis of small signals", Phys. Rev. D, **57**, 3873–3889. [DOI], [ADS], [arXiv:physics/9711021]

[169] Neyman, J., 1937, "Outline of a Theory of Statistical Estimation Based on the Classical Theory of Probability", *Royal Society of London Philosophical Transactions Series A*, **236**, 333–380. [DOI], [ADS]

[170] Sutton, P. J., 2009, "Upper limits from counting experiments with multiple pipelines", *Classical and Quantum Gravity*, **26**(24), 245 007–+. [DOI], [ADS], [arXiv:0905.4089 [physics.data-an]]

[171] Gondolo, P., Edsjö, J., Ullio, P., Bergström, L., Schelke, M. and Baltz, E. A., 2004, "DarkSUSY: computing supersymmetric dark matter properties numerically", J. Cosmology Astropart. Phys., **7**, 8–+. [DOI], [ADS], [arXiv:astro-ph/0406204]

[172] Gondolo, P., Edsjö, J., Ullio, P., Bergström, L., Schelke, M., Baltz, E. A., Bringmann, T. and Duda, G., 2011. URL: http://www.darksusy.org

[173] Neyman, J. and Pearson, E. S., 1933, "On the Problem of the Most Efficient Tests of Statistical Hypotheses", *Philosophical Transactions of the Royal Society of London. Series A, Containing Papers of a Mathematical or Physical Character*, **231**, pp. 289–337, ISSN 02643952URL: http://www.jstor.org/stable/91247

[174] Adelson, R. M., 1966, "Compound Poisson Distributions", *OR*, **17**(1), pp. 73–75, ISSN 14732858URL: http://www.jstor.org/stable/3007241

[175] Embrechts, Paul and Frei, Marco, 2009, "Panjer recursion versus FFT for compound distributions", *Mathematical Methods of Operations Research*, **69** (3), 497–508. [DOI]URL: http://dx.doi.org/10.1007/s00186-008-0249-2

[176] Rudaz, S., 1989, "Annihilation of heavy-neutral-fermion pairs into monochromatic γ rays and its astrophysical implications", Phys. Rev. D, **39**, 3549–3556. [DOI], [ADS]

[177] Bergström, L., 1989, "Radiative processes in dark matter photino annihilation", *Physics Letters B*, **225**, 372–380. [DOI], [ADS]

[178] Giudice, G. F. and Griest, K., 1989, "Rate for annihilation of galactic dark matter into two photons", Phys. Rev. D, **40**, 2549–2558. [DOI], [ADS]

[179] Bergström, L. and Kaplan, J., 1994, "Gamma ray lines from TeV dark matter", *Astroparticle Physics*, **2**, 261–268. [DOI], [ADS], [arXiv:hep-ph/9403239]

[180] Jungman, G. and Kamionkowski, M., 1995, "γ rays from neutralino annihilation", Phys. Rev. D, **51**, 3121–3124. [DOI], [ADS], [arXiv:hep-ph/9501365]

[181] Jackson, C. B., Servant, G., Shaughnessy, G., Tait, T. M. P. and Taoso, M., 2010, "Higgs in space!", J. Cosmology Astropart. Phys., **4**, 4. [DOI], [ADS], [arXiv:0912.0004 [hep-ph]]

[182] Weniger, C., 2012, "A tentative gamma-ray line from Dark Matter annihilation at the Fermi Large Area Telescope", J. Cosmology Astropart. Phys., **8**, 7. [DOI], [ADS], [arXiv:1204.2797 [hep-ph]]

[183] Tempel, E., Hektor, A. and Raidal, M., 2012, "Fermi 130 GeV gamma-ray excess and dark matter annihilation in sub-haloes and in the Galactic centre", J. Cosmology Astropart. Phys., **9**, 32. [DOI], [ADS], [arXiv:1205.1045 [hep-ph]]

[184] Su, M. and Finkbeiner, D. P., 2012, "Strong Evidence for Gamma-ray Line Emission from the Inner Galaxy", *ArXiv e-prints*. [ADS], [arXiv:1206.1616 [astro-ph.HE]]

[185] Dudas, E., Mambrini, Y., Pokorski, S. and Romagnoni, A., 2012, "Extra U(1) as natural source of a monochromatic gamma ray line", *Journal of High Energy Physics*, **10**, 123. [DOI], [ADS], [arXiv:1205.1520 [hep-ph]]

[186] Cline, J. M., 2012, "130 GeV dark matter and the Fermi gamma-ray line", Phys. Rev. D, **86**(1), 015 016. [DOI], [ADS], [arXiv:1205.2688 [hep-ph]]

[187] Choi, K.-Y. and Seto, O., 2012, "Dirac right-handed sneutrino dark matter and its signature in the gamma-ray lines", Phys. Rev. D, **86**(4), 043 515. [DOI], [ADS], [arXiv:1205.3276 [hep-ph]]

[188] Kyae, B. and Park, J.-C., 2013, "130 GeV Fermi gamma-ray line from dark matter decay", *Physics Letters B*, **718**, 1425–1429. [DOI], [ADS], [arXiv:1205.4151 [hep-ph]]

[189] Lee, H. M., Park, M. and Park, W.-I., 2012, "Fermi gamma ray line at 130 GeV from axion-mediated dark matter", Phys. Rev. D, **86**(10), 103 502. [DOI], [ADS], [arXiv:1205.4675 [hep-ph]]

[190] Rajaraman, A., Tait, T. M. P. and Whiteson, D., 2012, "Two lines or not two lines? That is the question of gamma ray spectra", J. Cosmology Astropart. Phys., **9**, 3. [DOI], [ADS], [arXiv:1205.4723 [hep-ph]]

[191] Buckley, M. R. and Hooper, D., 2012, "Implications of a 130 GeV gamma-ray line for dark matter", Phys. Rev. D, **86**(4), 043 524. [DOI], [ADS], [arXiv:1205.6811 [hep-ph]]

[192] Profumo, S. and Linden, T., 2012, "Gamma-ray lines in the Fermi data: is it a bubble?", J. Cosmology Astropart. Phys., **7**, 11. [DOI], [ADS], [arXiv:1204.6047 [astro-ph.HE]]

[193] Boyarsky, A., Malyshev, D. and Ruchayskiy, O., 2012, "Spectral and spatial variations of the diffuse gamma-ray background in the vicinity of the Galactic plane and possible nature of the feature at 130 GeV", *ArXiv e-prints*. [ADS], [arXiv:1205.4700 [astro-ph.HE]]

[194] Ackermann, M. *et al.*, 2012, "Fermi LAT search for dark matter in gamma-ray lines and the inclusive photon spectrum", Phys. Rev. D, **86**(2), 022 002. [DOI], [ADS], [arXiv:1205.2739 [astro-ph.HE]]

[195] Bergström, L., Ullio, P. and Buckley, J. H., 1998, "Observability of gamma rays from dark matter neutralino annihilations in the Milky Way halo", *Astroparticle Physics*, **9**, 137–162. [DOI], [ADS], [arXiv:astro-ph/9712318]

[196] Nolan, P. L. *et al.*, 2012, "Fermi Large Area Telescope Second Source Catalog", ApJS, **199**, 31. [DOI], [ADS], [arXiv:1108.1435 [astro-ph.HE]]

[197] 2012. URL: http://www.slac.stanford.edu/exp/glast/groups/canda/lat_Performance.htm

[198] Panjer, Harry H., 1981, "Recursive evaluation of a family of compound distributions", *Astin Bulletin*, **12**, 22–26

[199] Scheuer, P. A. G., 1957, "A statistical method for analysing observations of faint radio stars", *Proceedings of the Cambridge Philosophical Society*, **53**, 764–773. [DOI], [ADS]

[200] Lee, S. K., Ando, S. and Kamionkowski, M., 2009, "The gamma-ray-flux PDF from galactic halo substructure", J. Cosmology Astropart. Phys., **7**, 7–+. [DOI], [ADS], [arXiv:0810.1284]

[201] Baxter, E. J., Dodelson, S., Koushiappas, S. M. and Strigari, L. E., 2010, "Constraining dark matter in galactic substructure", Phys. Rev. D, **82**(12), 123 511–+. [DOI], [ADS], [arXiv:1006.2399 [astro-ph.GA]]

[202] Essig, R., Sehgal, N., Strigari, L. E., Geha, M. and Simon, J. D., 2010, "Indirect dark matter detection limits from the ultrafaint Milky Way satellite Segue 1", Phys. Rev. D, **82**(12), 123 503–+. [DOI], [ADS], [arXiv:1007.4199 [astro-ph.CO]]

[203] Martinez, G. D., Minor, Q. E., Bullock, J., Kaplinghat, M., Simon, J. D. and Geha, M., 2011, "A Complete Spectroscopic Survey of the Milky Way Satellite Segue 1: Dark Matter Content, Stellar Membership, and Binary Properties from a Bayesian Analysis", ApJ, **738**, 55. [DOI], [ADS], [arXiv:1008.4585 [astro-ph.GA]]

[204] Walker, M. G., Combet, C., Hinton, J. A., Maurin, D. and Wilkinson, M. I., 2011, "Dark Matter in the Classical Dwarf Spheroidal Galaxies: A Robust Constraint on the Astrophysical Factor for γ-Ray Flux Calculations", ApJ, **733**, L46. [DOI], [ADS], [arXiv:1104.0411 [astro-ph.HE]]

[205] Bringmann, T., Bergström, L. and Edsjö, J., 2008, "New gamma-ray contributions to supersymmetric dark matter annihilation", *Journal of High Energy Physics*, **1**, 49. [DOI], [ADS], [arXiv:0710.3169 [hep-ph]]

[206] Scott, P., Conrad, J., Edsjö, J., Bergström, L., Farnier, C. and Akrami, Y., 2010, "Direct constraints on minimal supersymmetry from Fermi-LAT observations of the dwarf galaxy Segue 1", J. Cosmology Astropart. Phys., **1**, 31. [DOI], [ADS], [arXiv:0909.3300 [astro-ph.CO]]

[207] Cholis, I. and Salucci, P., 2012, "Extracting limits on dark matter annihilation from gamma ray observations towards dwarf spheroidal galaxies", Phys. Rev. D, **86**(2), 023 528. [DOI], [ADS], [arXiv:1203.2954 [astro-ph.HE]]

[208] Mazziotta, M. N., Loparco, F., de Palma, F. and Giglietto, N., 2012, "A model-independent analysis of the Fermi Large Area Telescope gamma-ray data from the Milky Way dwarf galaxies and halo to constrain dark matter scenarios", *Astroparticle Physics*, **37**, 26–39. [DOI], [ADS], [arXiv:1203.6731 [astro-ph.IM]]

[209] Baushev, A. N., Federici, S. and Pohl, M., 2012, "Spectral analysis of the gamma-ray background near the dwarf Milky Way satellite Segue 1: Improved limits on the cross section of neutralino dark matter annihilation", Phys. Rev. D, **86**(6), 063 521. [DOI], [ADS], [arXiv:1205.3620 [astro-ph.HE]]

[210] Aliu, E. *et al.*, 2012, "VERITAS deep observations of the dwarf spheroidal galaxy Segue 1", Phys. Rev. D, **85**(6), 062 001. [DOI], [ADS], [arXiv:1202.2144 [astro-ph.HE]]

[211] Acciari, V. A. *et al.*, 2010, "VERITAS Search for VHE Gamma-ray Emission from Dwarf Spheroidal Galaxies", ApJ, **720**, 1174–1180. [DOI], [ADS], [arXiv:1006.5955 [astro-ph.CO]]

[212] Ripken, J., Conrad, J. and Scott, P., 2011, "Implications for constrained supersymmetry of combined H.E.S.S. observations of dwarf galaxies, the Galactic halo and the Galactic Centre", J. Cosmology Astropart. Phys., **11**, 4. [DOI], [ADS], [arXiv:1012.3939 [astro-ph.HE]]

[213] H.E.S.S. Collaboration *et al.*, 2011, "H.E.S.S. constraints on dark matter annihilations towards the sculptor and carina dwarf galaxies", *Astroparticle Physics*, **34**, 608–616. [DOI], [ADS], [arXiv:1012.5602 [astro-ph.HE]]

[214] Bringmann, T., Huang, X., Ibarra, A., Vogl, S. and Weniger, C., 2012, "Fermi LAT search for internal bremsstrahlung signatures from dark matter annihilation", J. Cosmology Astropart. Phys., **7**, 54. [DOI], [ADS], [arXiv:1203.1312 [hep-ph]]

[215] Komatsu, E., Dunkley, J., Nolta, M. R., Bennett, C. L., Gold, B., Hinshaw, G., Jarosik, N., Larson, D., Limon, M., Page, L., Spergel, D. N. and et al., 2009, "Five-Year Wilkinson Microwave Anisotropy Probe Observations: Cosmological Interpretation", ApJS, **180**, 330–376. [DOI], [ADS], [arXiv:0803.0547]

[216] Bernardi, Gianni, Carretti, E., Fabbri, R., Sbarra, C. and Cortiglioni, S., 2005, "The Synchrotron foreground and CMB temperature-polarization cross correlation power spectrum from the first year WMAP data", *Mon.Not.Roy.Astron.Soc.Lett.*, **364**, L5–L7. [DOI], [arXiv:astro-ph/0508278 [astro-ph]]

[217] Cruz, M., Vielva, P., Martínez-González, E. and Barreiro, R. B., 2011, "Anomalous variance in the WMAP data and Galactic foreground residuals", MNRAS, **412**, 2383–2390. [DOI], [ADS], [arXiv:1005.1264 [astro-ph.CO]]

[218] Dobler, G. and Finkbeiner, D. P., 2008, "Extended Anomalous Foreground Emission in the WMAP Three-Year Data", ApJ, **680**, 1222–1234. [DOI], [ADS], [arXiv:0712.1038]

[219] Dobler, Gregory, Draine, Bruce T. and Finkbeiner, Douglas P., 2009, "Constraining Spinning Dust Parameters with the WMAP Five-Year Data", *Astrophys.J.*, **699**, 1374–1388. [DOI], [arXiv:0811.1040 [astro-ph]]

[220] Gold, B., Bennett, C. L., Hill, R. S., Hinshaw, G., Odegard, N., Page, L., Spergel, D. N., Weiland, J. L., Dunkley, J. and et al., 2009, "Five-Year Wilkinson Microwave Anisotropy Probe Observations: Galactic Foreground Emission", ApJS, **180**, 265–282. [DOI], [ADS], [arXiv:0803.0715]

[221] Padovani, P., Ghisellini, G., Fabian, A. C. and Celotti, A., 1993, "Radio-loud AGN and the extragalactic gamma-ray background", MNRAS, **260**, L21–L24. [ADS]

[222] Stecker, F. W. and Salamon, M. H., 1996, "The Gamma-Ray Background from Blazars: A New Look", ApJ, **464**, 600–+. [DOI], [ADS], [arXiv:astro-ph/9601120]

[223] Mücke, A. and Pohl, M., 2000, "The contribution of unresolved radio-loud AGN to the extragalactic diffuse gamma-ray background", MNRAS, **312**, 177–193. [DOI], [ADS]

[224] Chiang, J. and Mukherjee, R., 1998, "The Luminosity Function of the EGRET Gamma-Ray Blazars", ApJ, **496**, 752–+. [DOI], [ADS]

[225] Narumoto, T. and Totani, T., 2006, "Gamma-Ray Luminosity Function of Blazars and the Cosmic Gamma-Ray Background: Evidence for the Luminosity-Dependent Density Evolution", ApJ, **643**, 81–91. [DOI], [ADS], [arXiv:astro-ph/0602178]

[226] Bhattacharya, D., Sreekumar, P. and Mukherjee, R., 2009, "Contribution from unresolved discrete sources to the extragalactic gamma-ray background (EGRB)", *Research in Astronomy and Astrophysics*, **9**, 1205–1214. [DOI], [ADS], [arXiv:0907.1741 [astro-ph.HE]]

[227] Venters, T. M., 2010, "Contribution to the Extragalactic Gamma-Ray Background from the Cascades of very High Energy Gamma Rays from Blazars", ApJ, **710**, 1530–1540. [DOI], [ADS], [arXiv:1001.1363 [astro-ph.HE]]

[228] Ando, S. and Pavlidou, V., 2009, "Imprint of galaxy clustering in the cosmic gamma-ray background", MNRAS, **400**, 2122–2127. [DOI], [ADS], [arXiv:0908.3890 [astro-ph.HE]]

[229] Inoue, Y. and Totani, T., 2009, "The Blazar Sequence and the Cosmic Gamma-ray Background Radiation in the Fermi Era", ApJ, **702**, 523–536. [DOI], [ADS], [arXiv:0810.3580]

[230] Dodelson, Scott, Belikov, Alexander V., Hooper, Dan and Serpico, Pasquale, 2009, "Identifying Dark Matter Annihilation Products In The Diffuse Gamma Ray Background", *Phys.Rev.*, **D80**, 083 504. [DOI], [arXiv:0903.2829 [astro-ph.CO]]

[231] Loeb, A. and Waxman, E., 2000, "Cosmic γ-ray background from structure formation in the intergalactic medium", *Nature*, **405**, 156–158. [ADS], [arXiv:astro-ph/0003447]

[232] Miniati, F., 2002, "Intergalactic shock acceleration and the cosmic gamma-ray background", MNRAS, **337**, 199–208. [DOI], [ADS], [arXiv:astro-ph/0203014]

[233] Colafrancesco, S. and Blasi, P., 1998, "Clusters of galaxies and the diffuse gamma-ray background", *Astroparticle Physics*, **9**, 227–246. [DOI], [ADS], [arXiv:astro-ph/9804262]

[234] Miniati, F., Koushiappas, S. M. and Di Matteo, T., 2007, "Angular Anisotropies in the Cosmic Gamma-Ray Background as a Probe of Its Origin", ApJ, **667**, L1–L4. [DOI], [ADS], [arXiv:astro-ph/0702083]

[235] Pavlidou, V. and Fields, B. D., 2002, "The Guaranteed Gamma-Ray Background", ApJ, **575**, L5–L8. [DOI], [ADS], [arXiv:astro-ph/0207253]

[236] Dermer, C. D., 1986, "Secondary production of neutral pi-mesons and the diffuse galactic gamma radiation", A&A, **157**, 223–229. [ADS]

[237] Abdo, A. A., Ackermann, M., Ajello, M., Anderson, B., Atwood, W. B., Axelsson, M., Baldini, L., Ballet, J., Barbiellini, G., Bastieri, D. and et al., 2009, "Fermi Large Area Telescope Measurements of the Diffuse Gamma-Ray Emission at Intermediate Galactic Latitudes", *Physical Review Letters*, **103**(25), 251 101–+. [DOI], [ADS], [arXiv:0912.0973 [astro-ph.HE]]

[238] Ando, Shin'ichiro, 2009, "Gamma-ray background anisotropy from galactic dark matter substructure", *Phys. Rev.*, **D80**, 023 520. [DOI], [arXiv:0903.4685 [astro-ph.CO]]

[239] Ando, Shin'ichiro, Komatsu, Eiichiro, Narumoto, Takuro and Totani, Tomonori, 2007, "Dark matter annihilation or unresolved astrophysical sources? Anisotropy probe of the origin of cosmic gamma-ray background", *Phys. Rev.*, **D75**, 063 519. [DOI], [arXiv:astro-ph/0612467]

[240] Cuoco, A., Hannestad, S., Haugbølle, T., Miele, G., Serpico, P. D. and Tu, H., 2007, "The signature of large scale structures on the very high energy gamma ray sky", J. Cosmology Astropart. Phys., **4**, 13. [DOI], [ADS], [arXiv:astro-ph/0612559]

[241] Cuoco, Alessandro, Brandbyge, Jacob, Hannestad, Steen, Haugboelle, Troels and Miele, Gennaro, 2008, "Angular Signatures of Annihilating Dark Matter in the Cosmic Gamma-Ray Background", *Phys. Rev.*, **D77**, 123 518. [DOI], [arXiv:0710.4136 [astro-ph]]

[242] Fornasa, Mattia, Pieri, Lidia, Bertone, Gianfranco and Branchini, Enzo, 2009, "Anisotropy probe of galactic and extra-galactic Dark Matter annihilations", *Phys. Rev.*, **D80**, 023 518. [DOI], [arXiv:0901.2921 [astro-ph]]

[243] Hooper, Dan and Serpico, Pasquale D., 2007, "Angular Signatures of Dark Matter in the Diffuse Gamma Ray Spectrum", *JCAP*, **0706**, 013. [arXiv:astro-ph/0702328]

[244] Siegal-Gaskins, J. M., 2010, "The Angular Power Spectrum of the Diffuse Gamma-Ray Background as a Probe of Galactic Dark Matter Substructure", in *2009 Snowbird Particle Astrophysics and Cosmology Workshop (SNOWPAC*

2009), (Ed.) D. B. Kieda & P. Gondolo, vol. 426 of Astronomical Society of the Pacific Conference Series, [ADS], [arXiv:0907.0183 [astro-ph.HE]]

[245] Siegal-Gaskins, Jennifer M. and Pavlidou, Vasiliki, 2009, "Robust identification of isotropic diffuse gamma rays from Galactic dark matter", *Phys. Rev. Lett.*, **102**, 241 301. [DOI], [arXiv:0901.3776 [astro-ph.HE]]

[246] Siegal-Gaskins, Jennifer M., 2008, "Revealing dark matter substructure with anisotropies in the diffuse gamma-ray background", *JCAP*, **0810**, 040. [DOI], [arXiv:0807.1328 [astro-ph]]

[247] Taoso, Marco, Ando, Shin'ichiro, Bertone, Gianfranco and Profumo, Stefano, 2009, "Angular correlations in the cosmic gamma-ray background from dark matter annihilation around intermediate-mass black holes", *Phys. Rev.*, **D79**, 043 521. [DOI], [arXiv:0811.4493 [astro-ph]]

[248] Morris, D. J., 1984, "Production of high-energy gamma rays by cosmic ray interactions in the atmosphere and lunar surface", J. Geophys. Res., **89**, 10 685–10 696. [DOI], [ADS]

[249] Moskalenko, I. V., Porter, T. A., Digel, S. W., Michelson, P. F. and Ormes, J. F., 2008, "A Celestial Gamma-Ray Foreground Due to the Albedo of Small Solar System Bodies and a Remote Probe of the Interstellar Cosmic-Ray Spectrum", ApJ, **681**, 1708–1716. [DOI], [ADS], [arXiv:0712.2015]

[250] Moskalenko, I. V. and Porter, T. A., 2009, "Isotropic Gamma-Ray Background: Cosmic-Ray-Induced Albedo from Debris in the Solar System?", ApJ, **692**, L54–L57. [DOI], [ADS], [arXiv:0901.0304 [astro-ph.HE]]

[251] Mack, Katherine J., Ostriker, Jeremiah P. and Ricotti, Massimo, 2007, "Growth of structure seeded by primordial black holes", *Astrophys.J.*, **665**, 1277–1287. [DOI], [arXiv:astro-ph/0608642 [astro-ph]]

[252] Lacki, B. C. and Beacom, J. F., 2010, "Primordial Black Holes as Dark Matter: Almost All or Almost Nothing", ApJ, **720**, L67–L71. [DOI], [ADS], [arXiv:1003.3466 [astro-ph.CO]]

[253] Koushiappas, S. M., 2006, "Proper Motion of Gamma Rays from Microhalo Sources", *Physical Review Letters*, **97**(19), 191 301–+. [DOI], [ADS], [arXiv:astro-ph/0606208]

[254] Pieri, L., Bertone, G. and Branchini, E., 2008, "Dark matter annihilation in substructures revised", MNRAS, **384**, 1627–1637. [DOI], [ADS], [arXiv:0706.2101]

[255] Ando, S., Kamionkowski, M., Lee, S. K. and Koushiappas, S. M., 2008, "Can proper motions of dark-matter subhalos be detected?", Phys. Rev. D, **78**(10), 101 301–+. [DOI], [ADS], [arXiv:0809.0886]

[256] Koushiappas, S. M., 2009, "The detection of subsolar mass dark matter halos", *New Journal of Physics*, **11**(10), 105 012–+. [DOI], [ADS], [arXiv:0905.1998 [astro-ph.CO]]

[257] Peebles, P. J. E., 1973, "Statistical Analysis of Catalogs of Extragalactic Objects. I. Theory", ApJ, **185**, 413–440. [DOI], [ADS]

[258] Fall, S. M. and Tremaine, S., 1977, "On estimating correlations in the spatial distribution of galaxies", ApJ, **216**, 682–689. [DOI], [ADS]

[259] Mo, H. J., Jing, Y. P. and Boerner, G., 1992, "On the error estimates of correlation functions", ApJ, **392**, 452–457. [DOI], [ADS]

[260] Fry, James N. and Gaztanaga, Enrique, 1993, "Biasing and hierarchical statistics in large scale structure", *Astrophys.J.*, **413**, 447–452. [DOI], [arXiv:astro-ph/9302009 [astro-ph]]

[261] Landy, S. D. and Szalay, A. S., 1993, "Bias and variance of angular correlation functions", ApJ, **412**, 64–71. [DOI], [ADS]

[262] Hamilton, A. J. S., 1993, "Toward Better Ways to Measure the Galaxy Correlation Function", ApJ, **417**, 19–+. [DOI], [ADS]

[263] Bernstein, G. M., 1994, "The variance of correlation function estimates", ApJ, **424**, 569–577. [DOI], [ADS]

[264] Szapudi, I. and Colombi, S., 1996, "Cosmic Error and Statistics of Large-Scale Structure", ApJ, **470**, 131–+. [DOI], [ADS], [arXiv:astro-ph/9510030]

[265] Szapudi, S. and Szalay, A. S., 1998, "A New Class of Estimators for the N-Point Correlations", ApJ, **494**, L41+. [DOI], [ADS]

[266] Ling, E. N., Barrow, J. D. and Frenk, C. S., 1986, "Uncertainties in the cluster-cluster correlation function", MNRAS, **223**, 21P–27P. [ADS]

[267] Barrow, J. D., Bhavsar, S. P. and Sonoda, D. H., 1984, "A bootstrap resampling analysis of galaxy clustering", MNRAS, **210**, 19P–23P. [ADS]

[268] Fisher, K. B., Davis, M., Strauss, M. A., Yahil, A. and Huchra, J., 1994, "Clustering in the 1.2-Jy IRAS Galaxy Redshift Survey. I - The redshift and real space correlation functions", MNRAS, **266**, 50. [ADS], [arXiv:astro-ph/9307001]

[269] Lupton, R., 1993, *Statistics in theory and practice*. [ADS]

[270] Zehavi, I., Blanton, M. R., Frieman, J. A., Weinberg, D. H., Mo, H. J., Strauss, M. A., Anderson, S. F., Annis, J., Bahcall, N. A., Bernardi, M., Briggs, J. W. and et al., 2002, "Galaxy Clustering in Early Sloan Digital Sky Survey Redshift Data", ApJ, **571**, 172–190. [DOI], [ADS], [arXiv:astro-ph/0106476]

[271] Morales, M. F., Williams, D. A. and De Young, T., 2004, "An advanced analysis technique for transient searches in wide-field gamma-ray observatories", *Astroparticle Physics*, **20**, 485–497. [DOI], [ADS], [arXiv:astro-ph/0303178]

[272] Moore, A. W. *et al.*, 2001, "Fast Algorithms and Efficient Statistics: N-Point Correlation Functions", in *Mining the Sky*, (Ed.) A. J. Banday, S. Zaroubi, & M. Bartelmann, [DOI], [ADS], [arXiv:astro-ph/0012333]

[273] Zhang, L. L. and Pen, U.-L., 2005, "Fast n-point correlation functions and three-point lensing application", New A, **10**, 569–590. [DOI], [ADS], [arXiv:astro-ph/0305447]

[274] Eriksen, H. K., Lilje, P. B., Banday, A. J. and Górski, K. M., 2004, "Estimating N-Point Correlation Functions from Pixelized Sky Maps", ApJS, **151**, 1–11. [DOI], [ADS], [arXiv:astro-ph/0310831]

[275] Geringer-Sameth, A. and Koushiappas, S. M., 2011. In preparation

[276] Stecker, F. W., 1970, "The Cosmic γ-Ray Spectrum from Secondary Particle Production in Cosmic-Ray Interactions", Ap&SS, **6**, 377–389. [DOI], [ADS]

[277] Stephens, S. A. and Badhwar, G. D., 1981, "Production spectrum of gamma rays in interstellar space through neutral pion decay", Ap&SS, **76**, 213–233. [DOI], [ADS]

[278] Kelner, S. R., Aharonian, F. A. and Bugayov, V. V., 2006, "Energy spectra of gamma rays, electrons, and neutrinos produced at proton-proton interactions in the very high energy regime", Phys. Rev. D, **74**(3), 034 018–+. [DOI], [ADS], [arXiv:astro-ph/0606058]

[279] Giglietto, N. *et al.*, 2009, "Search for gamma-ray emission from solar system bodies with Fermi-LAT", *ArXiv e-prints*. [ADS], [arXiv:0907.0541 [astro-ph.SR]]

[280] Moskalenko, I. V. and Porter, T. A., 2007, "The Gamma-Ray Albedo of the Moon", ApJ, **670**, 1467–1472. [DOI], [ADS], [arXiv:0708.2742]

[281] Giglietto, N. *et al.*, 2009, "Lunar gamma-ray emission observed by FERMI", *ArXiv e-prints*. [ADS], [arXiv:0907.0543 [astro-ph.SR]]

[282] Giglietto, N. *et al.*, 2009, "Lunar gamma ray emission seen during the first year by Fermi", *ArXiv e-prints*. [ADS], [arXiv:0912.3734 [astro-ph.HE]]

[283] Icecube Collaboration, Achterberg, A., Ackermann, M., Adams, J., Ahrens, J., Andeen, K., Atlee, D. W., Baccus, J., Bahcall, J. N. and et al., 2006, "First year performance of the IceCube neutrino telescope", *Astroparticle Physics*, **26**, 155–173. [DOI], [ADS], [arXiv:astro-ph/0604450]

[284] Hawking, S., 1971, "Gravitationally collapsed objects of very low mass", MNRAS, **152**, 75–+. [ADS]

[285] Ricotti, M., 2007, "Bondi Accretion in the Early Universe", ApJ, **662**, 53–61. [DOI], [ADS], [arXiv:0706.0864]

[286] Ricotti, M. and Gould, A., 2009, "A New Probe of Dark Matter and High-Energy Universe Using Microlensing", ApJ, **707**, 979–987. [DOI], [ADS], [arXiv:0908.0735 [astro-ph.CO]]

[287] Scott, P. and Sivertsson, S., 2009, "Gamma Rays from Ultracompact Primordial Dark Matter Minihalos", *Physical Review Letters*, **103**(21), 211 301–+. [DOI], [ADS], [arXiv:0908.4082 [astro-ph.CO]]

[288] Schmid, C., Schwarz, D. J. and Widerin, P., 1999, "Amplification of cosmological inhomogeneities by the QCD transition", Phys. Rev. D, **59**(4), 043 517–+. [DOI], [ADS], [arXiv:astro-ph/9807257]

[289] Hofmann, S., Schwarz, D. J. and Stöcker, H., 2001, "Damping scales of neutralino cold dark matter", Phys. Rev. D, **64**(8), 083 507. [DOI], [ADS], [arXiv:astro-ph/0104173]

[290] Green, A. M., Hofmann, S. and Schwarz, D. J., 2004, "The power spectrum of SUSY-CDM on subgalactic scales", MNRAS, **353**, L23–L27. [DOI], [ADS], [arXiv:astro-ph/0309621]

[291] Green, A. M., Hofmann, S. and Schwarz, D. J., 2005, "The first WIMPy halos", J. Cosmology Astropart. Phys., **8**, 3–+. [DOI], [ADS], [arXiv:astro-ph/0503387]

[292] Loeb, A. and Zaldarriaga, M., 2005, "Small-scale power spectrum of cold dark matter", Phys. Rev. D, **71**(10), 103 520–+. [DOI], [ADS], [arXiv:astro-ph/0504112]

[293] Chen, X., Kamionkowski, M. and Zhang, X., 2001, "Kinetic decoupling of neutralino dark matter", Phys. Rev. D, **64**(2), 021 302–+. [DOI], [ADS], [arXiv:astro-ph/0103452]

[294] Profumo, S., Sigurdson, K. and Kamionkowski, M., 2006, "What Mass Are the Smallest Protohalos?", *Physical Review Letters*, **97**(3), 031 301–+. [DOI], [ADS], [arXiv:astro-ph/0603373]

[295] Alcock, C., Allsman, R. A., Alves, D. R., Axelrod, T. S., Becker, A. C., Bennett, D. P., Cook, K. H. and et al., 2000, "The MACHO Project: Microlensing Results from 5.7 Years of Large Magellanic Cloud Observations", ApJ, **542**, 281–307. [DOI], [ADS], [arXiv:astro-ph/0001272]

[296] Uglesich, R. R., Crotts, A. P. S., Baltz, E. A., de Jong, J., Boyle, R. P. and Corbally, C. J., 2004, "Evidence of Halo Microlensing in M31", ApJ, **612**, 877–893. [DOI], [ADS], [arXiv:astro-ph/0403248]

[297] LSST Science Collaborations, Abell, P. A., Allison, J., Anderson, S. F., Andrew, J. R., Angel, J. R. P., Armus, L., Arnett, D., Asztalos, S. J., Axelrod, T. S. and et al., 2009, "LSST Science Book, Version 2.0", *ArXiv e-prints*. [ADS], [arXiv:0912.0201 [astro-ph.IM]]

[298] Unwin, S. C., Shao, M., Tanner, A. M., Allen, R. J., Beichman, C. A., Boboltz, D., Catanzarite, J. H., Chaboyer, B. C., Ciardi, D. R., Edberg, S. J., Fey, A. L. and et al., 2008, "Taking the Measure of the Universe: Precision Astrometry with SIM PlanetQuest", PASP, **120**, 38–88. [DOI], [ADS], [arXiv:0708.3953]

[299] Lindegren, L. *et al.*, 2008, "The Gaia mission: science, organization and present status", in *IAU Symposium*, (Ed.) W. J. Jin, I. Platais, & M. A. C. Perryman, vol. 248 of IAU Symposium, [DOI], [ADS]

[300] Erickcek, A. L. and Law, N. M., 2011, "Astrometric Microlensing by Local Dark Matter Subhalos", ApJ, **729**, 49. [DOI], [ADS], [arXiv:1007.4228 [astro-ph.CO]]

[301] Watters, K. P. and Romani, R. W., 2011, "The Galactic Population of Young γ-ray Pulsars", ApJ, **727**, 123–+. [DOI], [ADS], [arXiv:1009.5305 [astro-ph.HE]]

[302] Faucher-Giguère, C.-A. and Loeb, A., 2010, "The pulsar contribution to the gamma-ray background", J. Cosmology Astropart. Phys., **1**, 5–+. [DOI], [ADS], [arXiv:0904.3102 [astro-ph.HE]]

[303] Abdo, A. A. *et al.*, 2010, "The First Fermi Large Area Telescope Catalog of Gamma-ray Pulsars", ApJS, **187**, 460–494. [DOI], [ADS], [arXiv:0910.1608 [astro-ph.HE]]

[304] Abdo, A. A. *et al.*, 2008, "The Fermi Gamma-Ray Space Telescope Discovers the Pulsar in the Young Galactic Supernova Remnant CTA 1", *Science*, **322**, 1218–. [DOI], [ADS], [arXiv:0810.3562]

[305] Abdo, A. A. *et al.*, 2011, "Discovery of High-energy Gamma-ray Emission from the Binary System PSR B1259-63/LS 2883 around Periastron with Fermi", ApJ, **736**, L11. [DOI], [ADS], [arXiv:1103.4108 [astro-ph.HE]]

[306] Abdo, A. A. *et al.*, 2009, "Discovery of Pulsations from the Pulsar J0205+6449 in SNR 3C 58 with the Fermi Gamma-Ray Space Telescope", ApJ, **699**, L102–L107. [DOI], [ADS], [arXiv:0906.1217 [astro-ph.HE]]

[307] Abdo, A. A. *et al.*, 2010, "Discovery of Pulsed γ-Rays from PSR J0034-0534 with the Fermi Large Area Telescope: A Case for Co-Located Radio and γ-Ray Emission Regions", ApJ, **712**, 957–963. [DOI], [ADS]

[308] Abdo, A. A. *et al.*, 2009, "Discovery of Pulsed γ-Rays from the Young Radio Pulsar PSR J1028-5819 with the Fermi Large Area Telescope", ApJ, **695**, L72–L77. [DOI], [ADS], [arXiv:0903.1602 [astro-ph.HE]]

[309] Cognard, I. *et al.*, 2011, "Discovery of Two Millisecond Pulsars in Fermi Sources with the Nançay Radio Telescope", ApJ, **732**, 47–+. [DOI], [ADS], [arXiv:1102.4192 [astro-ph.HE]]

[310] Ray, P. S. *et al.*, 2011, "Precise γ-ray Timing and Radio Observations of 17 Fermi γ-ray Pulsars", ApJS, **194**, 17–+. [DOI], [ADS], [arXiv:1011.2468 [astro-ph.HE]]

[311] Ransom, S. M. *et al.*, 2011, "Three Millisecond Pulsars in Fermi LAT Unassociated Bright Sources", ApJ, **727**, L16+. [DOI], [ADS], [arXiv:1012.2862 [astro-ph.HE]]

[312] Saz Parkinson, P. M. *et al.*, 2010, "Eight γ-ray Pulsars Discovered in Blind Frequency Searches of Fermi LAT Data", ApJ, **725**, 571–584. [DOI], [ADS], [arXiv:1006.2134 [astro-ph.HE]]

[313] Abdo, A. A. *et al.*, 2010, "Detection of the Energetic Pulsar PSR B1509-58 and its Pulsar Wind Nebula in MSH 15-52 Using the Fermi-Large Area Telescope", ApJ, **714**, 927–936. [DOI], [ADS], [arXiv:1003.3833 [astro-ph.HE]]

[314] Keith, M. J. *et al.*, 2011, "Discovery of millisecond pulsars in radio searches of southern Fermi Large Area Telescope sources", MNRAS, **414**, 1292–1300. [DOI], [ADS], [arXiv:1102.0648 [astro-ph.HE]]

[315] Buckley, M. R., Hooper, D. and Rosner, J. L., 2011, "A leptophobic Z and dark matter from grand unification", *Physics Letters B*, **703**, 343–347. [DOI], [ADS], [arXiv:1106.3583 [hep-ph]]

[316] Dobler, G., Cholis, I. and Weiner, N., 2011, "The Fermi Gamma-Ray Haze from Dark Matter Annihilations and Anisotropic Diffusion", ApJ, **741**, 25. [DOI], [ADS], [arXiv:1102.5095 [astro-ph.HE]]

[317] Hooper, D. and Linden, T., 2011, "Gamma rays from the Galactic center and the WMAP haze", Phys. Rev. D, **83**(8), 083 517–+. [DOI], [ADS], [arXiv:1011.4520 [astro-ph.HE]]

[318] Malyshev, D., Cholis, I. and Gelfand, J. D., 2010, "Fermi Gamma-ray Haze Via Dark Matter and Millisecond Pulsars", ApJ, **722**, 1939–1945. [DOI], [ADS], [arXiv:1002.0587 [astro-ph.HE]]

[319] Gendelev, L., Profumo, S. and Dormody, M., 2010, "The contribution of Fermi gamma-ray pulsars to the local flux of cosmic-ray electrons and positrons", J. Cosmology Astropart. Phys., **2**, 16–+. [DOI], [ADS], [arXiv:1001.4540 [astro-ph.HE]]

[320] Buccheri, R., Sacco, B. and Ozel, M. E., 1987, "The feasibility of periodicity searches in gamma-ray astronomy", A&A, **175**, 353–+. [ADS]

[321] Atwood, W. B., Ziegler, M., Johnson, R. P. and Baughman, B. M., 2006, "A Time-differencing Technique for Detecting Radio-quiet Gamma-Ray Pulsars", ApJ, **652**, L49–L52. [DOI], [ADS]

[322] Malyshev, D. and Hogg, D. W., 2011, "Statistics of Gamma-Ray Point Sources below the Fermi Detection Limit", ApJ, **738**, 181. [DOI], [ADS], [arXiv:1104.0010 [astro-ph.CO]]

[323] Dodelson, S., Belikov, A. V., Hooper, D. and Serpico, P., 2009, "Constraining cosmological dark matter annihilation with gamma ray observations", Phys. Rev. D, **80**(8), 083 504–+. [DOI], [ADS], [arXiv:0903.2829 [astro-ph.CO]]

[324] Baxter, E. J. and Dodelson, S., 2011, "Robust approach to constraining dark matter properties with gamma-ray data", Phys. Rev. D, **83**(12), 123 516–+. [DOI], [ADS], [arXiv:1103.5779 [astro-ph.CO]]

[325] Siegal-Gaskins, J. M., 2008, "Revealing dark matter substructure with anisotropies in the diffuse gamma-ray background", J. Cosmology Astropart. Phys., **10**, 40–+. [DOI], [ADS], [arXiv:0807.1328]

[326] Siegal-Gaskins, J. M., Reesman, R., Pavlidou, V., Profumo, S. and Walker, T. P., 2011, "Anisotropies in the gamma-ray sky from millisecond pulsars", MNRAS, **415**, 1074–1082. [DOI], [ADS], [arXiv:1011.5501 [astro-ph.HE]]

[327] Lorimer, D. R., 2008, "Binary and Millisecond Pulsars", *Living Reviews in Relativity*, **11**, 8–+. [ADS], [arXiv:0811.0762]

[328] Ransom, S. M., 2007, "Finding (or not) New Gamma-ray Pulsars with GLAST", in *The First GLAST Symposium*, (Ed.) S. Ritz, P. Michelson, & C. A. Meegan, vol. 921 of American Institute of Physics Conference Series, [DOI], [ADS], [arXiv:0704.1131]

[329] Ransom, S. M., Eikenberry, S. S. and Middleditch, J., 2002, "Fourier Techniques for Very Long Astrophysical Time-Series Analysis", AJ, **124**, 1788–1809. [DOI], [ADS], [arXiv:astro-ph/0204349]

[330] Groth, E. J., 1975, "Probability distributions related to power spectra.", ApJS, **29**, 285–302. [DOI], [ADS]

[331] Vaughan, B. A. *et al.*, 1994, "Searches for millisecond pulsations in low-mass X-ray binaries, 2", ApJ, **435**, 362–371. [DOI], [ADS]

[332] Alpar, M. A., Cheng, A. F., Ruderman, M. A. and Shaham, J., 1982, "A new class of radio pulsars", Nature, **300**, 728–730. [DOI], [ADS]

[333] Radhakrishnan, V. and Srinivasan, G., 1982, "On the origin of the recently discovered ultra-rapid pulsar", *Current Science*, **51**, 1096–1099. [ADS]

[334] Bhattacharya, D. and van den Heuvel, E. P. J., 1991, "Formation and evolution of binary and millisecond radio pulsars", Phys. Rep., **203**, 1–124. [DOI], [ADS]

[335] Tauris, T. M. and van den Heuvel, E. P. J., 2006, "Formation and evolution of compact stellar X-ray sources", in *Compact stellar X-ray sources*, (Ed.) Lewin, W. H. G. & van der Klis, M., [ADS]

[336] Ransom, S. M., Cordes, J. M. and Eikenberry, S. S., 2003, "A New Search Technique for Short Orbital Period Binary Pulsars", ApJ, **589**, 911–920. [DOI], [ADS], [arXiv:astro-ph/0210010]

[337] de Jager, O. C., Raubenheimer, B. C. and Swanepoel, J. W. H., 1989, "A poweful test for weak periodic signals with unknown light curve shape in sparse data", A&A, **221**, 180–190. [ADS]

[338] Buccheri, R. *et al.*, 1983, "Search for pulsed gamma-ray emission from radio pulsars in the COS-B data", A&A, **128**, 245–251. [ADS]

[339] Abdo, A. A. *et al.*, 2009, "Detection of 16 Gamma-Ray Pulsars Through Blind Frequency Searches Using the Fermi LAT", *Science*, **325**, 840–. [DOI], [ADS], [arXiv:1009.0748 [astro-ph.GA]]

[340] Abdo, A. A. *et al.*, 2009, "Fermi/Large Area Telescope Bright Gamma-Ray Source List", ApJS, **183**, 46–66. [DOI], [ADS], [arXiv:0902.1340 [astro-ph.HE]]

[341] Abdo, A. A. *et al.*, 2010, "Fermi Large Area Telescope First Source Catalog", ApJS, **188**, 405–436. [DOI], [ADS], [arXiv:1002.2280 [astro-ph.HE]]

[342] Reif, F., 1965, *Fundamentals of Statistical and Thermal Physics*, Waveland Press. [ADS]